Catalyst development for hydrogenation of carbon oxides

炭素酸化物の水素化反応に関する触媒開発

Rungtiwa Kosol

Supervisor: Prof. Noritatsu Tsubaki

Tsubaki Laboratory

Graduate School of Science and Engineering

University of Toyama

Preface

Non-renewable like fossil fuels, including coal, oil, and gas have been played an important role in global energy systems. The combustion from fossil fuels were released as CO, NO_x, CH_4, and CO_2 that CO_2 is the main cause of greenhouse phenomena.

Casually, a growing concern of fossil fuels exhaustion has exhibited in the scientific community in the last decade or so. In fact, that at some point in time fossil fuels production will begin to decline is inescapable from the earth point of view: natural gas, crude oil, and coal are finite natural resources. This step will speed up because, according to the economic principle of substitution, as extraction costs increase after the easily obtained fossil fuel reserves have been used up, market forces will design favorable conditions for the implementation of alternative energy sources. Furthermore, fossil fuels also have negative impacts, being the dominant source of local air pollution and emitter of carbon dioxide (CO_2) and other greenhouse gases. As a result, researchers are therefore urged to develop a renewable and cleaner energy as substitutes for fossil fuels.

Syngas ($CO+H_2$) is a non-petroleum resource which can be produced from biomass, natural gas and coal. With the existence of syngas, it is possible to convert the lower carbon resource into industrial and commercial-valued products, such as hydrocarbon products, ethanol, aldehydes or even aromatics. Overall, producing of high value-added chemicals from syngas is of great importance from both academic and industrial aspect. As well-known to us all, the way of designing catalysts can be crucial in enhancing its catalytic efficiency throughout the reactions, among which catalyst designed with unique structure tend to exhibit outstanding performance in some reaction. As typical representatives, nitrogen-containing functional groups developed in carbon structure mainly consists of N-C structures arranged in a pyridine-like configuration, which explains the metallic behavior observed in these nanostructures. Nitrogen atom modification provides a promising means for CO_2 fixation to C_{2+} alkenes and rational design of functionalized Fe-supported carbon catalyst. These promotional effects were ascribed to the improved surface basicity as well as reduction and carburization processes.

Therefore, in this thesis, we mainly concentrate on a nitrogen incorporation was selected to modify the chemical structure of carbon support, and its promotional effects for CO_2 hydrogenation were investigated. (1) FeK/C-1EDA catalyst was designed for liquid hydrocarbon (C_{5+}); (2) a spinel catalyst, $ZnFe_2O_x$ catalyst exhibits the best catalytic performance with larger light olefins selectivity and chain growth ability. (Chapter 2); (3) the CuZn-SC-P5 catalyst, after improvement strategies, exhibited excellent performance. The conversions of CO and total carbon reached 55.8 and 49.5 %, respectively. (Chapter 3)

In chapter 1, ethylene diamine (EDA, NH_2-CH_2-CH_2-NH_2) as a nitrogen incorporation source was selected to modify the chemical structure of carbon support, and its promotional effects for CO_2 hydrogenation were investigated. The EDA loading amount was also investigated towards an optimal catalytic behavior effect. Meanwhile, to further enhance heavy hydrocarbon selectivity, potassium (K) alkaline promoter was further utilized to modify nitrogen-doped catalysts. Based on the characterization findings and reaction results, it is disclosed that the improved surface alkalinity by nitrogen doping and the increased carbide content, owing to the addition of K promoter, enhanced the catalytic performance of CO_2 hydrogenation. The study provides a rapid and effective way for the synthesis of nitrogen functionalize into carbon structure over Fe-based catalyst.

In chapter 2, the fabrication of heteroatom doped iron-based catalysts (spinel-like structure) through urea self-combustion method, and catalytic performances over these self-combustion catalysts are investigated in detail. It is found that catalytic performances are affected by the properties of doped metals. Owing to the high methanation activity of Ni and Co, $NiFe_2O_x$ and $CoFe_2O_x$ catalysts present high CH_4 selectivity compared to Fe_2O_3 catalysts. $MgFe_2O_x$ exhibits high olefin hydrogenation ability. By contrast, the utilization of Cu and Zn promotes catalytic activity and olefins selectivity via regulating surface CO_2 adsorption and carbides content. Among these spinel catalysts, the $ZnFe_2O_x$ catalyst shows the best CO_2 hydrogenation performance. Enhanced CO_2 adsorptions as well as active species of carbides result in the benign hydrogenation behavior.

In chapter 3, the catalytic results of alcohol-assisted LT-MS reveal that via the two optimized strategies, a CuZn-SC-P5 catalyst exhibits superior catalytic performance. It is significantly different from the CuZn-based catalysts prepared by traditional impregnation method, and also better than the catalysts treated by sole PEG treatment or supercritical CO_2 drying. The work provides multiple strategies to improve catalytic efficiency, and will be beneficial to explore new approaches in catalyst synthesis.

Herein, nitrogen incorporation into a carbon support material provides a promising means for regulating their electronic structure and active sites distribution of doped-carbon supported iron oxides, to achieve an enhanced catalytic CO_2 hydrogenation performance. Also, the two optimized strategies that use polyethylene glycol (PEG) surfactant and supercritical CO_2 drying in urea co-precipitation method, to synthesize the highly efficient CuZn-based catalysts.

Content

Preface I

Chapter 1 1

Iron catalysts supported on nitrogen functionalized carbon for improved CO_2 hydrogenation performance...1

Abstract... 2

1.1 Introduction 3

1.2 Experimental section 4

1.2.1 Catalyst preparation.. 4

1.2.2 Catalyst characterization.. 5

1.2.3 Catalytic performance 6

1.3 Result and discussion 7

1.3.1 Texture and morphological properties of the catalysts 7

1.3.2 Bulk composition of different catalysts 9

1.3.3 H_2 reduction behavior and surface basic properties..................................11

1.3.4 Surface chemical composition...13

1.3.5 Catalytic performance evaluation...18

1.4 Conclusions 21

References 22

Chapter 2 24

Heteroatom doped Iron-based catalysts preparaed by urea self-combustion method for effcient CO_2 hydrogenation 24

Abstract.. 25

2.1 Introduction 26

2.2 Experimental section 29

2.2.1 Catalysts preparation 29

2.2.2 Catalytic characterization......31
2.2.3 Catalyst activity evaluation 32
2.3 Results and discussion......33
2.3.1 Surface morphology of catalyst...... 33
2.3.2 Chemical phase of catalyst 36
2.3.3 Reducibility and reactant adsorption state of catalyst......39
2.3.4 Surface composition property of catalyst......42
2.3.5 Effect of different metals......46
2.3.6 Effect of different Zn/Fe molar ratio......51
2.3.7 Rational design of efficient iron-based catalysts......52
2.4. Conclusions 53
References 54
Chapter 3 58
Fabrication of CuZn-Based catalyst via Polyethylene Glycol surfactant and supercritical drying...... 58
Abstract...... 59
3.1 Introduction 60
3.2 Experimental section 61
3.2.1 Catalysts preparation 61
3.2.2 Catalyst characterizations...... 63
3.2.3 Catalyst evaluation 64
3.3 Results and discussion......66
3.3.1 CuZn-SC-Px for alcohol-assisted LT-MS......66
3.3.2 CuZn-Px for alcohol-assisted LT-MS......81
3.3.3 Different types of CuZn-based catalysts for alcohol-assisted LT-MS…85
3.4 Conclusions 92

References ... 93

Chapter 4 ... 96

Summary ... 96

List of publications ... 98

List of conferences ... 100

Acknowledgements ... 101

Chapter 1

Iron catalysts supported on nitrogen functionalized carbon for improved CO_2 hydrogenation performance

Nitrogen-containing functional groups developed in carbon structure mainly consists of N-C structures arranged in a pyridine-like configuration, which explains the metallic behavior observed in these nanostructures. Nitrogen atom modification provides a promising means for CO_2 fixation to C_{2+} alkenes and rational design of functionalized Fe-supported carbon catalyst.

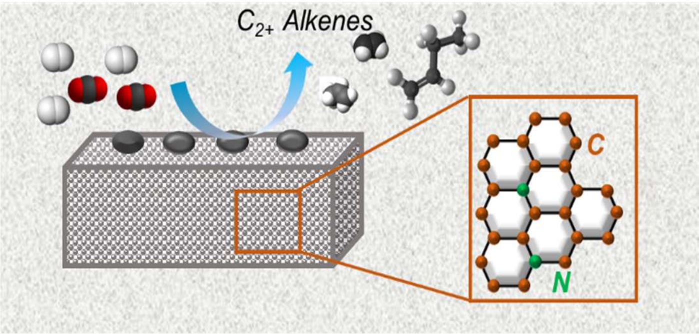

Abstract

Preparation of highly efficient Fe-based catalysts is a reliable and achievable goal for catalyzing CO_2 hydrogenation. Herein, ethylene diamine as a benign modifier well regulates the surface properties of carbon support, achieving a good dispersion of active small-size iron carbide sites. With the further incorporation of alkaline K promoter, heavy hydrocarbon selectivity (C_{5+}) is increased from 14.8% to 39.8%. Combining several catalyst characterizations (XRD, CO_2-TPD, H_2-TPR, TEM, and XPS) and reaction data, discloses that good dispersion, enhanced reduction/carburization behavior, and small-size carbides formation are essential for improving CO_2 performance. Simultaneous doping of nitrogen atoms and alkali metal provides a promising means for CO_2 fixation and rational design of functionalized metal-supported carbon catalysts.

Keywords: Nitrogen incorporation, CO_2 hydrogenation, Carbon materials, Fe-based catalyst, Alkaline promoter.

1.1 Introduction

Massive CO_2 emissions associated with human activities such as transportation, industry, deforestation, agriculture, etc., result in a series of problems such as global warming and ocean acidification, compelling mankind to seek a path of sustainable development [1–4]. CO_2 thermal catalytic utilization can be achieved via a modified Fischer-Tropsch synthesis (FTS) or methanol-mediated process (methanol to hydrocarbons, MTH) [5–10]. Considering the fact that Fe-based catalysts have two types of active sites under working reaction conditions, namely, Fe_3O_4 responsible for CO intermediates formation and Fe_5C_2 for subsequent chain propagation [1,11], it is widely used in the process of CO_2 hydrogenation via FTS [11–13].

Generally, support materials play a crucial role in the dispersion and stabilization of deposited active sites during catalytic processes. Conventional supports for iron-based catalysts include Al_2O_3, SiO_2, zeolite, etc. However, the interaction between the metal and inert oxide supports usually leads to the formation of unreducible compounds or inferior carbonization behavior with poor catalytic performance [7,13,14]. Apart from the inert oxide materials, carbon materials owing to their tunable surface properties such as electronic effect, structure, and a favorable carbon environment, have been widely used in the catalysis field in the last two decades [15–17].

Nitrogen incorporation as a promising means can well regulate the surface properties of carbon supports by promoting the formation of defect sites or regulating nitrogen configuration structure [13,17,18]. Liu et al. [15] reported that the utilization of nitrogen doping promoted the selectivity of light olefins with high activity [15]. These promotional effects were ascribed to the improved surface basicity as well as reduction and carburization processes. More recently, Guo et al. [13] investigated in some detail the effects of different nitrogen groups incorporation on CO_2 hydrogenation. Nitrogen modification was beneficial for iron oxide reduction, CO_2 adsorption and iron defect formation, and consequently the catalyst with nitrogen doping presented high activity and low CO by-product selectivity, achieving thus high carbon atom utilization [13]. Although nitrogen doping as a useful means to improve the reaction performance has been reported in recent years, further promoter modifications of conventional iron-based catalysts, such as K or Na incorporation has not yet received enough attention [19–21]. Generally, the promotional effects are ascribed to the favorable carburization, enhanced CO_2/H_2 adsorption, and weak secondary hydrogenation ability [5,11,22,23].

Herein, ethylene diamine (EDA, NH_2-CH_2-CH_2-NH_2) as a nitrogen incorporation source was selected to modify the chemical structure of carbon support, and its promotional effects for CO_2 hydrogenation were investigated. The EDA loading amount was also investigated towards an optimal catalytic behavior effect. Meanwhile, to further enhance heavy hydrocarbon selectivity, potassium (K) alkaline promoter was further utilized to modify nitrogen-doped catalysts. Based on the characterization findings and reaction results, it is disclosed that the improved surface alkalinity by nitrogen doping and the increased carbide content, owing to the addition of K promoter, enhanced the catalytic performance of CO_2 hydrogenation. More importantly, an enhanced number density of small-size active sites were formed with the N-decoration of carbon support materials. All these findings provide new insights for strengthening the catalytic performance via regulating carbon surface properties, being approached by nitrogen incorporation as well as electronic promoter modification of carbon support.

1.2 Experimental section

1.2.1 Catalysts preparation

Nitrogen-functional carbon support. The nitrogen-functional carbon support was fabricated via a one-pot hydrothermal treatment of glucose and ethylene diamine (EDA) at 180 °C for 24 hours. Obtained products were filtered and washed several times with distilled water and 20 ml of ethanol respectively. Two nitrogen functional carbon supports were synthesized by changing the weight of EDA, namely C-1EDA and C-2EDA. Thereinto, 1 stands for 1 g of EDA and 2 for 2 g of EDA. For comparison, the carbon material free of nitrogen was also synthesized by the hydrothermal treatment of glucose only at 180 ºC for 24 hours. The obtained non-doped carbon material was denoted as C.

Fe-supported nitrogen-functional carbon catalysts. The Fe-supported nitrogen-functional carbon catalysts were prepared by the incipient wetness impregnation method. The as-prepared C-1EDA was impregnated with an aqueous solution of $Fe(NO_3)_3 \cdot 9H_2O$ under ultrasound for 30 minutes. The final sample was calcined at 500 °C for 5 hours in N_2 gas atmosphere (60 mL/min), which is denoted as Fe/C-1EDA. The loading of Fe used was 20 wt%. Compared to Fe/C-1EDA, the Fe/C-2EDA and Fe/C without EDA addition were also prepared with the same loading of Fe. The K-promoted Fe/C-1EDA was prepared by the treatment of Fe/C-1EDA with K_2CO_3 solution via the wet impregnation method (1 wt% K). The sample was then calcined at 500 °C in N_2 gas flow for 4 hours, and is named FeK/C-1EDA.

1.2.2 Catalysts characterization

The powder X-ray diffraction (XRD) analyses were conducted by an X-ray diffractometer (Rigaku RINT 2400) with Cu Kα radiation (40 kV and 20 mA). The N_2 adsorption-desorption measurements at − 196 °C were used to determine surface area (texture) of catalysts (NOVA 2200e instrument). Prior to measurements, the catalysts were degassed at 200 °C under vacuum conditions for 6 hours. The specific surface area of the solids (m^2 /g) was estimated based on the Brunauer-Emmett-Teller (BET) method. Scanning electron microscopy (SEM, JEOL JSM-6360LV) was employed to analyze surface morphologies of samples. Transmission electron microscopy (TEM, JEOL JEM-3200Fs) was employed to record high-magnification morphology images of the solid catalyst samples at the acceleration voltage of 100 kV.

H_2 temperature-programmed reduction (H_2-TPR) traces of the solids were obtained using a BELCAT-II-T-SP analyzer with a thermal conductivity detector (TCD). A 50-mg sample was first pretreated at 150 °C with He for 1 hour. Then a 5 vol% H_2/Ar gas mixture was fed into the reactor (30 mL/min) when the temperature was cooled to 50 °C. Finally, the H_2-TPR traces were recorded from 50 to 900 °C with a heating rate of 10 °C/min. The CO_2 temperature programmed desorption (CO_2-TPD) was also studied using the same equipment used in H_2-TPR. A 50-mg sample was first reduced at 400 °C in H_2 gas flow (30 mL/min) for 2 hours. After reduction, the temperature of the solid was decreased to 50 °C in He gas flow (30 mL/min). A 10 vol% CO_2/Ar gas mixture was then introduced into the reactor for 1 h. Then He was introduced into the reactor to remove gas phase CO_2. The CO_2-TPD trace was recorded from 50 to 900 °C with a heating rate of 10 °C/min. X-ray photoelectron spectroscopy (XPS) analysis was performed by a Thermo Fischer Scientific ESCALAB 250 Xi instrument equipped with a catalyst pretreatment chamber for varying gas composition.

1.2.3 Catalytic performance

The catalytic tests were performed using a continuous-flow fixed-bed reactor (i.d. = 6 mm), loaded with 0.5 g catalyst packed into the middle of the reactor and in situ reduced by pure H_2 at 380 °C for 8 hours before the start of the catalytic measurements. After reduction, the H_2/CO_2 gas mixture including Ar as inner standard was introduced into the reactor system. The reaction was carried out at 300 °C and 1.0 MPa for 6 hours. The effluent gas composition was analyzed by two on-line gas chromatographs (GC) with thermal conductivity detector (TCD) and flame ionization detector (FID) to determine the CO_2 conversion and light hydrocarbons selectivity (C_1-C_7), respectively. The heavy hydrocarbons (C_4-C_{18}) were collected using a cold trap and analyzed by an off-line GC with n-dodecane (0.1 g) as an internal standard.

Furthermore, CO_2 conversion was calculated by equation **(1).** CO selectivity was calculated by equation **(2)**. For hydrocarbons selectivity was estimated according to equation **(3)**.

$$CO_{2\ \text{conversion}\ (\%)} = (CO_{2\ \text{in}} - CO_{2\ \text{out}})/CO_{2\ \text{in}} \times 100\% \qquad \textbf{(1)}$$

- $CO_{2\ \text{in}}$: mole fraction of CO_2 in the inlet.
- $CO_{2\ \text{out}}$: mole fraction of CO_2 in the outlet.

$$CO_{\text{selectivity}\ (\%)} = CO_{\text{out}}/\ (CO_{2\ \text{in}} - CO_{2\ \text{out}}) \times 100\% \qquad \textbf{(2)}$$

- CO_{out}: mole fraction of CO in the outlet.

$$C_{i\ \text{hydrocarbon selectivity (C-mol \%)}} = \text{Mole of } C_{i\ \text{hydrocarbons}}\ /\ \text{Mole of total hydrocarbon} \times 100\% \ \textbf{(3)}$$

1.3 Result and discussion

1.3.1 Texture and morphological properties of the catalysts

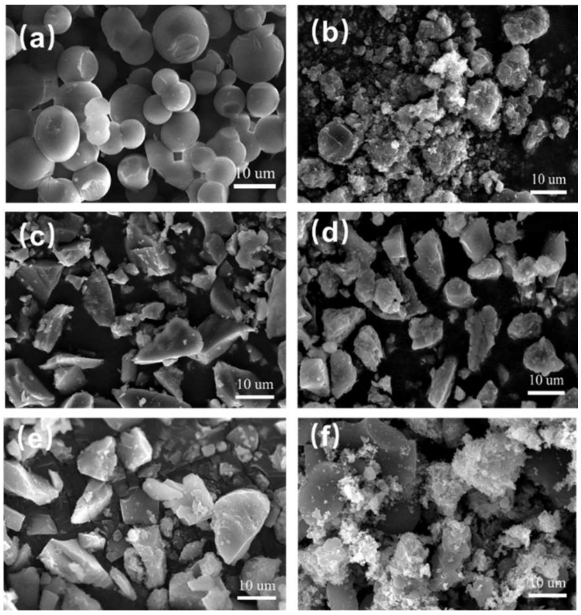

Figure 1.1 Typical SEM images of fresh catalysts, (a) C, (b) Fe/C, (c) Fe/C-1EDA, (d) Fe/C-2EDA, (e) FeK/C-1EDA, (f) FeK/C.

The textural and morphological properties of the catalysts are depicted in Figure 1.1. For carbon precursors, a smooth spherical structure with dimensions ranging from 5 to 10 μm is appeared, which is consistent with previous reports [13,24]. However, the morphologies and structures of the catalysts change significantly after high-temperature treatment (Figure 1.1b-d), showing an irregular block structure. Although the addition of EDA with different content does not obviously change the size of the catalyst, the introduction of EDA can make the surface of the catalyst smoother than the catalysts without nitrogen modification (Figure 1.1c-e). Besides, the introduction of alkali metal K does not obviously change the size of the catalyst. SEM-mapping images also indicate that the active metals were dispersed uniformly with or without the nitrogenous reagent (EDA) added (Figure 1.2). Meanwhile, specific surface areas of the various catalysts investigated are listed in Table 1. Compared with Fe/C catalyst, a suitable additive amount is beneficial to increase somehow the SSA (8.5 m^2 /g vs. 6.8 m^2 /g). It should be noted that the addition of excessive EDA reagent results in lower specific surface area for the catalyst (Fe/C-2EDA). With further modification of K promoter, the BET surface area decreases slightly.

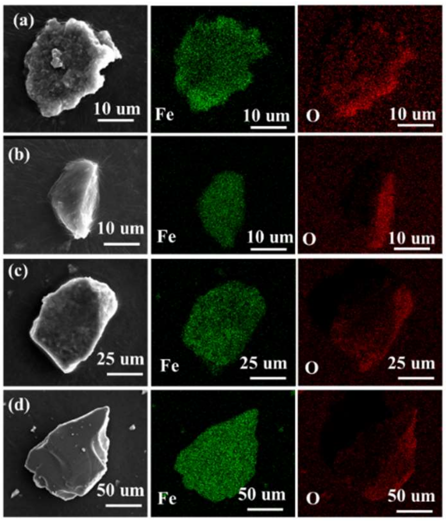

Figure 1.2 Element distribution images of fresh (a) Fe/C; (b) Fe/C-1EDA; (c) Fe/C-2EDA; (d) FeK/C-1EDA.

1.3.2 Bulk composition of different catalysts

The iron phases of different catalysts before and after reaction were identified by powder XRD analyses (Figure 1.3). Figure 1.3a shows that for Fe/C catalyst without nitrogen modification, the main phase is Fe_3O_4 (JCPDS, 89–0691) [25]. However, for the Fe/C-1EDA and Fe/C-2EDA catalysts, the catalyst with nitrogen incorporation exhibits no obvious sharp characteristic diffraction peaks of Fe_3O_4, suggesting fine particle sizes or uniform distribution. It is easy to infer that the modification of carbon with appropriate EDA reagent can affect the crystallite size or/and dispersion of iron oxide. Meanwhile, the crystallite sizes calculated by the Scherrer equation are compared in Table 1.1. The utilization of nitrogen-atom doping results in the small crystallite sizes of the iron oxide phase. The introduction of potassium (K) alkali metal leads to particle enlargement, especially for the catalyst without nitrogen doping. This result strongly suggests that the presence of nitrogen atom promotes the formation of small-size iron oxide particles. As presented in Figure 1.3b, all catalysts after reaction contain Fe_3O_4, an active phase for converting CO_2 into CO intermediates [11,20].

Different from FeK/C catalyst, no obvious peaks ascribed to Fe_5C_2 (JCPDS, 20–0509) appear in the EDA-added catalysts, probably due to the fine particle sizes. Crystallite sizes of FeK/C and FeK/C-1EDA were measured according to the Scherrer equation (Table 1.1). As expected, FeK/C-1EDA catalyst shows a rather small crystallite size than FeK/C. The modification of the carbon support material by nitrogenous reagent (EDA) is conducive to the formation of small particles and high dispersion of iron oxide species, which has an important influence to boost the reaction performance [17,18].

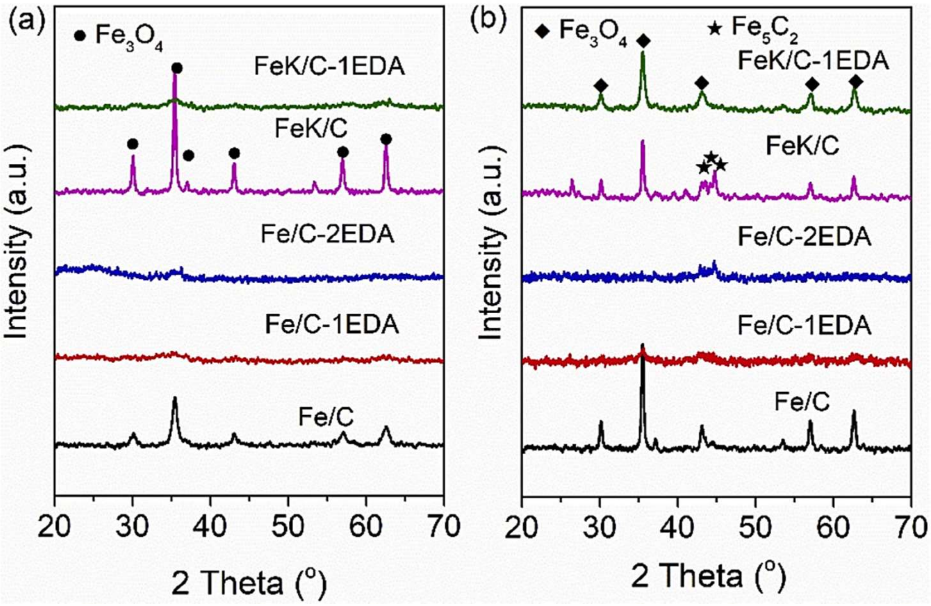

Figure 1.3 Powder XRD patterns of (a) as-prepared catalysts and (b) spent catalysts.

Table 1.1 Average crystallite size of iron phase, surface area, and reduction/ adsorption properties of catalysts.

Catalysts	Surface area[a] (m^2/g)	Fresh catalysts[b] (nm)	Spent catalysts[b] (nm)	Total H_2 consumption[c] (mmol/g)	Total CO_2 uptake[c] (mmol/g)
Fe/C	6.8	11.6	22.1	1.42	0.33
Fe/C-1EDA	8.5	5.5	7.0	0.66	0.42
Fe/C-2EDA	5.8	4.6	5.9	0.46	0.21
FeK/C-1EDA	7.1	7.4	9.6	0.90	0.38
FeK/C	6.4	22.5	23.9	1.88	0.26

[a] Calculated by the Brunauer-Emmett-Teller (BET).

[b] Calculated by Scherrer equation. For fresh catalysts, average crystallite stands for Fe_3O_4 particles, while for spent catalysts stands for Fe_3O_4/Fe_5C_2 particles.

[c] Calculated by H_2-TPR and CO_2-TPD methods. To exclude factors such as carbon gasification, only peaks located in the 200–600 °C range are considered (H_2-TPR and CO_2-TPD traces).

1.3.3 H_2 reduction behavior and surface basic properties

Generally, the reduction behavior of a catalyst can be regarded as the first step of phase composition change followed by an in-situ formation of the active sites. The reduction behavior of the various catalysts examined is compared in Figure 1.4a. The total H_2 consumption (mmol/g) is also compared in Table 1. Obviously, there is a distinct tailing peak between 300 and 550 °C, including the reduction process of Fe_3O_4 to FeO and FeO to metallic Fe [23]. As illustrated in Figure 1.4a, compared with Fe/C catalyst, Fe/C-1EDA has a lower initial reduction temperature (334 °C), which is beneficial for the subsequent formation of active sites such as iron carbide. However, excessive utilization of nitrogen containing reagent makes reduction behavior more difficult. Although the introduction of alkaline promoter K can delay the initial reduction temperature, the FeK/C-1EDA catalyst also has a low initial reduction temperature. The reduction peaks between 550 °C and 900 °C are ascribed to carbon gasification or the degradation of carbonaceous species at high temperatures [13,18]. It should be noted that for the positive hydrogen consumption peak (300–550 °C), it represents the reduction process of metal oxide (Fe_3O_4 to metallic Fe), while for the complicated tail-peak between 550 and 900 °C, it may represent carbon gasification or degradation of C_xH_y hydrocarbon-like adsorbed chains to C and H_2 at high temperatures (> 650 °C). At the reaction temperature (ca. 300 ℃), the process of hydrogen generation caused by the high temperature (> 650 °C) as discussed above can be ignored.

Catalysts CO_2 adsorption/desorption characteristics are shown in Figure 1.4b. The desorption peaks between 450 and 600 °C can be ascribed to chemisorbed-type CO_2 species, while the peaks appearing between 600 and 800 °C can be assigned to the presence of carbonaceous materials degradation [13]. Compared to Fe/C, with the incorporation of nitrogen atom, the intensity of the desorption peaks increases significantly. The interaction between the acidic CO_2 molecule and the surface basic sites is enhanced as depicted in Figure 1.4b (compare FeK/C vs. Fe/C and Fe/C-1EDA vs. Fe/C). It indicates that the introduction of nitrogen atoms and K promoter can obviously enhance the surface basicity of the catalyst and strengthen the interaction with the acidic CO_2 reactant. However, excessive utilization of EDA reagent presents a poor CO_2 adsorption capacity, suggesting that the surface basic properties can be regulated by adjusting the EDA addition amount (Table 1.1). Generally, enhanced surface CO_2 adsorption is beneficial to the increase of the adsorbed CO_2/H surface ratio, promoting chain propagation [11]. As shown in Table 1.1, with the incorporation of suitable EDA reagent amount, the surface basicity of the catalyst is enhanced (Tables 1.1, 0.42 vs. 0.33 mmol/g), thus promoting CO_2 chemisorption. Therefore, the enhanced surface basicity allows the catalyst surface to be rich in adsorbed CO_2 species (carbonate-like structure).

The intermediate species of hydrocarbons are less likely to undergo terminal hydrogenation in an adsorbed CO_x enriched atmosphere, thus promoting the formation of long-chain hydrocarbons. By contrast, the further incorporation of K promoter degrades adsorption behavior of CO_2 slightly (see Table 1.1 and Figure 1.4b). This finding suggests that the main promotional effect derived from the K promoter may not come from the improvement of adsorption properties, but rather from the enhanced surface carburization and weakening of the secondary hydrogenation ability of olefins.

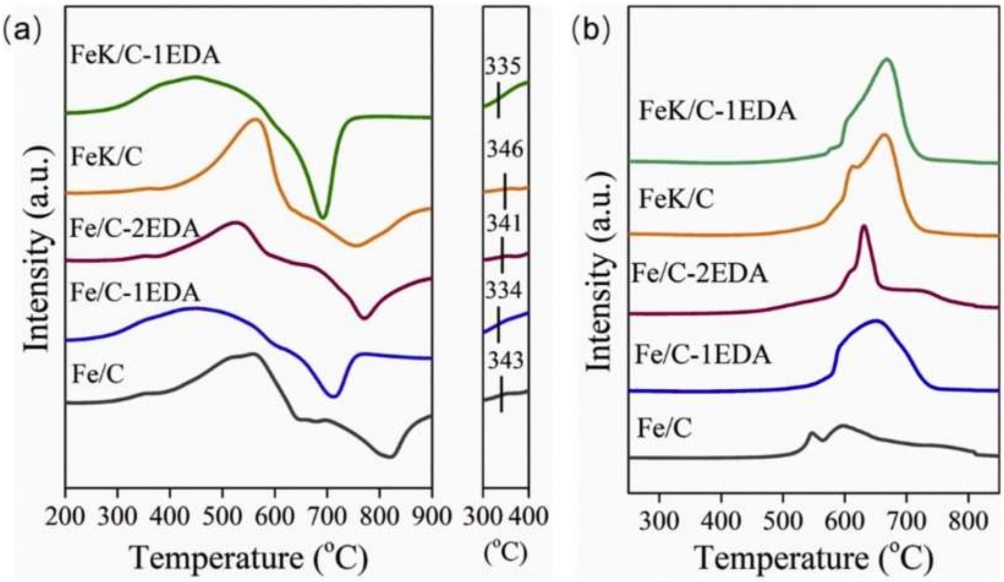

Figure 1.4 (a) H_2-TPR traces and (b) CO_2-TPD traces of different catalysts.

1.3.4 Surface chemical composition

Given that the surface composition of a catalyst has an important effect on the catalytic performance, the catalysts surface chemical composition was investigated. The survey scan spectra of different Fe-based catalysts are compared in Figure 1.5. According to Figure 1.6a, the peaks at 708.5, 710.7 and 712.6 eV are assigned to Fe–C, Fe^{II} and Fe^{III} [26]. Thereinto, Fe–C bonds are generally ascribed to carbides, such as Fe_5C_2 [20]. C1s XPS spectra are also provided in Figure 1.8. The C1s spectrum can be deconvoluted into three peaks assigned to C=O bond (286.8 eV), C–O bond (284.9 eV) and C–C/C=C bond (283.8 eV) [26]. Compared to Fe/C catalyst, Fe/C-1EDA shows a higher content of Fe–C, a crucial species for the catalytic hydrogenation of CO_2 to hydrocarbons (Table 1.2 and Figure 1.6a). However, the Fe–C content on the Fe/C-2EDA is lowered again, which indicates that a suitable N addition amount is vital. Nevertheless, the concentration of Fe^{II} is still significantly larger than that of Fe/C catalyst. This indicates that doping of nitrogen atoms has two promotional effects: one is to improve the reduction of iron oxides, and the other is to promote the generation of active carbides. Generally, Fe_3O_4 is responsible for converting CO_2 to adsorbed CO intermediates, while Fe–C is responsible for the conversion of CO to hydrocarbons [11,20]. Surface content of Fe_3O_4 (Fe_2O_3·FeO) can be reflected according to the Fe^{II} content to some extent. Therefore, both the improved reduction and carbonization behavior can boost the improvement of reaction performance. With the introduction of alkali metal K, in addition to the improvement of carbonization behavior, the catalysts (FeK/C-1EDA and FeK/C, Table 1.2) exhibit a higher composition of low-valence iron species.

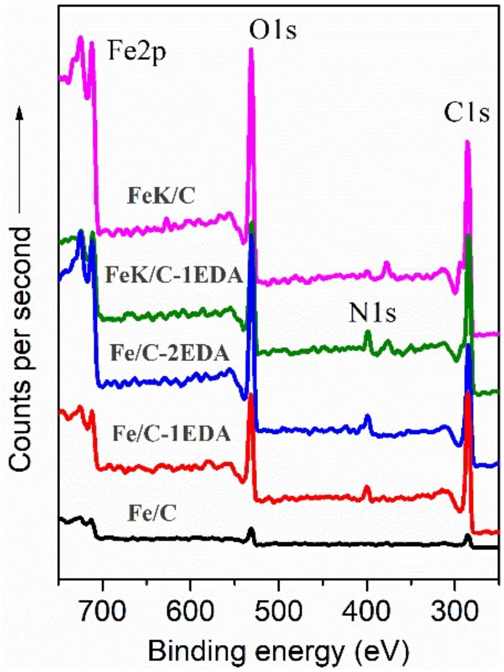

Figure 1.5 XPS survey scan spectra of different Fe-based catalysts.

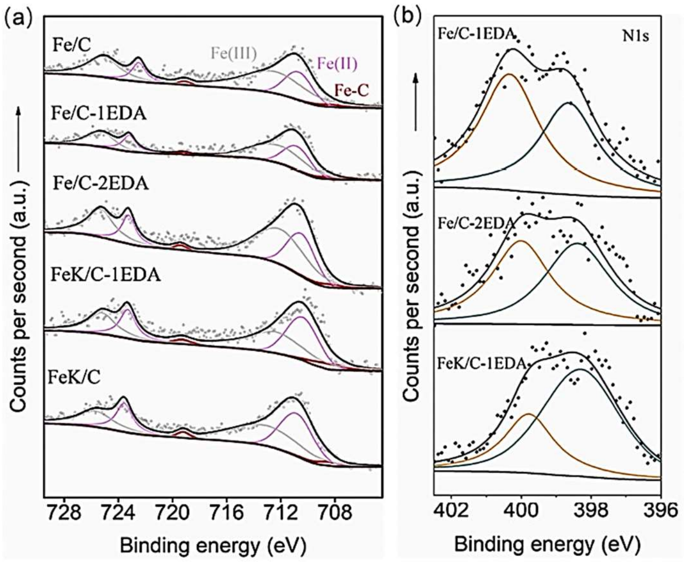

Figure 1.6 (a) Fe2p X-ray photoelectron spectra, and (b) N1s X-ray photoelectron spectra of catalysts investigated. In Figure 1.6b, orange line represents pyrrolic nitrogen, and green line represents pyridine nitrogen.

Previous studies have shown that different nitrogen configurations can affect the catalytic performance. Therefore, N1s XPS spectra of different nitrogen-doped catalysts were deconvoluted and compared as shown in Figure 1.6b. The existence of nitrogen in carbon support can change the electron donor state, such as the enhancement of electron density near the Fermi level. The amount of surface nitrogen atoms is listed in Table 1.3, and the concentration of surface nitrogen is between 6 at. % and 7 at. % (atom ratio). The metal-like promotional effect is generally ascribed to pyridine-like structures [13,17]. Nitrogen from the pyridine like structure shows higher electron density than that of pyrrolic nitrogen groups, and this high electron density nitrogen atom is more conducive to stabilizing the Fe–C bond. As seen, compared with Fe/C-1EDA, the content of pyridine-like structures over Fe/C-2EDA increases slightly. However, with the further addition of K promoter, the pyridine like nitrogen content increases significantly, which is indicative that the presence of K promoter is beneficial for the formation of pyridine-like nitrogen.

Table 1.2 Surface composition of spent doped iron-based catalysts. [a]

Catalyst	Composition from Fe2p (mol. %)		
	Fe(III)	Fe(II)	Fe-C
Fe/C	67.2	29.4	3.4
Fe/C-1EDA	59.2	35.3	5.5
Fe/C-2EDA	62.0	34.7	3.3
FeK/C-1EDA	52.4	42.0	5.6
FeK/C	51.1	44.3	4.6

[a] Data obtained from XPS measurements.

Table 1.3 N atom incorporation amount according to XPS analysis. [a]

Catalyst	N atom content (atom. %)
Fe/C-1EDA	6.0
Fe/C-2EDA	6.7
FeK/C-1EDA	7.0

[a] Data obtained from XPS measurements.

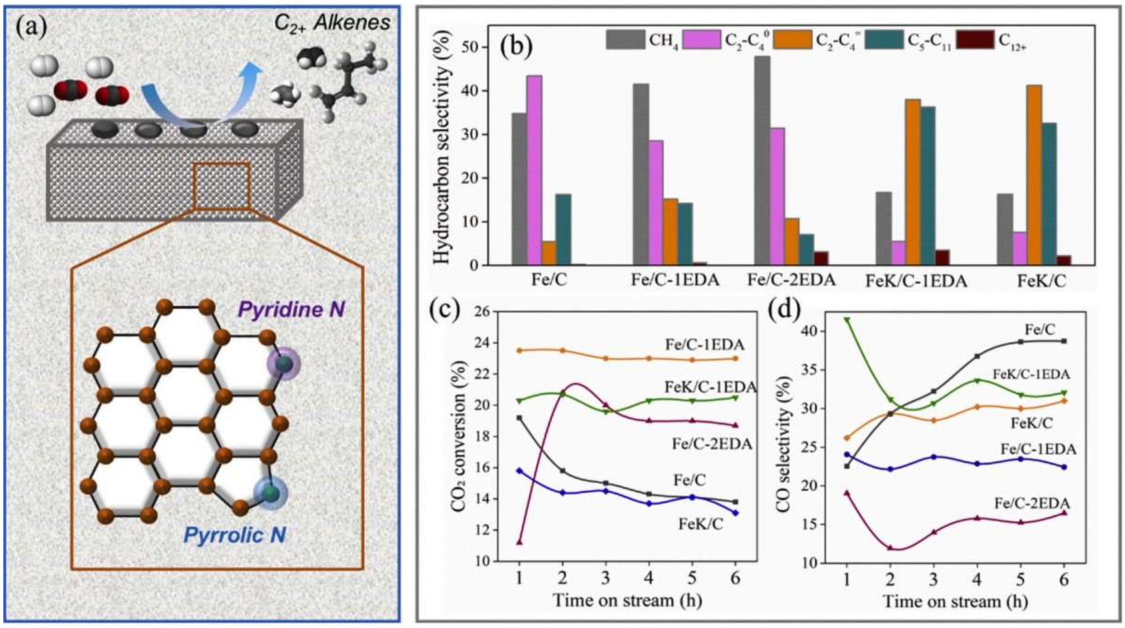

Figure 1.7 (a) Schematic diagram of CO_2 hydrogenation over a nitrogen incorporation into carbon-supported catalyst; (b) Hydrocarbon selectivity distribution over different catalysts, data collected at 6 h TOS; (c) CO_2 conversion vs time on stream; (d) CO-selectivity vs time on stream. Reaction conditions (Figure 1.7b, d): 300 °C, 1.0 MPa, 12 g h mol^{-1}.

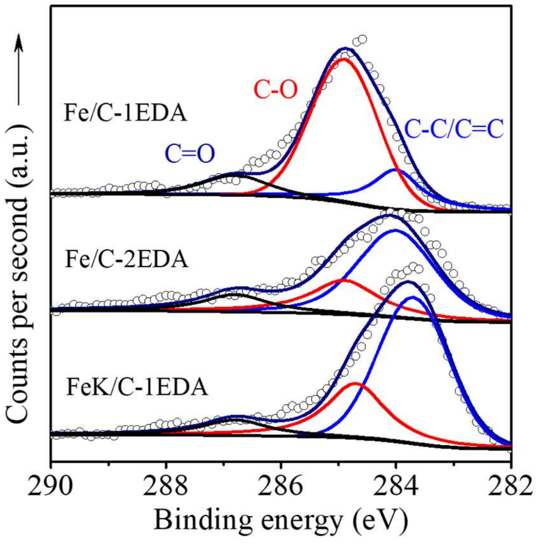

Figure 1.8 High resolution of C1s spectra of different catalysts

1.3.5 Catalytic performance evaluation

The catalytic performance of different catalysts investigated for the CO_2 hydrogenation are depicted in Figure 1.7 and Table 1.4. As for the reference Fe/C catalyst, the main hydrocarbon products are low-carbon saturated hydrocarbons. CO_2 conversion is 14.1%, and the CO selectivity is 38.7%. In contrast, the catalytic performance changes obviously with the incorporation of nitrogen atoms (see Fe/C-1EDA). While the catalytic activity increases from 14.1 to 22.8%, the CO selectivity decreases from 38.7 to 22.9%. Meanwhile, the hydrocarbon distribution shifts from saturated light hydrocarbons to alkenes (Table 1.4). As discussed above (Table 1.1, Figures 1.3 and 1.6), with the incorporation of nitrogen atom, uniform distribution of small-size carbides particles is formed, which is crucial for enhancing CO_2 conversion, thus leading to an enriched $-CH_2$ surface concentration and finally boosting C–C coupling towards more alkenes. Besides, improved surface CO_2 adsorption properties are also beneficial for alkenes formation. As a consequence, Fe/C-1EDA presents a high catalytic activity as well as high C_{2+}-olefin selectivity. However, for the Fe/C-2EDA catalyst, the catalytic performance is inferior to that of Fe/C-1EDA. According to the XPS spectra (Figure 1.6 and Table 1.2), it has a lower content of carbides compared to Fe/C-1EDA catalyst. However, it presents a high content of Fe^{II} species than Fe/C, thus showing a higher conversion than Fe/C but a lower conversion than Fe/C-1EDA. Meanwhile, owing to the inferior CO_2 adsorption (and lower surface CO_2/H ratio), the C_{2+}-olefin selectivity decreases. Characterization results and reaction data clearly show that the doping of nitrogen atom, as a favorable means, can significantly improve the performance of the present catalytic reaction, especially the light olefins selectivity.

Table 1.4 Catalytic performances of different catalysts for CO_2 hydrogenation.

Catalyst	CO_2 conv. (%)	CO sel. (%)	Hydrocarbon selectivity (C-mol %)					O/P ratio
			CH_4	C_2-C_4^o	C_2-$C_4^=$	C_5-C_{11}	C_{12+}	
Fe/C	14.1	38.7	34.8	43.4	5.4	16.2	0.2	0.1
Fe/C-1EDA	22.8	22.9	41.5	28.5	15.2	14.2	0.6	0.3
Fe/C-2EDA	18.7	15.8	47.8	31.4	10.7	7.0	3.1	0.2
FeK/C-1EDA	20.1	31.7	17.2	5.6	37.7	35.9	3.6	1.2
FeK/C	13.1	54.7	16.3	7.6	41.2	32.5	2.4	1.4

Reaction conditions: $H_2/CO_2 = 3:1$, 1.0 MPa, 300 °C, W/F=12 g h mol^{-1}; C_2-C_4^o: saturated C_2-C_4 hydrocarbon; C_2-$C_4^=$: C_2-C_4 olefins; O/P: olefins/paraffin ratio.

As another effective strategy, the addition of alkaline metal promoters, especially K_2O, is widely used to improve the catalytic performance by improving CO_2 adsorption, weakening olefin hydrogenation and enhancing carbides content. Thus, K doping is further investigated. As illustrated in Figure 1.7b, with the addition of K, hydrocarbon distribution changes obviously. The selectivity of heavy hydrocarbons (C_{5+}) increases from 16.4% in Fe/C to 34.7% in FeK/C-1EDA, more than two times. The high CO-selectivity may be ascribed to the promotional effect of K promoter for the RWGS reaction, which has been demonstrated by others [27]. For FeK/C-1EDA catalyst, while maintaining a high activity, it shows a lower CO-selectivity. Besides, its heavy hydrocarbon selectivity is higher than that of FeK/C. As described above, the addition of alkali K promotes the formation of iron carbide species. However, pyridine nitrogen can provide electrons and make carbide rich in electrons, thus there is a mutually promoting effect between these two factors for catalyzing the CO_2 hydrogenation reaction. It is believed that there is synergistic effect between K and pyridine nitrogen. The synergistic effect between K^+ and nitrogen species significantly improves the reaction performance, which might be due to the high pyridine-like structure content and surface adsorption performance (Figures 1.4 and 1.6). More importantly, the existence of nitrogen atom is beneficial for the formation of small-size iron carbides (Table 1.1 and Figure 1.3). To some extent, the surface molar ratio of Fe to C indicates that it is easier to produce small-size iron carbides.

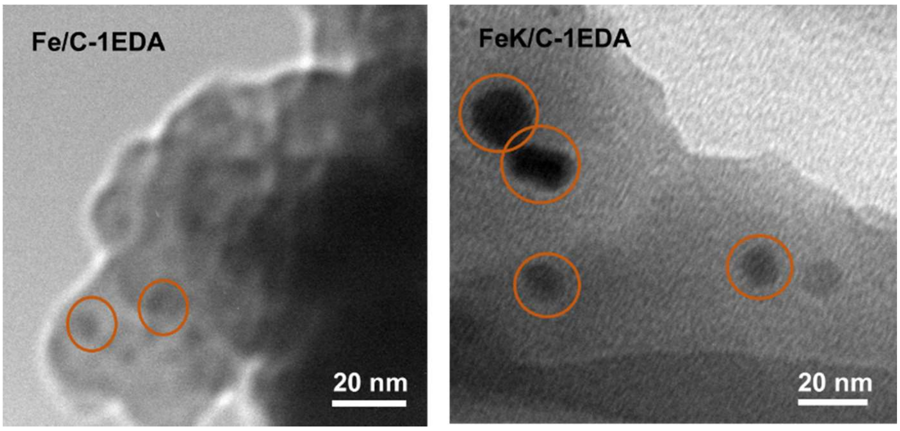

Figure 1.9 Typical TEM images of spent Fe/C-1EDA and FeK/C-1EDA.

TEM images also demonstrated the good distribution of small-size iron oxide particles (Figure 1.9). Fe carbides with the size between 5 and 30 nm was reported to be suitable to accelerate the formation of longer alkenes [17,18]. Chain propagation of hydrocarbon is a structure sensitive reaction, and small-size iron carbides have a high chain propagation ability [18,28], thus it shows a benign performance than FeK/C catalyst (Table 1.1 and Table 1.3). In addition, the changes of catalytic activity and CO-selectivity over time-on-stream are shown in Figure 1.7c and d respectively. Compared with the reference catalyst (Fe/C), Fe/C-1EDA shows higher activity and lower selectivity of the undesired CO. More importantly, catalysts with suitable addition of EDA agents have a shorter induction period, which is important for potential industrial applications. Even compared with other related reported state of-the-art Fe-based catalysts, FeK/C-1EDA presents a rather high heavy hydrocarbon selectivity (C_{5+}). It indicates that the catalyst with both nitrogen incorporation and alkali K promoter is a promising means for efficiently catalyzing the CO_2 hydrogenation into valuable products.

1.4 Conclusions

Ethylene diamine (EDA) as a nitrogen source was applied to tune carbon support surface chemical properties, achieving an outstanding performance for the CO_2 hydrogenation process. Combining characterization and reaction data, it was found that nitrogen incorporation into the carbon support contributes to the high dispersion of active iron oxide phase, and to the formation of small-size iron carbides, which is beneficial for the formation of olefins. Meanwhile, enhanced surface basicity resulted from suitable nitrogen doping, which also boosts the selective formation of olefins. In addition, further utilization of electronic K promoter adjusts iron carbide's electron density, thus promoting chain propagation of C_xH_{y-s} adsorbed intermediates. Correspondingly, the catalyst with both nitrogen incorporation into the carbon support structure and potassium modification presents benign catalytic activity as well as higher olefin-rich hydrocarbon selectivity. Nitrogen incorporation into a carbon support material provides a promising means for regulating their electronic structure and active sites distribution of doped-carbon supported iron oxides, to achieve an enhanced catalytic CO_2 hydrogenation performance.

References

[1] R. Ye, J. Ding, W. Gong, M.D. Argyle, Q. Zhong, Wang Y, C.K. Russell, Z. Xu, A.G. Russell, Q. Li, M. Fan, Y. Yao, Nat. Commun., 2019, 10, 5698.

[2] C. Hepburn, E. Adlen, J. Beddington, E.A. Carter, S. Fuss, N.M. Dowell, J.C. Minx, P. Smith, C.K. Williams, Nature, 2019, 575, 87.

[3] W. Wang, S. Wang, X. Ma, J. Gong. Chem. Soc. Rev., 2011, 40, 3703-3727.

[4] W. Zhou, K. Cheng, J. Kang, C. Zhou, V. Subramanian, Q. Zhang, Y. Wang, Chem. Soc. Rev., 2019, 48, 3193-3228.

[5] L. Guo, J. Sun, Q. Ge, N. Tsubaki, J. Mater. Chem. A, 2018, 6, 23244-23262.

[6] X. Liu, M. Wang, C. Zhou, W. Zhou, K. Cheng, J. Kang, Q. Zhang, W. Denga, Y. Wang, Chem. Commun., 2018, 54, 140-143.

[7] R.W. Dorner, D.R. Hardy, F.W. Williams, H.D.Willauer, Catal. Comm., 2011, 15, 88-92.

[8] P. Gao, S. Li, X. Bu, S. Dang, Z. Liu, H. Wang, L. Zhong, M. Qiu, C. Yang, J. Cai, W. Wei, Y. Sun, Nat. Chem., 2017, 9, 1019-1024.

[9] L. Tan, P. Zhang, Y. Cui, Y. Suzuki, H. Li, L. Guo, G. Yang, N. Tsubaki, Fuel Process. Technol., 2019, 196, 106174.

[10] Y. Wang, L. Tan, M. Tan, P. Zhang, Y. Fang, Y. Yoneyama, G. Yang, N. Tsubaki, ACS Catal., 2019, 9, 895-901.

[11] L. Guo, J. Li, Y. Cui, R. Kosol, Y. Zeng, G. Liu, J. Wu, T. Zhao, G. Yang, L. Shao, P. Zhan, J. Chen, N. Tsubaki, Chem. Comm., 2020, 56, 9372-9375.

[12] W.D. Shafer, G. Jacobs, U.M. Graham, H.H. Hamdeh, B.H. Davis, J. Catal., 2019, 396, 239-248.

[13] L. Guo, P. Zhang, Y. Cui, G. Liu, J. Wu, G. Yang, Y. Yoneyama, N. Tsubaki, ACS Sustainable Chem. Eng., 2019, 7, 8331-8339.

[14] N. Boreriboon, X. Jiang, C. Song, P. Prasassarakich, J. CO_2 Util., 2018, 25, 330-337.

[15] G. Liu, Q. Chen, E. Oyunkhand, S. Ding, N. Yamane, G. Yang, Y. Yoneyama, N. Tsubaki, Carbon, 2018, 130, 304-314.

[16] H. Xiong, L.L. Jewell, N.J. Coville, ACS Catal., 2015, 5, 2640-2658.

[17] H. Xiong, M. Moyo, M. Motchelaho, Z. Tetana, S. Dube, L.L. Jewell, N.J. Coville, J. Catal. 2014, 311, 80-87.

[18] H. Xiong, M. Moyo, M. Motchelaho, L.L Jewell, N.J. Coville, Appl. Catal. A, 2010, 388, 168-178.

[19] B. Liang, T. Sun, J. Ma, H. Duan, L. Li, X. Yang, Y. Zhang, X. Su, Y. Huang, T. Zhang, Catal. Sci. Technol., 2019, 9, 456-464.

[20] J. Wei, Q. Ge, R. Yao, Z. Wen, C. Fang, L. Guo, Y. Xu, J. Sun, Nat. Commun., 2017, 8, 15174-15181.

[21] P. Zhai, C. Xu, R. Gao, X. Liu, M. Li, W. Li, X. Fu, C. Jia, J. Xie, M. Zhao, X. Wang, Yong. Li, Q. Zhang, X. Wen, D. Ma, Angew. Chem. Int. Ed., 2016, 55, 1-7.

[22] C.G. Visconti, M. Martinelli, L. Falbo, A. Infantes-Molina, L. Lietti, P. Forzatti, G. Iaquaniello, E. Palo, Ba. Picutti, F. Brignoli, Appl. Catal. B, 2017, 200, 530-542.

[23] J. Wei, J. Sun, Z. Wen, C. Fang, Q. Ge, H. Xu, Catal. Sci. Technol., 2016, 6, 4786-4793.

[24] G. Yu, B. Sun, Y. Pei, S. Xie, S. Yan, M. Qiao, K. Fan, X. Zhang, B. Zong, J. Am. Chem. Soc., 2010, 132, 935-937.

[25] L. Guo, J. Sun, X. Ji, J. Wei, Z. Wen, R. Yao, H. Xu, Q. Ge, Commun. Chem., 2018, 1, 11.

[26] L. Guo, Y. Cui, H. Li, Y. Fang, R. Prasert, J. Wu, G. Yang, Y. Yoneyama, N. Tsubaki, Catal. Comm., 2019, 130, 105759.

[27] M. Amoyal, R. Vidruk-Nehemya, M..V. Landau, M. Herskowitz, J. Catal., 2017, 348, 29-39.

[28] H.M.T Galvis, J.H. Bitter, T. Davidian, M. Ruitenbeek, A.I. Dugulan, K.P. Jong, J. Am. Chem. Soc., 2012, 134, 16207-16215.

Chapter 2

Heteroatom doped iron-based catalysts prepared by urea self-combustion method for efficient CO_2 hydrogenation

A serial of spinel-like structure catalysts are successfully fabricated through urea self-combustion method instead of traditional iron-based catalyst preparation process.

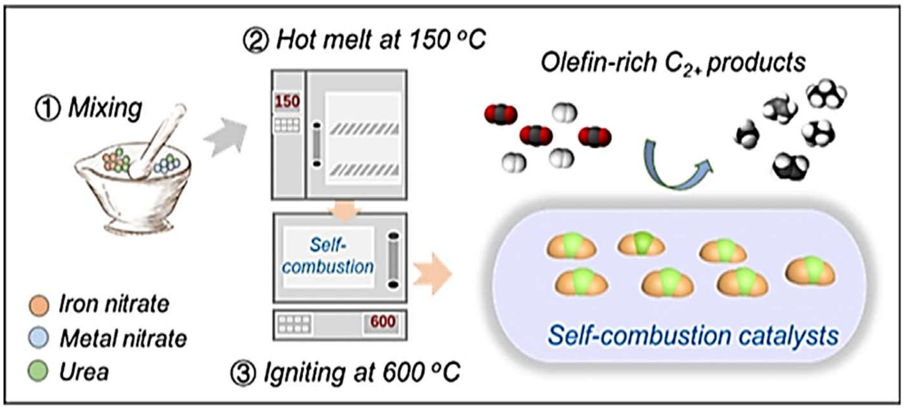

Abstract

This work describes a novel route for the fabrication of heteroatom doped iron-based catalysts (spinel-like structure) through urea self-combustion method, and catalytic performances over these self-combustion catalysts are investigated in detail. It is found that catalytic performances are affected by the properties of doped metals. Owing to the high methanation activity of Ni and Co, $NiFe_2O_x$ and $CoFe_2O_x$ catalysts present high CH_4 selectivity compared to Fe_2O_3 catalysts. $MgFe_2O_x$ exhibits high olefin hydrogenation ability. By contrast, the utilization of Cu and Zn promotes catalytic activity and olefins selectivity via regulating surface CO_2 adsorption and carbides content. Among these spinel catalysts, the $ZnFe_2O_x$ catalyst shows the best CO_2 hydrogenation performance. Enhanced CO_2 adsorptions as well as active species of carbides result in the benign hydrogenation behavior. Meanwhile, the effects of Zn/Fe molar ratio are also investigated. It is worth noting that the catalytic performance can be improved regardless of the added amount of Zn promoter. Nevertheless, the catalytic performance reaches the best level when the Zn/Fe molar ratio equals 1/2. The proposed method provides a new strategy different from traditional catalyst preparation process for catalytic hydrogenation of CO_2 into highly valuable products.

Keywords: CO_2 hydrogenation, Spinel structure, Iron catalyst, Olefins, Bimetallic catalyst

2.1 Introduction

Although the utilization of carbon-rich resources such as petroleum and goal greatly promotes the rapid development of economic society, the on-going rise of carbon dioxide (CO_2) concentration aggravates a series of environmental problems related to ocean acidification and climate change [1–3]. These challenges above compel human being to seek appropriate routes to reduce the concentration of CO_2 in the atmosphere. Combined with CO_2 capture and storage (CCS), catalytic conversion of CO_2 to valuable chemicals (e.g., olefins, isoparaffins, aromatics and methanol) or high-energy fuels (for example, gasoline) is a promising means which not only reduces the concentration of CO_2, but also creates economic benefits [4–20]. However, the chemical inertness of CO_2 molecules and imprecise control of chain propagation process lead to the poor catalytic performance including activity and product selectivity until now [21].

It is well accepted that CO_2 hydrogenation to hydrocarbons can be achieved through a methanol-mediated process or modified Fischer-Tropsch synthesis (FTS) process [21]. Iron-based catalysts, as potential catalysts, have been intensively investigated for CO_2 hydrogenation via a modified FTS since they contain two kinds of active sites responsible for CO_2 activation to CO intermediates and C–C bond propagation simultaneously. In order to improve performance such as light olefin selectivity, heteroatom doping strategy is generally adopted by tailoring the electron density of iron species, active site distribution, surface basicity, etc., to suppress undesired CH_4 and light saturated hydrocarbon selectivity [22–24].

Generally, traditional Co-based catalysts show good activity and chain propagation ability for FTS process. However, the chain growth capacity is significantly reduced when the reaction gas is switched from CO to CO_2. Different from Fe-based catalysts, Co has a low reverse water–gas shift (RWGS) activity and high C-C propagation ability. Therefore, in recent years, constructing a bimetallic Co-Fe catalyst by combining the merits of cobalt and iron metal was applied as an efficient catalyst for CO_2 hydrogenation [25–27]. Generally, the doping of Co can improve the catalytic performance, especially the selectivity of C_{2+} hydrocarbon, by influencing H*/CO* species ratio or hydrogenation ability. Furthermore, the co-existence of Co further improves FTS performance by promoting CO activation process [28]. Different from Co-based catalysts, Cu-based catalysts exhibit a benign activity for RWGS reaction but no methanation ability [29]. Thus, the utilization of Cu promotes the formation of reaction intermediate through catalyzing RWGS reaction, followed by chain growth reaction on iron carbides, which shows an improved catalytic performance, such as high conversion and boosted C_{2+} product selectivity. However, the combination manner and presence state between Fe and Cu elements will affect the product distribution as well as the dominant reaction pathway [30–34]. As for a Cu-Fe bimetallic catalyst, CO* is the preferred intermediate product with low surface Cu coverage (atom layer of 2/9 or below) while HCOO* intermediate path is favorable with high Cu coverage (atom layer of 4/9 or higher) [32,33]. Besides, non-precious Ni metal has also been intensively investigated for CO_2 hydrogenation [35–37]. Previously, it is reported that a bimetallic Fe–Ni system catalyst exhibits favorable behaviors for FTS activity as well as heavy hydrocarbon selectivity than pure Fe catalyst [38]. The utilization of another metal (Ni) enhances the chain growth probability (α), and the bimetallic system has an optimal molar ratio of metal to Fe during FTS reaction [38]. Moreover, Ni addition may also improve the dispersion of iron oxides and decreases the crystallite size of metal oxides [39]. Unlike FTS reaction process, the main product occurring on Ni-Fe catalysts is generally methane when the reaction gas is switched from CO to CO_2 [36,40]. Generally, the introduction of alkali-earth Mg promoter could regulate the reduction, carburization, or/and hydrogenation behaviors in FTS process to improve catalytic performance such as olefin ratio [41,42]. However, different from a conventional FTS process, few reports have investigated the promotional effect of Mg additives on CO_2

hydrogenation [43,44]. On the contrary, as for Zn promoter, it is generally considered as structural promoter to add into iron-based catalyst system [45]. In addition, Zn acting as a base could also generate more basic carbide species, and retard the reabsorption of olefins by tailoring surface adsorption behaviors [46,47], thus improving light olefin formation. Zinc, as a structural promoter, can also stabilize the catalytic performance by inhibiting carbides sintering [48]. Although Zn is used as a structural promoter to enhance CO_2 hydrogenation performance, the effects of Zn incorporation on structure and properties have not been addressed well.

Up to now, most of iron-based catalysts are prepared by precipitation method or impregnation method. An alternative means for preparing efficient Fe-based catalysts is an important research area. Herein, we fabricate a series of heteroatom doped iron-based (M-Fe, M = Co, Ni, Mg, Cu, Zn) catalysts synthesized through a novel urea self-combustion method instead of traditional preparation method. Different from common precipitation or impregnation process, urea self-combustion method can significantly reduce the preparation steps.Meanwhile, there is no extra introduction of liquid reagents (for example, H_2O) in the preparation process of catalyst, and a series of operations such as drying and washing are also avoided. Although González-Cortés et al. used the combustion method to prepare the supported catalysts, here we focus on directly preparing the different non-supported catalyst with a good spinel structure by the combustion method [49].

Based on the above discussion, it can be easily realized that the utilization of this method can significantly reduce the catalyst preparation cost and production cycle. These alloy catalysts are employed as prototype catalysts to investigate the influence of the second metal on the catalytic performance. Besides, the effects of second metal on reducibility, surface adsorption capacity and carburization ability are also investigated in detail.

2.2 Experimental section

2.2.1 Catalyst preparation

Reference catalyst and doped catalysts were synthesized through urea self-combustion method. Briefly, $Fe(NO_3)_3 \cdot 9H_2O$ of 0.01 mol and urea of 0.022 mol melt at 150 °C for 10 min. There into, the molar ratio of urea to metallic nitrate was 2.2 [50]. After mixing well, it was then transferred to 600 °C muffle furnace to burn for 30 min. Subsequently, the products were calcined for 4 hours at 700 °C. The corresponding catalyst was labeled as Fe_2O_3. As for heteroatom doped iron catalysts, similar processes were adopted for preparation of MFe_2O_x, in which 2 stands for molar ratio of Fe/M during fabrication steps. Similar processes were adopted for the fabrication of $NiFe_2O_x$, $CoFe_2O_x$, $MgFe_2O_y$, $ZnFe_2O_x$, and $CuFe_2O_x$. Metal composition of doped iron-based catalysts was also examined via different techniques and listed in Table 2.1 and Table 2.2. For example, Zn $(NO_3)_2 \cdot 6H_2O$ of 0.01 mol, urea of 0.066 mol, and Fe $(NO_3)_3 \cdot 9H_2O$ of 0.02 mol melt at 150 °C for 10 min. After mixing well, it was then transferred to 600 °C muffle furnace to burn for 30 min. Afterwards, the products were calcined for 4 hours at 700 °C to obtain the $ZnFe_2O_x$ structure catalyst. As for Zn doped iron catalysts, similar processes were adopted for preparation of $ZnFeMO_x$, in which M (M = 1, 2, 4, 8) stands for the varied molar ratio of Fe/Zn during fabrication steps.

Table 2.1 Metal composition of doped iron-based catalysts.[a]

Entry	Catalyst	Metal Composition (mol.%)		Metal/Fe (molar ratio)
		Metal	Fe	
1	Fe_2O_3	/	100	/
2	$CoFe_2O_x$	35.5	64.5	1.82
3	$NiFe_2O_x$	34.9	65.1	1.87
4	$MgFe_2O_x$	34.7	65.3	1.88
5	$CuFe_2O_x$	35.4	64.6	1.82
6	$ZnFe_2O_x$	34.6	65.4	1.89

[a] Data obtained from EDX measurements.

Table 2.2 The elemental composition of different catalysts. [a]

Catalyst	Composition of element /wt%		
	Metal	Fe	O
$NiFe_2O_x$	23.1	45.2	31.7
$CoFe_2O_x$	24.6	44.1	31.3
$MgFe_2O_x$	11.3	57.2	31.5
$CuFe_2O_x$	27.4	47.1	25.5
$ZnFe_2O_x$	26.1	47.6	26.3

[a] Data obtained from EDX measurements.

2.2.2 Catalyst characterization

XRD patterns were recorded on a Rigaku RINT 2400 X-ray Diffractometer equipped with Cu-Ka (40 kV, 40 mA) irradiation. Scans were recorded in the 2θ range of 5–90° with a step size of 0.02°/s. A JEOL JSM-6360LV microscope was used to analyze structural information. The X-ray photoelectron spectroscopy (XPS) analysis was conducted on Thermo Fisher Scientific ESCALAB 250Xi multifunctional X-ray photoelectron spectroscopy. The adsorption and reduction properties of as-prepared catalysts were determined by a BELCAT-II-T-SP Characterization System. For H_2-TPR conditions, firstly, the catalyst (50 mg) was dried at 400 °C for 60 min in a flow of pure Ar of 40 mL min^{-1}, and then cooled down to 50 °C. Subsequently, the catalyst was exposed in flowing H_2/Ar at 50–550 °C with a heating rate of 10 °C min^{-1}. As for CO_2-TPD conditions, 50 mg catalyst was reduced at 400 °C for 120 min in a flow of pure H_2 of 40 mL min^{-1}, and then cooled down to 40 °C. After that, the corresponding catalyst was exposed in flowing pure CO_2 for 60 min with 40 mL min^{-1}, followed by flushing in Ar for 30 min. Finally, the measurement was conducted at 50–550 °C with a heating rate of 10 °C min^{-1}. The analysis of element composition was also evaluated by a PHILIPS PW2404R X-ray spectrometer. High-resolution transmission electron microscopy (HR-TEM) images for spent catalysts were obtained using a TOPCON EM-002B at 120 kV. Inductively Coupled Plasma Optical Emission Spectrometer (ICP-OES) was adopted to determine the content of different elements.

2.2.3 Catalyst activity evaluation

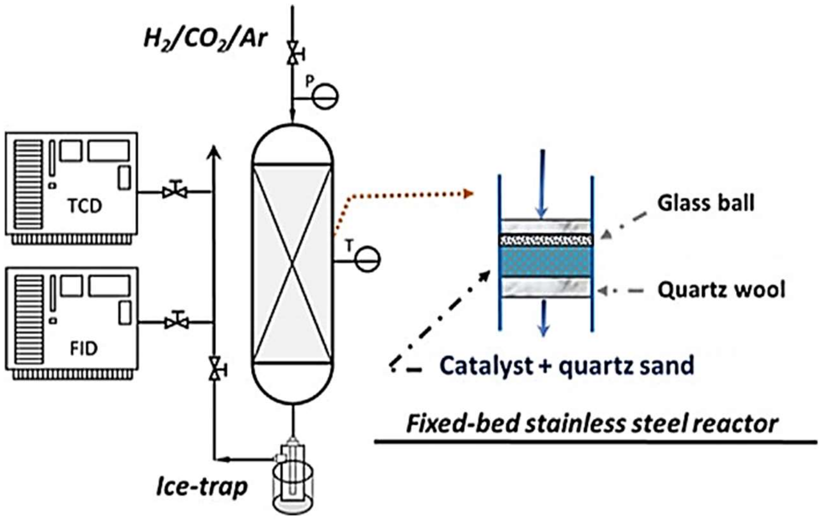

Scheme 1. Detailed reaction system for CO_2 hydrogenation.

CO_2 hydrogenation reaction was conducted in a stainless steel fixed-bed reactor (Scheme 1). Firstly, the as-prepared catalyst of 0.5 g diluted with 0.5 g quartz granule was in situ reduced at 400 °C for 8 h using pure H_2 flow (40 mL min^{-1}, atmospheric pressure) to fully expose the active sites. Afterwards the temperature dropped to the reaction temperature, and then the reactant gas mixtures including $CO_2/H_2/Ar$ (27.1 v%, H_2: 60.58 v%, Ar: 5.32 v%) were fed into the reactor. Meanwhile, the pressure rose to 1.0 MPa. N-octane as solvent was loaded in ice trap to capture the liquid hydrocarbons in the effluent. The obtained liquid hydrocarbons were analyzed by an off-line gas chromatograph using a flame ionization detector. CO_2 conversion, CO selectivity, and hydrocarbons selectivity were calculated according to Eqs. (1), (2), and (3), respectively.

$$CO_2\ _{\text{conversion}}\ (/\%) = \frac{CO_{2in}-CO_{2out}}{CO_{2i}} x100 \qquad (1)$$

$CO_{2\,in}$: mole fraction of CO_2 in the inlet, $CO_{2\,out}$: mole fraction of CO_2 in the outlet.

$$CO\ _{\text{selectivity}}\ (/\%) = \frac{CO_{out}}{CO_{2in}-CO_{2out}} x100\% \qquad (2)$$

CO out: mole fraction of CO in the outlet.

$$C\ _{\text{i hydrocarbon selectivity (C-mol/\%)}} = \frac{Mole\ of\ C\ i\ hydrocarbon\ \ x\ i}{\Sigma_{i=1}^{n}\ Mole\ of\ C\ i\ hydrocarbo\ \ x\ i} x\ 100\% \qquad (3)$$

2.3 Results and discussion

2.3.1 Surface morphology of catalyst

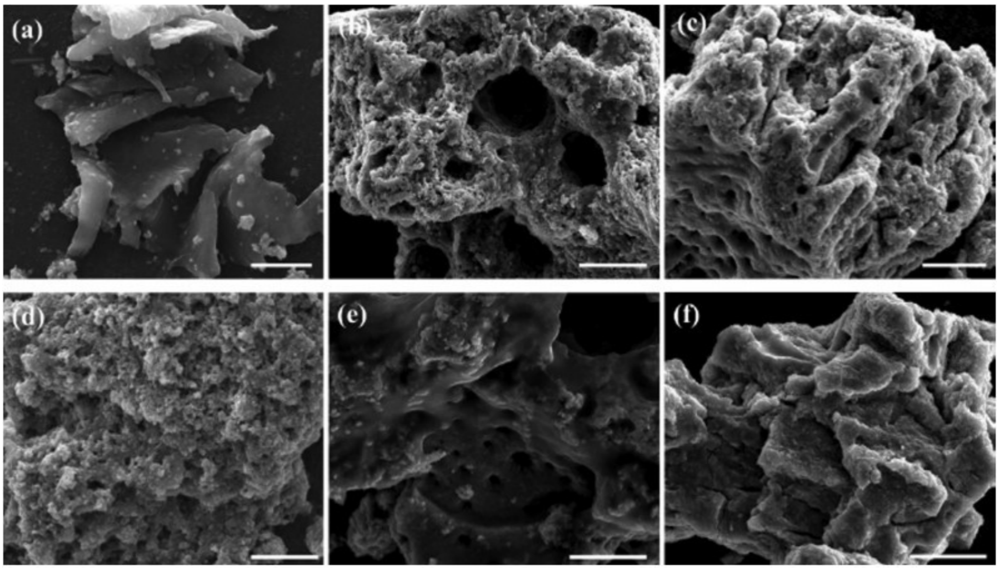

Figure 2.1 SEM images of different self-combustion catalysts. (a) Fe_2O_3, (b) $NiFe_2O_x$, (c) $CoFe_2O_x$, (d) $MgFe_2O_x$, (e) $CuFe_2O_x$, (f) $ZnFe_2O_x$. The scale bar in the images stands for 10 μm.

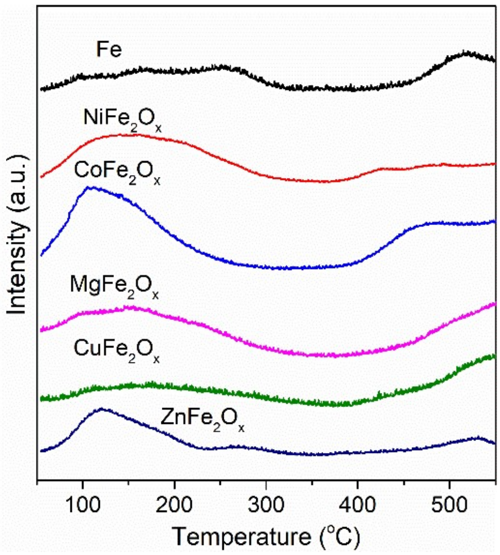

Figure 2.2 CO_2-TPD patterns normalized by relative specific surface area of different self-combustion catalysts.

The morphology and structure of as-prepared self-combustion catalysts are shown in Figure 2.1. As shown in Figure 2.1a, the fresh Fe_2O_3 catalyst presents smooth flaky structure. By contrast, the introduction of the second metal significantly changes the catalyst structural morphology. As for Ni metal incorporation (Figure 2.1), the catalyst surface shows a rather rough structure with a hollow structure of varying sizes. These surface pores are caused by bubbles formed during spontaneous combustion of the catalyst. With the addition of Co metal (Figure 2.1c), the surface of catalyst also presents a rough morphology, although its cavity structure is small than that of Ni-doped one. For the introduction of Mg (Figure 2.1d), the catalyst surface exhibits a finer roughness. As for the doping of Cu metal (Figure 2.1e), the surface roughness is lower than above three metal-modified ones with hole structures of different sizes on the catalyst surface. For the Zn metal (Figure 2.1f), the catalyst surface presents a rough interface of different sizes. Obviously, the utilization of doping metal changes the morphology and structure of as-prepared self-combustion catalysts, and the introduction of different doped metals has varied effects on the morphology and structure. In addition, the specific surface areas of different catalysts are characterized (Table 2.3). Compared with iron catalysts (Fe_2O_3), the specific surface area of the catalysts can be increased through heteroatoms incorporation except for the doping of Co metal. In particular, the doping of Zn significantly increases the specific surface area. Besides, the change of catalyst surface area may be due to the regulation of morphology by doped metal.

TEM images of spent catalysts are also characterized and shown in Figure 2.2. As seen, the particle size of the Fe_2O_3 catalyst after reaction is between 20 and 30 nm. However, with the incorporation of Ni, Co, or Mg metal, the particle size of the catalyst is significantly reduced and mainly concentrated at 15–20 nm. On the contrary, the doping of Cu or Zn increases the particle size, and the particle size is mainly about 30–40 nm. Visibly, the introduction of different heteroatoms can also change the particle size of the spent catalyst.

In order to further investigate the influence of doped metal amount on the morphologies and structures of self-combustion catalysts, SEM images of catalysts with different Zn/Fe molar ratios are compared in Figure 2.3. When the Zn/Fe molar ratio equals 1:1, the catalyst surface forms more pores indicating that more bubbles are formed during fabrication process owing to huge amounts of gas formation. As the Fe content decreases, the roughness of catalyst decreases gradually. When the molar ratio of Zn to Fe equals 1:8, the morphology and structure are similar to those of Fe_2O_3 catalyst (Figure 2.1a and Figure 2.3d). As observed, the additive amount of doped metal can adjust the morphology and structure of self-combustion catalyst, just as different metals are used.

Table 2.3 Surface area of different iron-based catalysts.

Sample	Special surface area (m^2/g)
Fe_2O_3	7.4
$NiFe_2O_x$	10.1
$CoFe_2O_x$	7.2
$MgFe_2O_x$	8.2
$CuFe_2O_x$	9.7
$ZnFe_2O_x$	13.8

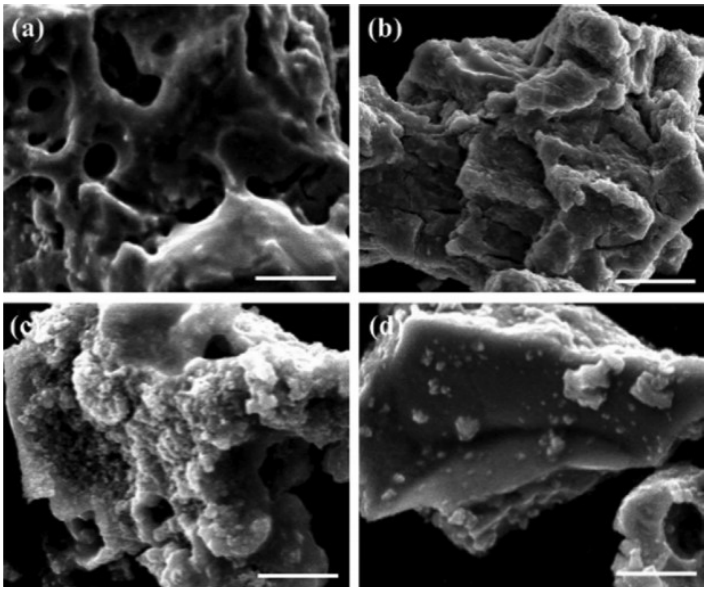

Figure 2.3 SEM images of different self-combustion catalysts. (a) ZnFeOx, (b) $ZnFe_2O_x$, (c) $ZnFe_4O_x$, (d) $ZnFe_8O_x$. The scale bar in the images stands for 10 µm.

2.3.2 Chemical phase of catalyst

The XRD patterns of different self-combustion catalysts are depicted in Figure 2.4a. As depicted, the main phase for Fe catalyst is Fe_2O_3. With the implanting of another hetero-atom metal, obvious characteristic peaks appear. These characteristic peaks are ascribed to corresponding spinel like structure phases. Apparently, the spinel-like structure catalysts can be well formed via the urea self-combustion method. Figure 2.4b shows the XRD patterns of spent self-combustion catalysts. For Fe catalyst, the main phases are Fe metal and Fe_3O_4. As for $NiFe_2O_x$ catalyst, the main phases are Fe and Ni-Fe alloy. Like those of $NiFe_2O_x$ catalyst, the main phase states of $CoFe_2O_x$ and $MgFe_2O_x$ catalysts after reaction are alloy, accompanied by metallic Fe. Different from the above-mentioned catalysts, for $CuFe_2O_x$ catalyst, the main phases after the reaction are Cu and Fe without any alloy formation. By contrast, only ZnO and Fe are formed for ZnFe2Ox catalyst after reaction. According to XRD patterns, although the introduction of different metals can form a good spinel structure phase, the phase states generated by different catalysts after reaction are determined by the properties of doped metals. There into, Ni, Co, and Mg incorporations are more conducive to the formation of alloy compounds, while Cu incorporation contributes to the formation of Cu metals after reaction (Figure 2.4b). For $ZnFe_2O_x$ catalyst, Zn is used as a structural promoter to eventually produce ZnO species. It is worth noting that although characteristic diffraction peaks of carbides do not appear in the Figure 2.4b, the presence of carbides can be detected by HR-TEM (Figure 2.5) [7]. Thus, well dispersion or/and low carbide content may account for the absence of characteristic diffraction peaks (Figure 2.4b).

Figure 2.6 shows the XRD patterns of as-prepared and spent self-combustion catalysts with different Zn/Fe molar ratio. As seen (Figure 2.5a), when the molar ratio of Zn/Fe is greater than 1/2, that is, the content of Zn is more than that of a spinel system, ZnO species will be formed besides spinel species ($ZnFe_2O_4$). However, with the Zn/Fe molar ratio below 1/2, iron oxide species (Fe_2O_3) are formed as well as spinel species. After reaction, in addition to Fe and ZnO, Fe_3O_4 also appears which should be ascribed to the reduction of Fe_2O_3 species. With the decrease of Zn species content, the diffraction intensities of characteristic diffraction peaks decrease gradually (Figure 2.5b).

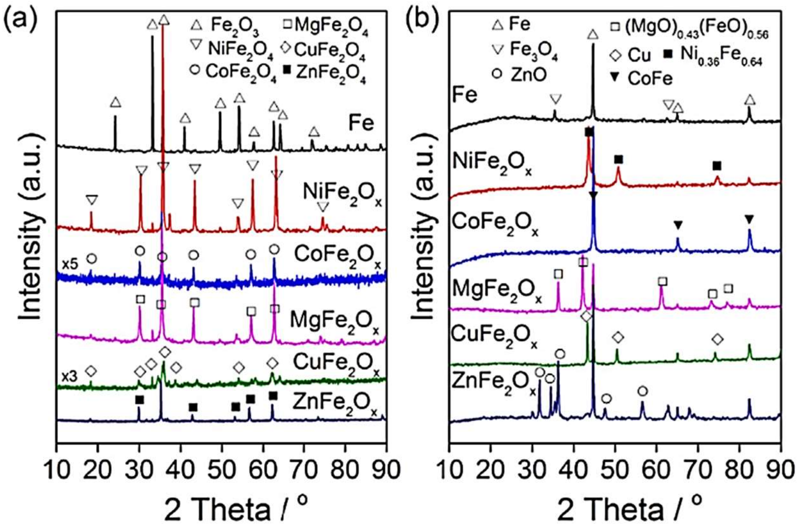

Figure 2.4 XRD patterns of (a) as-prepared self-combustion, (b) spent self-combustion catalysts

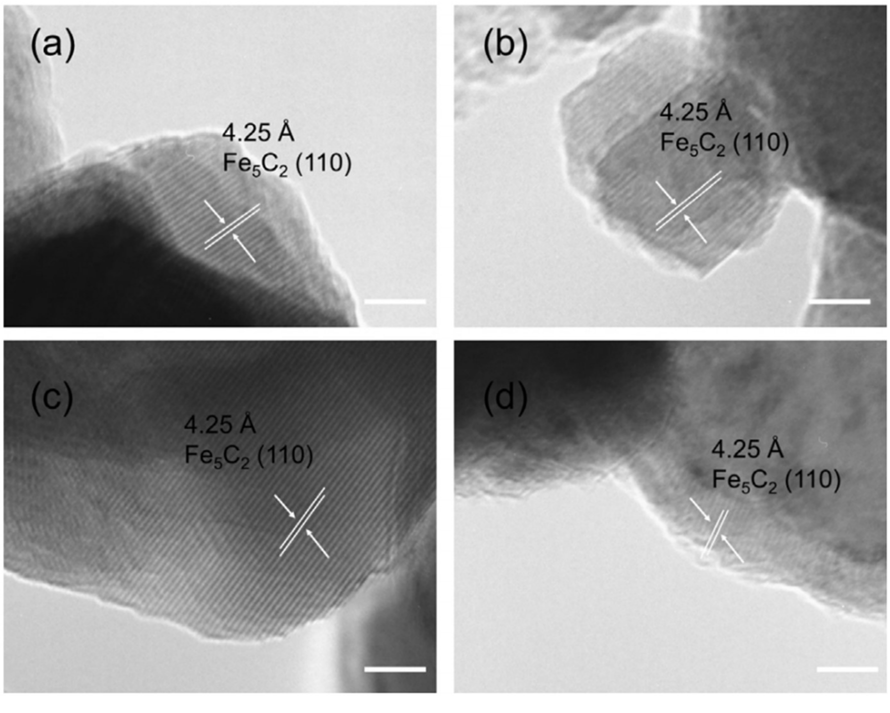

Figure 2.5 Typical TEM images of spent catalysts (a. Fe_2O_3; b. $MgFe_2O_x$; c. $CuFe_2O_x$; d. $ZnFe_2O_x$, the scare bars in the images stand for 5 nm).

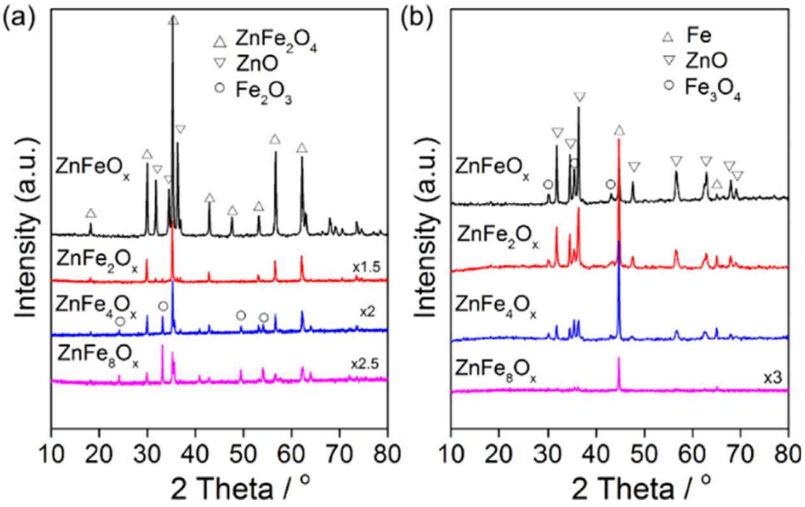

Figure 2.6 XRD patterns of (a) as-prepared and (b) spent self-combustion catalysts with different Zn/Fe molar ratio.

2.3.3 Reducibility and reactant adsorption state of catalyst

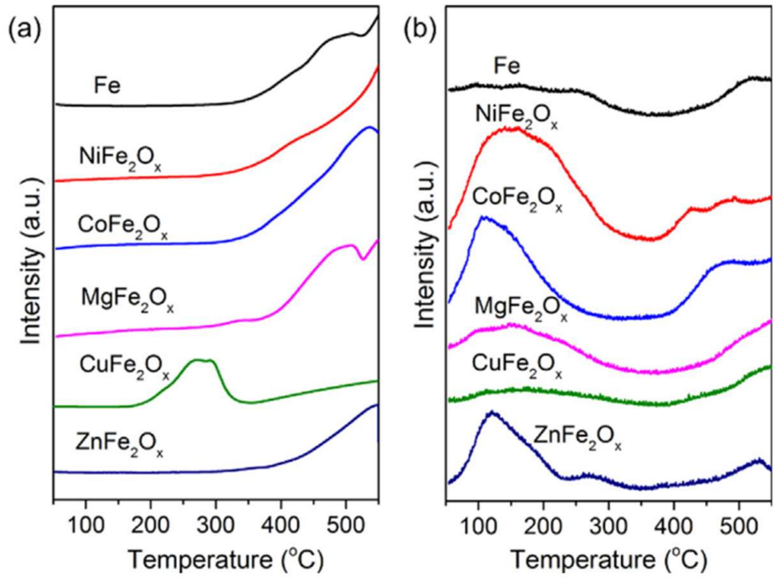

Figure 2.7 (a) H_2-TPR patterns and (b) CO_2-TPD patterns of different self-combustion catalysts.

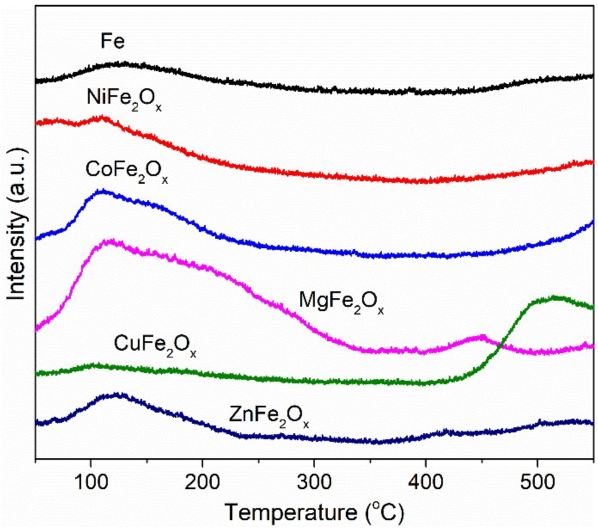

Figure 2.8 CO_2-TPD patterns of different spent self-combustion catalysts.

The reducibility of different self-combustion catalysts with another metal doping determined by H_2-TPR is presented in Figure 2.7a. For Fe_2O_3 catalyst, the peaks at around 300–400 °C and above 400 °C can be ascribed to Fe_2O_3 to Fe_3O_4 and Fe_3O_4 to Fe processes. With the introduction of Ni metal, the first reduction peak has a slight advance to the low temperature region. Similar phenomenon can also be observed for Co or Mg doping, possibly resulting from the promotion of doped metal to the reduction process of Fe species [52]. However, a major low temperature peak appears in the Cu-doped Fe-based catalyst, which can be attributed to reduction of Cu oxides [31]. By contrast, for Zn-modified self-combustion catalyst, catalyst reduction does not show favorable improvement, which indicates that Zn adding is not beneficial for the reduction process as behaved by Ni, Co, and Cu metal to reduction process. In addition, CO_2 reactant adsorption states over different self-combustion catalysts are also investigated (Figure 2.7b). Different from reduction process, the utilization of different metal doping exhibits visible difference. For single Fe catalyst, the weak adsorption peak among 100 to 350 °C which can be ascribed to weakly or moderately bonded CO_2 species, and strong adsorption peak above 400 °C corresponding to chemisorbed CO_2 or carbonate species are weak. For those self-combustion bimetallic catalysts, weak adsorption peaks as well as strong adsorption peaks increase visually. Although the addition of heteroatomic metals improves the adsorption of CO_2 on the catalyst surface, the utilization of Ni, Co, and Zn improves the adsorption performance more dramatically than Mg and Cu modified ones.

Meanwhile, in order to take the catalyst specific surface factor into account, the CO_2 adsorption strength relative to the specific surface are also considered and shown in Figure 2.2. Compared to Figure 2.6b, although the relative adsorption strength has changed slightly, it still has a good similarity as shown in Figure 2.6b. To further compare CO_2 adsorption capability, CO_2-TPD patterns of spent catalysts are also investigated in Figure 2.8. As seen, the CO_2-TPD patterns of spent catalysts can be found to change significantly compared with the patterns of as-prepared catalysts. On the Ni and Co doped metal catalysts, the medium adsorption peak of CO_2 decreases obviously, while the strength of the Mg doped catalyst increases obviously. However, the moderate CO_2 adsorption peak of the Cu-doped catalyst disappears, leaving only the strong CO_2 adsorption peak. Although the moderate adsorption peak of Zn-doped catalysts decreases slightly, it remains at a high level compared to reference catalyst. It indicates that Zn incorporation is more beneficial to improve the adsorption performance of CO_2.

The effects of Zn doping amount on reducibility and adsorption behaviors are also investigated as shown in Figure 2.9. As for $ZnFeO_x$ and $ZnFe_2O_x$ catalysts, the reduction peaks of the two catalysts are not obvious. However, for $ZnFe_4O_x$ catalyst, there is a slight forward peak. This phenomenon may be due to the fact that the amount of Zn addition could affect the interaction between Fe and Zn. To some extent, the incorporation of heteroatomic metals may also help regulate the interactions between atoms. With the decrease of the molar ratio of Zn/ Fe, the peak shape of reduction peak gradually resembles that of iron catalyst as expected (Figure 2.7a). As depicted in Figure 2.9b, although different amounts of Zn doping can affect the reduction degree as well as morphology, the weak adsorption behavior of CO_2 (weakly or moderately bonded CO_2 species) changes slightly. By contrast, the strong adsorption peak changes obviously. Compared with $ZnFe_2O_x$ catalyst, the strong adsorption of the other three catalysts is strengthened.

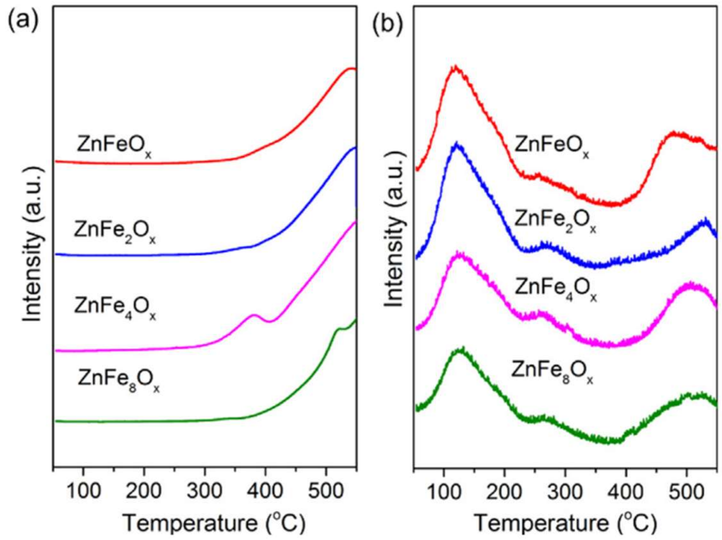

Figure 2.9 (a) H_2-TPR patterns and (b) CO_2-TPD patterns of different Zn-Fe self-combustion catalysts.

2.3.4 Surface composition property of catalyst

Generally, the surface properties of catalysts play a crucial role in understanding catalytic properties. To compare the difference among these spent self-combusted catalysts, XPS measurements are performed as shown in Figure 2.10. After deconvolution of Fe2p spectra, the characteristic peaks at around 708.5 eV, 711.0 eV, and 712.0 eV can be ascribed to Fe-C, Fe^{II}, and Fe^{III}, respectively [4,53]. For C1s spectra (Figure 2.10b), the peaks at 283.6 eV, 284.7 eV, 286.3 eV, and 288.2 eV can be assigned to C-Fe, C-C/C=C, C-O, and C=O, respectively [54–56]. For Fe2p and C1s spectra, Fe-C bond and

C-Fe bond can reflect the interaction between surface iron species and surface carbon species. Actually, there are some changes between the two expressions of interaction between iron species and carbon species (Fe-C bond and C-Fe bond) with the incorporation of another metal.

According to Fe2p spectra, Fe-C bonds appear after reaction, which is important for chain propagation. Compared to Fe-based catalyst, the content of Fe-C bonds increases visually with incorporation of second metal (Figure 2.10a and Table 2.4). To some extent, the utilization of heteroatom is conducive to improve surface carbides content. However, as depicted in Figure 2.10b, although surface content of Fe-C bonds increases, the content of C-Fe bonds varies, perhaps depending to the properties of doped metal. As the chart shows, with the incorporation of Co and Ni metal, the content of C-Fe bonds decreases obviously. Combined with CO_2 adsorption as well as Fe2p XPS spectra (Figure 2.7b and Figure 2.10a), it can be inferred that competitive reactions may occur on the surface of catalyst, weakening the interaction between the adsorbed carbon species and Fe species due to the presence of Ni and Co metals. And these competitive reaction properties should be derived from Co and Ni metal with a high methanation activity [57,58]. By contrast, although the presence of the alkaline Mg metal slightly improves the content of Fe-C bonds, the adsorption behavior of surface carbon species become very weak. It can be seen from this phenomenon that the $NiFe_2O_x$ spinel-like structure is not conducive to the formation of active iron species (Figure 2.4b). With the incorporation of Cu metal, the surface content of Fe-C (Fe2p) and C-Fe (C1s) bonds increases according to Figure 2.10 and Table 2.4. Previously, researchers have also reported that synergistic interactions between Fe and Cu promote catalytic performance [30]. When Zn is adopted as a structural promoter, the surface contents of both are improved. As reaction proceeds, the species of $ZnFe_2O_x$ spinel are gradually transformed into a wide variety of active sites. In addition, improved CO_2 adsorption will further promote this phenomenon (Figure 2.7b). In addition, HR-TEM images are also used to verify the existence of Fe-C bond. According to Figure 2.5, the lattice fringe of carbides can be clearly detected, which is in accordance to XPS results (Figure 2.9).

Meanwhile, the effects of Zn/Fe molar ratio on surface properties of catalysts are also drawn in Figure 2.11. As depicted in Figure 2.11a, the surface content of Fe-C bonds decreases obviously when Zn/Fe molar ratio equals 1. By contrast, with the decrease of Zn/Fe molar ratio, the surface Fe-C bonds content increases visually. This situation is likely due to excessive ZnO covering the active sites of iron species (Figure 2.6b). Because the presence of Zn promotes the adsorption of CO_2 (Figure 2.9b), the surface content of C-Fe bonds in C1s changes little (Table 2.5). It is obvious that Zn as a structural promoter can effectively improve the surface properties of the catalyst, which is crucial for chain propagation to obtain target products.

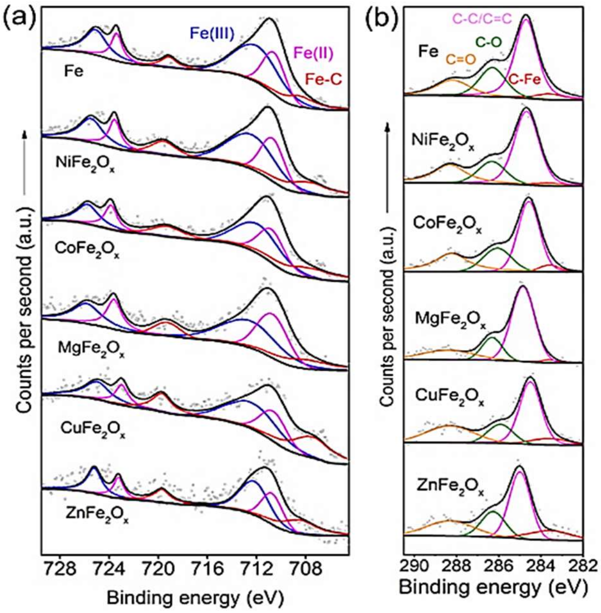

Figure 2.10 (a) Fe2p XPS spectra and the corresponding deconvolution results of spent self-combustion catalysts; (b) C1s XPS spectra and the corresponding results of spent self-combustion catalysts.

Table 2.4. Surface composition of spent doped iron-based catalysts. [a]

Entry	Catalyst	Composition from Fe2p (mol.%)			Composition from C1s (mol.%)			
		$Fe^{(III)}$	$Fe^{(II)}$	Fe-C	C=O	C-O	C-	C-
1	Fe_2O_3	54.3	29.6	16.1	16.9	21.9	54.8	6.4
2	$CoFe_2O_x$	47.4	28.5	24.1	23.6	18.2	55.6	3.4
3	$NiFe_2O_x$	42.0	29.6	28.4	27.4	20.2	48.3	4.1
4	$MgFe_2O_x$	45.5	35.7	18.8	17.8	16.4	63.0	2.8
5	$CuFe_2O_x$	42.1	24.5	33.4	27.9	16.0	49.3	7.8
6	$ZnFe_2O_x$	45.8	26.7	27.5	23.3	19.2	45.0	12.5

[a] Data obtained from XPS measurements.

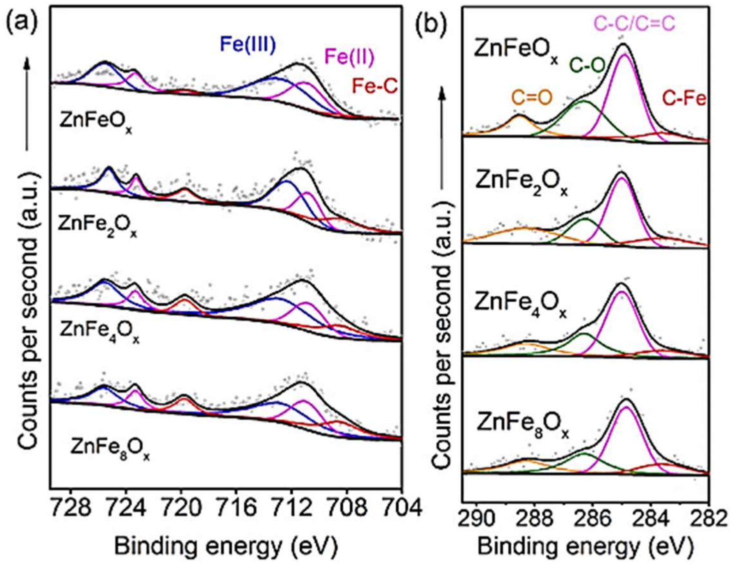

Figure 2.11 (a) Fe2p XPS spectra and the corresponding deconvolution results of spent self-combustion catalysts; (b) C1s XPS spectra and the corresponding results of spent self-combustion catalysts.

Table 2.5 Surface composition of spent doped iron-based catalysts. [a]

Entry	Catalyst	Composition from Fe2p (mol.%)			Composition from C1s (mol.%)			
		Fe $^{(III)}$	Fe $^{(II)}$	Fe-C	C=O	C-O	C-	C-
1	$ZnFeO_x$	55.4	38.1	6.5	14.8	28.0	44.5	12.7
2	$ZnFe_2O_x$	45.8	26.7	27.5	23.3	19.2	45.0	12.5
3	$ZnFe_4O_x$	56.1	24.0	19.9	18.4	25.0	46.5	10.1
4	$ZnFe_8O_x$	45.7	27.5	26.7	18.0	23.1	47.2	11.6

[a] Data obtained from XPS measurements.

2.3.5 Effect of different metals

Catalytic performances of different self-combustion catalysts are performed as shown in Figure 2.12 (Table 2.6 and Figure 2.13). Compared to Fe_2O_3 catalyst, the reaction products obtained from $NiFe_2O_x$ catalyst, are shifted from low hydrocarbons (C_2-C_4, Figure 2.12a) to CH_4 products (80% in whole hydrocarbons, Figure 2.12b). In addition to the slightly weaker methanation ability, the same reaction performance also appears on $CoFe_2O_x$ catalyst (Figure 2.12c). Generally, Ni and Co metals have a benign methanation ability, thus these catalytic performances are mainly due to the characteristics of doped metal [57,58]. As for $MgFe_2O_x$ catalyst (Figure 2.12d), although catalytic products distribution changes little, the incorporation of Mg leads to the increase of olefins hydrogenation ability on the catalyst surface. Previous studies have reported that the addition of appropriate Mg promoter can help inhibit the selectivity of CH_4 and increase the olefins content [59,60]. However, with the large utilization of Mg promoter, $MgFe_2O_x$ does not exhibit the improved performance as we expected. Clearly, it indicates that Mg as an electron promoter exists a suitable additive amount to modify Fe-based catalysts. Compared with the reference catalyst (Fe_2O_3), magnesium can also improve the adsorption of CO_2 (Figure 2.2). However, combined with XRD patterns of spent catalysts (Figure 2.4b), it can be found that the Mg-doped catalyst after the reaction does not expose more active sites than Zn-doped catalysts. Thus, despite its improved CO_2 adsorption, the subsequent chain growth process is not improved and then shows a poor catalytic activity (Table 2.7). By contrast, spinel $CuFe_2O_x$ species as a precursor exhibits improved olefins selectivity than that of Fe_2O_3 catalyst except a low CH_4 selectivity (Figure 2.12e). As discussed above, the incorporation of Cu metal improves the reduction and carbonization of iron species, which is consistent with previous reports [30,31]. In addition, Cu has a benign reactivity without methanation ability, which facilitates the generation of CO intermediates. At the same time, the formed CO intermediates can be converted into hydrocarbons over carbide sites in time. When Zn as a structural promoter is adopted to modify Fe catalyst ($ZnFe_2O_x$), catalytic performance is obviously improved compared to Fe_2O_3 catalyst. In addition to significantly increasing the adsorption of CO_2 on the catalyst surface (Figure 2.7b), Zn promoter can also improve the surface content of carbides (Figure 2.10b and Table 2.4), and then presents a high carbon chain propagation ability. The addition of Zn contributes to the formation of more basic iron carbides in addition to preferably adsorbing and activating CO_2, thus increasing light olefins selectivity [46]. Zn as an efficient promoter can improve the adsorption of reactants and the generation of active sites simultaneously. CO_2-TPD patterns (Figure 2.8) also demonstrate the improved CO_2 adsorption ability. Besides, different from Cu-doped catalyst, the moderate CO_2 adsorption peak remains a high level, which is beneficial for CO_2 conversion. Therefore, Zn-doped catalyst exhibits a high reaction ability than Cu-doped catalyst.

Different from the addition of Zn, although the addition of Co and Ni can significantly promote the adsorption of CO_2, their corresponding catalytic activity has not been significantly enhanced like that of $ZnFe_2O_x$ catalyst. Combined with the XRD patterns of spent catalysts (Figure 2.4b), it can be found that among the catalysts after reaction, the Zn modified catalyst can better expose the active sites, thus presenting a high catalytic activity. According to the Figure 2.10 and Table 2.4, the introduction of both Cu and Zn promotes the formation of active carbides, and the introduction of Cu leads to a higher content of carbides. However, according to the Table 2.4, the introduction of Zn can promote the formation of C-Fe bonds. Combined with Figure 2.7 and Figure 2.9b, it can be visually found that the introduction of Zn can significantly promote the adsorption of CO_2 than that of Cu, consequently obviously increasing activity. In addition, the catalytic performance was also compared with that of other similar catalysts (Table 2.8).

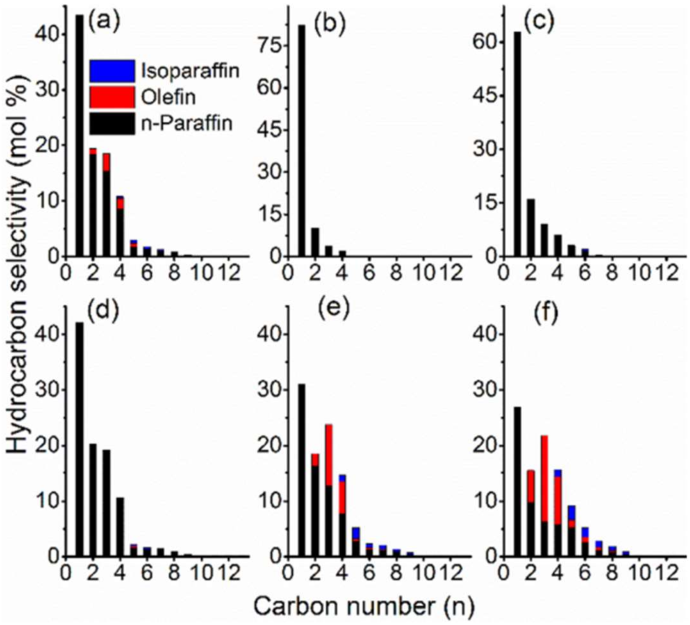

Figure 2.12 Detailed hydrocarbon distribution obtained over different self-combustion catalysts. (a) Fe_2O_3, (b) $NiFe_2O_x$, (c) $CoFe_2O_x$, (d) $MgFe_2O_x$, (e) $CuFe_2O_x$, (f) $ZnFe_2O_x$. Reaction conditions: 300 °C, 1.0 MPa, 10 g h mol^{-1}, TOS = 6 hours.

Table 2.6 CO_2 hydrogenation reaction over different self-combustion catalysts. [a]

Entry	Catalyst	Conv. / %	CO Sel. / %	HC$_x$ Selectivity / %					$C_{2+}^{=}$ Sel. (%)
				CH_4	C_2-C_4^0	C_2-$C_4^=$	C_{5+}^0	$C_{5+}^=$	
1	Fe_2O_3	21.1	13.6	43.5	42.5	6.3	6.6	1.1	7.4
2	$NiFe_2O_x$	27.1	15.3	82.5	16.2	0.1	1.1	0.1	0.2
3	$CoFe_2O_x$	28.6	21.1	62.8	30.9	0.3	5.9	0.1	0.4
4	$MgFe_2O_x$	19.0	28.1	42.1	50.0	0.2	7.1	0.5	0.7
5	$CuFe_2O_x$	28.2	18.5	31.0	37.7	19.1	11.0	1.2	20.3
6	$ZnFe_2O_x$	34.6	17.1	26.9	23.2	29.4	17.1	3.3	32.7

[a] Reaction conditions: 300 °C, 1.0 MPa, 10 g h mol^{-1}, TOS = 6 h.

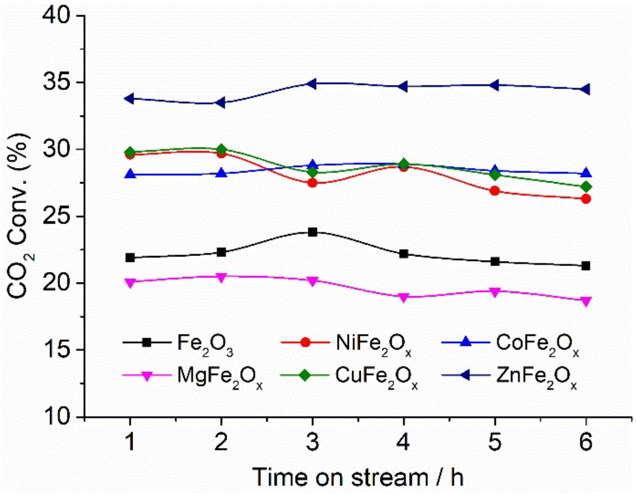

Figure 2.13 Time-on-stream stability curves of CO_2 conversion over different catalyst (1.0 MPa, 10 g h mol^{-1}).

Table 2.7 CO_2 hydrogenation reaction over different self-combustion catalysts. [a]

Entry	Catalyst	Conv. / %	CO Sel.	HCx Selectivity / %					$C_{2+}^{=}$ Sel.
				CH_4	C_2-C_4^0	C_2-$C_4^=$	C_{5+}^0	$C_{5+}^=$	
1	Fe_2O_3	21.1	13.6	43.5	42.5	6.3	6.6	1.1	7.4
2	$ZnFeO_x$	34.7	13.8	34.2	34.6	18.7	9.9	2.5	21.2
3	$ZnFe_2O_x$	34.6	17.1	26.9	23.2	29.4	17.1	3.3	32.7
4	$ZnFe_4O_x$	33.0	15.4	38.8	32.2	19.9	8.2	1.0	20.9
5	$ZnFe_8O_x$	30.7	14.5	40.7	41.2	10.2	7.1	0.7	10.9

[a] Reaction conditions: 300 °C, 1.0 MPa, 10 g h mol^{-1}, TOS = 6 h.

Table 2.8 CO_2 hydrogenation reaction over different catalysts under temperature 300°C.

Ref	Catalyst	GHSV / ml g^{-1} h^{-1}	P / MPa	Conv. / %	CO Sel. / %	HCx Selectivity / %			O/O+P [a]
						CH_4	C_2-C_4	C_{5+}	
[1]	Fe_2O_3	560	2.5	30.8	15.7	35.	45.5	18.	1.3
[1]	15Fe5K/Si	560	2.5	17.4	58.8	8.0	15.8	76.	70
[2]	Fe-Mg-Cu-	1320	1.0	29.0	16.0	26.	73.8[b]	/	29
[3]	Fe-K/Al_2O_3	2000	1.0	35.0	21.0	15.	84.8[c]	/	52
[4]	Fe_2O_3-	1140	1.0	23.0	21.0	17.	82.2[d]	/	58
[5]	Fe/NaY	1900	1.0	20.8	29.5	14.	45.5	39.	71
[6]	$FeCeO_x$	15500	1.0	25.0	22.0	48.	51.2[e]	/	/
[7]	1Fe-1Zn-K	1000	0.5	37.8	11.1	46.	48.3	5.5	84
Our	$ZnFe_2O_x$	2400	1.0	34.6	17.1	26.	52.6	20.	56

[a] The percentage of olefin in the C_{2-4} hydrocarbons

[b] C_{2+} hydrocarbon selectivity

[c] C_{2+} hydrocarbon selectivity

[d] C_{2+} hydrocarbon selectivity

[e] C_{2+} hydrocarbon selectivity

2.3.6 Effect of different Zn/Fe molar ratios

The effects of different Zn/Fe molar ratio on catalytic performances are compared in Figure 2.14 and Table 2.7. Obviously, with the introduction of Zn structural promoter, these catalysts show improved olefin selectivity regardless of the added Zn content. It indicates that Zn, as a good promoter, can effectively promote the generation of olefin via CO_2 hydrogenation. When the Zn/Fe molar content is 1/2, $ZnFe_2O_x$ catalyst shows the best performance including reaction activity and light olefins selectivity. With the further decreases of Zn/Fe molar ratio, the selectivity of olefin decreases, and the selectivity of CH_4 increases gradually. As shown in Figure 2.9b and Figure 2.11, obviously, with the addition of Zn promoter, the adsorption capacity of CO_2 and the content of carbides are improved significantly, which is crucial for improving catalytic performance. The catalytic activity of CO_2 can be effectively enhanced regardless of the additive amount. Although the activity is increased, the product distribution is affected by the additive amount of Zn promoter. It indicates that an appropriate additive amount is of great significance to the promotion of catalytic activity and the improvement of product distribution. Excessive Zn content can lead to the formation of zinc oxide products, and the contact mode between zinc oxide and iron-containing species is worse than that of $ZnFe_2O_x$. However, too little Zn content results in the formation of separated iron oxide species. Therefore, the formation of spinel structure according to the specific composition of Zn and Fe (Zn/Fe = 1/2) is more conducive to the sequence reaction. According to the above discussion, Zn, as an excellent structural promoter, can promote the formation olefin-rich C_{2+} products.

In addition, when zinc-iron forms a spinel structure according to a certain molar ratio (1/2), the metallic iron sites can be better exposed during the reaction, thereby improving the catalytic activity. In particular, the introduction of zinc structural promoter can effectively improve the adsorption behavior of CO_2 regardless of the additive amount, thus the introduction of Zn can be conducive to activity enhancement. In contrast, special spinel-structured catalysts ($ZnFe_2O_x$) exhibit an improved hydrocarbon distribution, which indicates that the interaction between Zn and Fe can affect the reaction process. In addition to the improved adsorption, proper Zn-Fe interaction facilitates olefin selective formation achieved by controlling Zn-Fe molar composition.

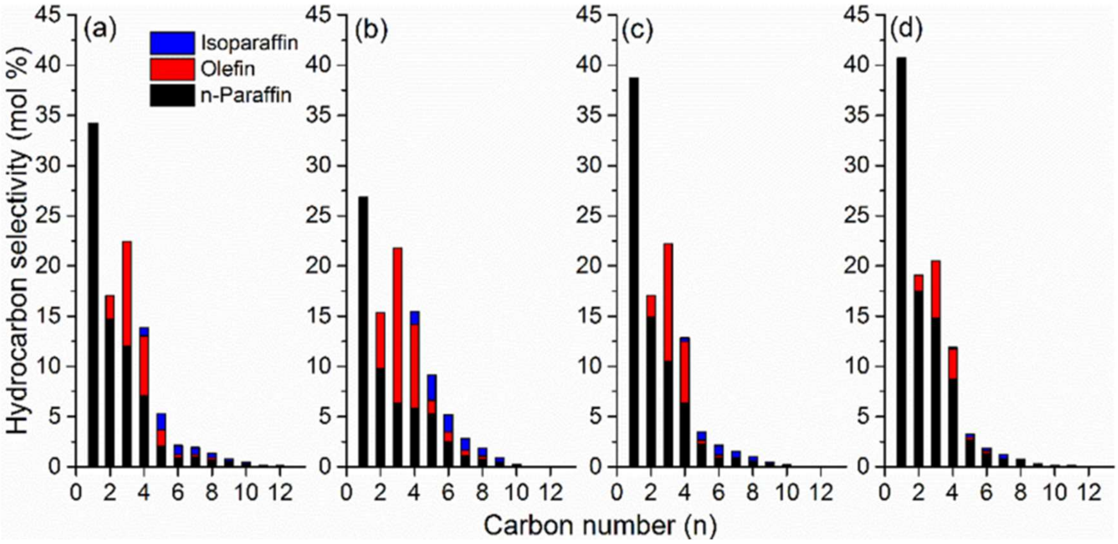

Figure 2.14 Detailed hydrocarbon distribution obtained over different self-combustion catalysts. (a) $ZnFeO_x$, (b) $ZnFe_2O_x$, (c) $ZnFe_4O_x$, (d) $ZnFe_8O_x$. Reaction conditions: 300 °C, 1.0 MPa, 10 g h mol^{-1}, TOS = 6 hours.

2.3.7 Rational design of efficient iron-based catalysts

It is a key to construct and design highly efficient iron-based catalysts for the CO_2 hydrogenation process. One of the key factors is the convenient preparation process and limited operating steps, which reduces the time and process cost of catalyst production. By contrast, spinel-like catalysts can be easily obtained through self-combustion method. Meanwhile, it can be found that $ZnFe_2O_x$ catalyst exhibits a superior catalytic activity (about 35%) compared to current conventional catalysts under mild reaction conditions (Table 2.8). In addition, $ZnFe_2O_x$ also exhibits a lower selectivity (less than 20%) for CO by product, which means that more carbon sources are converted to hydrocarbons products. As shown in Table 2.8, $ZnFe_2O_x$ shows a high chain propagation ability (C_{5+} products) while maintaining a high olefin selectivity (O/(O + P)). More importantly, $ZnFe_2O_x$ catalyst is not modified by any electronic promoters. The high carbon chain growth capability and high reactivity make $ZnFe_2O_x$ catalyst a promising candidate for efficiently catalyzing CO_2 hydrogenation. Therefore, constructing a high-efficiency catalyst through self-combustion method will have good prospects.

2.4 Conclusions

In summary, a serial of spinel-like structure catalysts ($NiFe_2O_x$, $CoFe_2O_x$, $MgFe_2O_x$, $CuFe_2O_x$, and $ZnFe_2O_x$) are successfully fabricated through urea self-combustion method. Compared with reference catalysts (Fe_2O_3), $NiFe_2O_x$ and $CoFe_2O_x$ catalysts show a high CH_4 selectivity. As for $MgFe_2O_x$ catalysts, although product distribution changes little, the olefins hydrogenation ability on catalyst surface becomes stronger than Fe_2O_3 catalysts. However, with the incorporation of Cu promoter, catalytic activity as well as light olefins selectivity are improved owing to the synergistic effect between Cu and Fe species. This synergy can be attributed to improved CO_2 adsorption and surface carbides formation. Among these spinel catalysts, $ZnFe_2O_x$ catalyst exhibits the best catalytic performance with larger light olefins selectivity and chain growth ability. Zn as a structural promoter promotes CO_2 adsorption and more basic iron carbides formation, which is vital for enhancing CO_2 hydrogenation performance. $ZnFe_2O_x$ species from urea self-combustion method, with Zn as an active precursor, provides a benign route for efficiently catalyzing CO_2 hydrogenation to value hydrocarbon products, especially olefin-rich C_{2+} products.

References

[1] G.A. Meehl, W.M. Washington, W.D. Collins, J.M. Arblaster, A. Hu, L.E. Buja, W.G. Strand, H. Teng, Science, 2005, 307, 1769–1772.

[2] M.D. Porosoff, B. Yan, J.G. Chen, Energy Environ Sci. 2016, 9, 62–73.

[3] D. Zeng, D. Cui, Y. Qiu, M. Li, L. Ma, S. Zhang, R. Xiao. Fuel, 2020, 274, 117854.

[4] L. Guo, J. Sun, X. Ji, J. Wei, Z. Wen, R. Yao, H. Xu, Q. Ge, Commun Chem., 2018, 1, 11.

[5] Y. Ni, Z. Chen, Y. Fu, Y. Liu, W. Zhu, Z. Liu, Nat Commun., 2018, 9, 3457.

[6] X. Liu, M. Wang, C. Zhou, W. Zhou, K. Cheng, J. Kang, Q. Zhang, W. Deng, Y. Wang, Chem Commun., 2018, 54, 140–143.

[7] J. Wei, Q. Ge, R. Yao, Z. Wen, C. Fang, L. Guo, H. Xu, J. Sun, Nat Commun., 2017, 8, 15174.

[8] P. Gao, S. Li, X. Bu, S. Dang, Z. Liu, H. Wang, L. Zhong, M. Qiu, C. Yang, J. Cai, W. Wei, Y. Sun, Nat Chem., 2017, 9, 1019–1024.

[9] Y. Wang, L. Tan, M. Tan, P. Zhang, Y. Fang, Y. Yoneyama, G. Yang, N, Tsubaki, ACS Catal., 2019 , 9, 895–901.

[10] J. Zhang, M. Zhang, S. Chen, X. Wang, Z. Zhou, Y. Wu, T. Zhang, G. Yang, Y. Han, Y. Tan, Chem Comm., 2019, 55, 973–976.

[11] L. Tan, P. Zhang, Y. Cui, Y. Suzuki, H. Li, L. Guo, G. Yang, N. Tsubaki, Fuel Process Technol., 2019, 196, 106174

[12] D. Previtali, M. Longhi, F. Galli, A.D. Michele, F. Manenti, M. Signoretto, F. Menegazzo, C. Pirola, Fuel, 2020, 274, 117804.

[13] S.I. Ngo, Y-I. Lim, D. Lee, K.S. Go, M.W. Seo, Fuel, 2020, 275, 117886.

[14] T. Chwoła, T. Spietz, L. Więcław-Solny, A. Tatarczuk, A. Krótki, S. Dobras, A. Wilk, J. Tchorz, M. Stec, J. Zdeb, Fuel, 2020, 263, 116804.

[15] L. Zhang, F. Wang, J. Zhu, B. Han, W. Fan, L. Zhao, W. Cai, Z. Li, L. Xu, H. Yu, W.

Shi, Fuel, 2019, 256, 115954.

[16] S. Xiong, Y. Lian, H. Xie, B. Liu, Fuel, 2019, 256, 115975.

[17] J. Chen, X. Wang, D. Wu, J. Zhang, Q. Ma, X. Gao, X. Lai, H. Xia, S. Fan, T-S. Zhao, Fuel, 2019, 239, 44–52.

[18] C. Bassano, P. Deiana, L. Lietti, C.G. Visconti, Fuel, 2019, 253, 1071–1079.

[19] S. Falcinelli, A. Capriccioli, F. Pirani, F. Vecchiocattivi, S. Stranges, C. Martì, A. Nicoziani, E. Topini, A. Lagana, Fuel, 2017, 209, 802–811.

[20] S. Abelló, C. Berrueco, D. Montané, Fuel, 2013, 113, 598–609.

[21] L. Guo, J. Sun, Q. Ge, N. Tsubaki, J Mater Chem A. 2018, 6, 23244–23262.

[22] B. Liang, H. Duan, T. Sun, J. Ma, X. Liu, J. Xu, X. Su, Y. Huang, T. Zhang, ACS Sustainable Chem Eng., 2018, 7, 925–932.

[23] F. Jiang, B. Liu, S. Geng, Y. Xu, X. Liu, Catal Sci Technol., 2018, 8, 4097–4107.

[24] C.G. Visconti, M. Martinelli, L. Falbo, A. Infantes-Molina, L. Lietti, P. Forzatti, G. Iaquaniello, E. Palo, B. Picutti, F. Brignoli, Appl Catal B-Environ., 2017, 200, 530–542.

[25] W. Li, A. Zhang, X. Jiang, M.J. Janik, J. Qiu, Z. Liu, X. Guo. C. Song, J CO_2 Util., 2018, 23, 219–225.

[26] T. Numpilai, T. Witoon, N. Chanlek, W. Limphirat, G. Bonura, M. Chareonpanich, J. Limtrakul, Appl Catal A-Gen., 2017, 547, 219–229.

[27] M.K. Gnanamani, G. Jacobs, H.H. Hamdeh, W.D. Shafer, F. Liu, S.D. Hopps, G.A. Thomas, B.H. Davis, ACS Catal., 2016, 6, 913–927.

[28] C. Yang, B. Zhao, R. Gao, S. Yao, P. Zhai, S. Li, J. Yu, Y. Hou, D. Ma, ACS Catal., 2017, 7, 5661–5667.

[29] G. Centi, S. Perathoner, Catal Today, 2009, 148, 191–205.

[30] W. Wang, X. Jiang, X. Wang, C. Song, Ind Eng Chem Res., 2018, 57, 4535–4542.

[31] J. Liu, A. Zhang, X. Jiang, M. Liu, Y. Sun, C. Song, X. Guo, ACS Sustainable Chem Eng., 2018, 6, 10182–10190.

[32] X. Nie, H. Wang, M.J. Janik, Y. Chen, X. Guo, C. Song, J Phys Chem C., 2017, 121, 13164–13174.

[33] X. Nie, H. Wang, M.J. Janik, X. Guo, C. Song, J Phys Chem C., 2016, 120, 9364–9373.

[34] Y.H. Choi, Y.J. Jang, H. Park, W.Y. Kim, Y.H. Lee, S.H. Choi, J.S. Lee, Appl Catal B-Environ., 2017, 202, 605–610.

[35] C. Vogt, E. Groeneveld, G. Kamsma, M. Nachtegaal, L. Lu, C.J. Kiely, P.H. Berben, F. Meirer, B.M. Weckhuysen, Nat Catal., 2018, 1, 127–134.

[36] L.R. Winter, E. Gomez, B. Yan, S. Yao, J.G. Chen, Appl Catal B-Environ., 2018, 224, 442–450.

[37] F. Studt, I. Sharafutdinov, F. Abild-Pedersen, C.F. Elkjær, J.S. Hummelshøj, S. Dahl, I. Chorkendorff, J.K. Nørskov, Nat Chem., 2014, 6, 320–324.

[38] T. Ishihara, K. Eguchi, H. Arai, Appl Catal., 1987, 30, 225–238.

[39] T. Li, H. Wang, Y. Yang, H. Xiang, Y. Li, Fuel Process Technol., 2014, 118, 117–124.

[40] K. Zhao, W. Wang, Z. Li, J CO_2 Util., 2016, 16, 236–244.

[41] M. Luo, B.H. Davis, Appl Catal A-Gen., 2003, 246, 171–181.

[42] A. Nakhaei Pour, S.M.K Shahri, H.R. Bozorgzadeh, Y. Zamani, A.Tavasoli, M.A. Marvast, Appl Catal A-Gen., 2008, 348, 201–208.

[43] D. Mattia, M.D. Jones, J.P. O'Byrne, O.G. Griffiths, R.E. Owen, E. Sackville, M. McManus, P. Plucinski, ChemSusChem., 2015, 8, 4064–4072.

[44] G. Kishan, M-W. Lee, S-S. Nam, M-J. Choi, K-W. Lee, Catal Lett., 1998, 56, 215–219.

[45] P. Zhai, C. Xu, R. Gao, X. Liu, M. Li, W. Li, X. Fu, C. Jia, J. Xie, M. Zhao, X. Wang, Y-W. Li, Q. Zhang, X-D. Wen, D. Ma, Angew Chem Int Ed., 2016, 128, 10056–10061.

[46] P.S.S. Prasad, J.W. Bae, K-W. Jun, K-W. Lee, Catal Surv Asia., 2008, 12, 170–183.

[47] J. Zhang, S. Lu, X. Su, S. Fan, Q. Ma, T. Zhao, J CO_2 Util., 2015, 12, 95–100.

[48] S-L. Soled, E. Iglesia, S. Miseo, B-A. DeRites, R-A. Fiato, Top Catal., 1995, 2, 193–205.

[49] S-L, Gonzalez-Cortesa, T-C. Xiao, M.L.H. Green, Stud Surf Sci Catal., 2006, 162, 817–824.

[50] N.F.P. Ribeiro, R.C.R. Neto, S.F. Moya, M.M.V.M. Souza, M. Schmal, Int J Hydrogen Energy, 2010, 35, 11725–11732.

[51] L. Guo, P. Zhang, Y. Cui, G. Liu, J. Wu, G. Yang, Y. Yoneyama, N. Tsubaki, ACS Sustainable Chem Eng., 2019, 7, 8331–8339.

[52] L. Guo, Y. Cui, P. Zhang, X. Peng, Y. Yoneyama, G. Yang, N. Tsubaki, ChemistrySelect., 2018, 3, 13705–13711.

[53] BL. Liang, T. Sun, JG. Ma, HM. Duan, L. Li, XL. Yang, YR. Zhang, X. Su, YQ. Huang, T. Zhang, Catal Sci Technol., 2019, 9, 456–464.

[54] C. Nie, H. Zhang, H. Ma, W. Qian, Q. Sun, WY. Ying, Catal Lett., 2019, 149, 1375–1382.

[55] S. Jang, S-W. Kang, D-H. Chun, H-T. Lee, J-I. Yang, H. Jung, H-D. Jeong, K-M. Nam, J-C. Park, New J Chem., 2017, 41, 2756–2763.

[56] B. Sun, Z. Jiang, D. Fang, K. Xu, Y. Pei, S. Yan, MH. Qiao, KN. Fan, BN. Zong, ChemCatChem., 2013, 5, 714–719.

[57] G. Zhou, H. Liu, K. Cui, A. Jia, G. Hu, Z. Jiao, Y. Liu, X. Zhang, Appl Surf Sci., 2016, 383, 248–252.

[58] C.G. Visconti, M. Martinelli, L. Falbo, L. Fratalocchi, L. Lietti. Catal Today., 2016, 277, 161–170.

[59] J. Yang, Y. Sun, Y. Tang, Y. Liu, H. Wang, L. Tian, H. Wang, Z. Zhang, H. Xiang, Y. Li, J Mol Catal A., 2006, 245, 26–36.

[60] Q. Zhang, J. Kang, Y. Wang, ChemCatChem., 2010, 2, 1030–1058.

Chapter 3

Fabrication of CuZn-Based Catalyst via Polyethylene Glycol surfactant and supercritical drying

Schematic diagram for preparation of CuZn-SC-Px catalysts by urea co-precipitation method with PEG treatment and supercritical CO_2 drying.

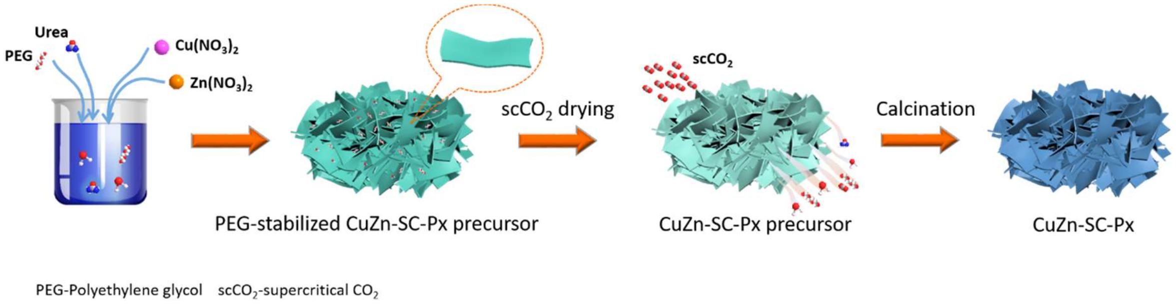

Abstract

CuZn-based catalysts have been applied in industrial methanol synthesis. However, in alcohol-assisted low-temperature methanol synthesis (LT-MS), preparation of highly efficient CuZn-based catalysts is still a considerable challenge. Here, we report two optimized strategies that use polyethylene glycol (PEG) surfactant and supercritical CO_2 drying in urea co-precipitation method, to synthesize the highly efficient CuZn-based catalysts. The PEG treatment is utilized to enhance porosity and improve surface functional groups of the CuZn-based catalysts, and the supercritical CO_2 drying is employed to increase reduction degree for them. The catalytic results of alcohol-assisted LT-MS reveal that via the two optimized strategies, a CuZn-SC-P5 catalyst exhibits superior catalytic performance. It is significantly different from the CuZn-based catalysts prepared by traditional impregnation method, and also better than the catalysts treated by sole PEG treatment or supercritical CO_2 drying. The present work provides multiple strategies to improve catalytic efficiency, and will be beneficial to explore new approaches in catalyst synthesis.

3.1 Introduction

Methanol is a key commodity for chemical industries. In last century, the ICI Co. Ltd. developed a widespread method that employed Cu/ZnO/Al_2O_3 catalysts to produce methanol from syngas (CO/H_2)[1-4]. However, high temperature (250 to 300 °C) and high pressure (5.0 to 10.0 MPa) are utilized in this synthesis method. The high temperatures result in thermodynamic limitation for the CO conversion, because methanol synthesis is a strongly exothermic reaction ($CO + 2H_2 = CH_3OH$, ΔH_{298K} = -90.8 KJ mol-1) [5,6]. The equilibrium conversion of CO is only around 25 % at 300 °C and 50 atm. It is highly desirable to develop low-temperature methanol synthesis (LT-MS). Although several research groups have focused on the LT-MS process (100 to 180 °C), harsh operating conditions prevented them from large-scale industrial applications [7-9].

The Brookhaven National Laboratory (BNL) of USA reported a LT-MS in slurry at 100-130 °C and 1.0-5.0 MPa over a strong base catalyst composed of NaH, alcohol and acetate [8]. However, trace amounts of water (H_2O) or carbon dioxide (CO_2) in the LT-MS systems can rapidly deactivate the basic catalyst. Another method via methylformate (MF) in liquid phase at 100 °C for LT-MS was first proposed by Christiansen [9]. The mechanism of this process consists of methanol carbonylation to methyl formate, and hydrogenolysis of the methyl formate to methanol. Wender and co-workers further developed this method via a Cu-Cr/CH_3OK catalyst at a 140-180 °C with 3.8-6.2 MPa. They realized high CO conversion and methanol synthesis rate[10,11]. However, the deactivation of the alkoxide catalyst has never been solved. To overcome this problem, we have designed alcohol-assisted LT-MS in our previous works, which claimed that the alcohols in the LT-MS remarkably lowered the reaction temperature[12-18]. But, to date, exploration of highly efficient catalyst is still highly challenging in the alcohol-assisted LT-MS.

CuZn-based catalysts have been widely used in methanol synthesis from syngas (CO/H_2) or CO_2 hydrogenation [19-22]. They are usually synthesized using co-precipitation method. In the traditional co-precipitation, routine precipitant (for example, Na_2CO_3, NaOH) is employed to prepare CuO/ZnO precursor. The CuO/ZnO precursor is then dried in air at a temperature above 100 °C. However, the routine co-precipitation process results in a weak porous structure and few surface functional groups for CuZn-based catalyst. The traditional drying process in air at the high temperature further reduces porosity and the number of active sites. The obtained CuZn-based catalysts significantly decrease performance of methanol synthesis. Therefore, it is necessary to alter the traditional co-precipitation method with novel precipitation process and efficient drying technique.

Herein, we present two improvement strategies on the traditional co-precipitation method for CuZn-based catalysts. Polyethylene glycol (PEG) as a surfactant is utilized in the precipitation process, to enhance porosity and increase surface functional groups for the CuZn-based catalysts [23,24]. Supercritical CO_2 drying is employed in the drying process to improve the number of active sites for them[25,26]. We also synthesize the CuZn-based catalysts using traditional precipitation process, drying technique, or impregnation method, to compare the catalysts from the two improvement strategies. The physical and chemical properties of these CuZn-based catalysts are systematically investigated by multiple characterization techniques. Further, we evaluate these CuZn-based catalysts in alcohol-assisted LT-MS, and the catalysts optimized by the two improvement strategies exhibit superior performance at a low temperature of 170 °C.

3.2 Experimental section

3.2.1 Catalyst preparation

The CuZn-based catalysts were synthesized via a homogeneous urea co-precipitation method. Typically, $Cu(NO_3)_2 \cdot 3H_2O$ (0.025 mol L^{-1}), $Zn(NO_3)_2 \cdot 6H_2O$ (0.025 mol L^{-1}) and deionized water (1480 mL) were added into a beaker, to prepare an aqueous solution. PEG (0.05 mol L^{-1}) and urea (0.5 mol L^{-1}) were then introduced into the aqueous solution. The mixed solution was stirred and heated on 95 °C for 2 hours, to obtain the precipitated precursor. After aging for 24 hours at room temperature, the precursor was filtered and washed with deionized water. The solid product was then dried with supercritical CO_2 at a temperature of 35 °C with pressure of 7.5 MPa for 6 hours. After the supercritical CO_2 drying, the obtained sample was calcined in air at 350 °C for 1 hours, and the resulting catalyst was denoted as CuZn-SC-P3. By using the PEG concentration of 0.08 and 0.13 mol L^{-1}, CuZn-SC-P5 and CuZn-SC-P8 were fabricated, respectively, while the other treatment processes were the same as CuZn-SC-P3. CuZn-SC-P0 was also prepared by the same processes, but without the PEG treatment. The series of CuZn-SC-P0, CuZn-SC-P3, CuZn-SC-P5 and CuZn-SC-P8 catalysts were denoted as CuZn-SC-Px (x = 0, 3, 5, 8).

To synthesize traditional CuZn-based catalysts for comparison, we also employed conventional drying method to substitute the supercritical drying process. The solid products were dried in air at 120 °C for 12 hours, after they was filtered and washed with deionized water. The other treatment processes remained unchanged. Using the traditional drying method, CuZn-P0, CuZn-P5 and CuZn-P8 were obtained by tuning the PEG concentration of 0, 0.08 and 0.13 mol/L, respectively. The series of CuZn-P0, CuZn-P5 and CuZn-P8 catalysts were denoted as CuZn-Px (x = 0, 5, 8). In addition, traditional impregnation method were utilized to synthesize two samples of CuZn-I-SC and CuZn-I. In brief, $Cu(NO_3)_2\cdot 3H_2O$ (8.2 g), ZnO powder (5.0 g) and deionized water (5.0 mL) were added into a beaker. The mixture was stirred for 1 hour. The deionized water was then removed at 60 °C. The CuZn-I-SC sample was dried with supercritical CO_2. The CuZn-I sample was dried in air at 120 °C for 12 hours. After the drying process, the two samples were calcined in air at 350 °C for 1 hour. To further compare the influence of urea precipitant, the traditional co-precipitation method, using Na_2CO_3 as precipitant, was also employed to synthesize CuZn-Na catalysts. The molar ratio of Cu/Zn was the same as the other CuZn-Based catalysts. In the preparation, the nitrates of Cu and Zn, were firstly dissolved in deionized water. The aqueous solution of Na_2CO_3 (0.05 mol L^{-1}) was added dropwise to the nitrate solution, under constant stirring at 75 °C for 1 hour. Then, the pH value was kept at 8.0, and the precipitates were aged for 24 hours at room temperature. The final samples were obtained by filtration, washing with deionized water, drying at 120 °C, and calcination in air at 350 °C for 1 hour.

Before alcohol-assisted LT-MS, all the samples were reduced by a gas mixture of H_2/Ar (5 vol.% H_2) at 220 °C for 10 hours with a flow rate of 60 mL min^{-1}. The apparatus with a quartz reactor (inner diameter = 15 mm) for the reduced process. After the reduction, the samples were cooled to room temperature, and then passivated in O_2/N_2 (1 vol.% O_2) atmosphere for 4 hours with a flow rate of 30 mL min^{-1}.

3.2.2 Catalyst characterization

A scanning electron microscope (SEM, JEOL JSM-6360LV) was used to analyze surface morphology of the CuZn-based catalysts. The transmission electron microscope (TEM, JEOL JEM-3200Fs) was employed to observe the high-magnification morphology at an acceleration voltage of 200 kV. The X-ray diffraction (XRD) analyses were performed by an X-ray diffractometer (RINT 2400; Rigaku) with Cu Kα radiation (40 kV and 20 mA). The mean size of Cu and ZnO was calculated by the Scherrer equation at $2\theta = 43.3°$ and $36.1°$, respectively. The elemental composition of the CuZn-based catalysts was determined by X-ray fluorescence (XRF) analysis. The X-ray photoelectron spectroscopy (XPS) analyses were conducted by a Thermo Fisher Scientific ESCALAB 250Xi instrument with an Al Ka X-ray radiation source and a chamber for in situ H_2 reduction pretreatment. The nitrogen physisorption was measured by a NOVA2200e analyzer. Before the physisorption analysis, the sample was degassed at 200 °C for 3 h. The specific surface area and average pore size were calculated based on the method of Brunauer-Emmett-Teller (BET) and Barrett-Joyner-Halenda (BJH) methods.

The H_2 temperature programmed reduction (H_2-TPR) was carried out using a BELCAT-B-TT analyzer (BEL Japan Co. Ltd.) with a thermal conductivity detector (TCD). The sample (50 mg) was pretreated at 150 °C by a helium gas (30 mL min^{-1}) for 1 h. After the pretreatment, the sample was cooled down to 50 °C. Then, a gas mixture of H_2/Ar (5 vol% H_2; 30 mL min^{-1}) was introduced into the test system. The H_2-TPR profiles were recorded from 50 °C to 900°C with a rate of 10 °C/min. The specific Cu^0 surface area and Cu dispersion were determined by N_2O adsorption method. The N_2O adsorption analysis was also conducted on the BELCAT-B-TT analyzer (BEL Japan Co. Ltd.). The sample (50 mg) was also pretreated in a helium gas (30 mL min^{-1}) at 150 °C for 1 h, and then reduced by a H_2/Ar gas (5 vol.% H_2; 30 mL min^{-1}) at 220 °C for 2 h. After the sample was cooled down to 60 °C, pulses of N_2O/He gas (10 vol.% N_2O) was introduced into the system, and the total consumption of N_2O was recorded. The CO temperature programmed desorption (CO-TPD) was studied using the same BELCAT-B-TT analyzer. The helium pretreatment and H_2 reduction were also the same as those of the N_2O adsorption analysis. After the temperature was lowered to 50 °C, a gas mixture of CO/Ar (5 vol.% CO; 30 mL min^{-1}) was introduced into the system. Then the sample was purged by the helium gas (30 mL min^{-1}), and the CO-TPD profile was recorded from 50 °C to 900°C with a rate of 10 °C min^{-1}.

The *in-situ* diffuse reflectance infrared Fourier transform spectroscopy (*in-situ* DRIFT) was carried out on a Thermo Nicolet (NEXUS-470) FTIR spectrometer, equipped with a high-temperature and high-pressure chamber, and a MCT detector. Typically, the sample (10 mg) was loaded into the sample cell, and pretreated by a helium gas (20 mL/min) at 150 ºC. The pretreated sample was further reduced using a H_2/Ar gas (5 vol.% H_2; 20 mL min^{-1}) at 240 ºC for 4 h. After the reduction, the sample was purged by the helium gas, and the background spectra were collected at the different temperatures. Then, CO gas or syngas was introduced into the sample cell, and the *in-situ* DRIFT was recorded at 4 cm^{-1} resolution with 32 scans.

3.2.3 Catalyst evaluation

The catalytic tests were performed by a flow-type semi-batch autoclave reactor (inner volume = 85 ml). The sample (3.0 g) and 2-butanol (40 ml) were added into the reactor simultaneously. 2-butanol was used as solvent, and also acted as catalytic promoter in the system. Then, syngas ($H_2/CO/CO_2/Ar = 62.6/29.5/4.9/3.0$) with a flow rate of 20 mL min^{-1} was introduced into the reactor. After purging the system for 20 minutes with syngas, the reaction was then carried out at a temperature of 170 °C and pressure of 5.0 MPa for 20 hours with continuous stirring. The effluent gas was analyzed using an online gas chromatograph (Shimadzu, GC-8A) with a thermal conductivity detector (TCD). The liquid products both in the reactor and ice trap were analyzed by an off-line GC (Shimadzu, GC-14B) with a flame ionization detector (FID). The conversions of CO, CO_2 and total carbon, and the product selectivity were calculated as follows:

$$\textbf{(1)}\ \text{CO Conv. (\%)} = (CO_{in}/Ar_{in} - CO_{out}/Ar_{out}) / (CO_{in}/Ar_{in}) \times 100$$

CO Conv. – CO conversion; CO_{in} – peak area of CO in feed gas; Ar_{in} – peak area of Ar in feed gas; CO_{out} – peak area of CO in effluent gas; Ar_{out} – peak area of Ar in effluent gas.

$$\textbf{(2)}\ CO_2\ \text{Conv. (\%)} = (CO_{2,in}/Ar_{in} - CO_{2,out}/Ar_{out}) / (CO_{2,in}/Ar_{in}) \times 100$$

CO_2 Conv. – CO_2 conversion; $CO_{2,in}$ – peak area of CO_2 in feed gas; Ar_{in} – peak area of Ar in feed gas; $CO_{2,out}$ – peak area of CO_2 in effluent gas; Ar_{out} – peak area of Ar in effluent gas.

$$\textbf{(3)}\ \text{Total Carbon Conv. (\%)} = \text{CO Conv.} \times a/(a + b) + CO_2\ \text{Conv.} \times b/(a + b)$$

a – CO content in the feed gas; b – CO_2 content in the feed gas.

$$\textbf{(4)}\ S_i\ (\%) = A_i f_i / \Sigma A_i f_i \times 100$$

S_i – selectivity of product i; A_i – peak area for product i; f_i – correction factor from quantitative product i.

$$\textbf{(5)}\ \text{TOF}\ (h^{-1}) = (X_{total} \times n_{total}) / (W_{cat.} \times f_{cu} \times d_{cu} / M_{cu})$$

TOF – turnover frequency; X_{total} – total carbon conversion (%); n_{total} – total carbon number of feed gas per hour (mol/h); $W_{cat.}$ – catalyst weight (g); f_{cu} – weight fraction of Cu in the catalyst (%); d_{cu} – dispersion degree of Cu in the catalyst based on N_2O chemisorption (%); M_{cu} – molar mass of Cu (63.5 g mol^{-1}).

$$\textbf{(6)}\ \text{STY}\ (g\ kg^{-1}\ h^{-1}) = (X_{CO} \times n_{CO} \times S_{MeOH} \times M_{MeOH} / W_{cat.}) + (X_{CO2} \times n_{CO2} \times S_{MeOH} \times M_{MeOH} / W_{cat.})$$

STY – space-time yield (g kg^{-1} h^{-1}); X_{CO} – CO conversion; n_{CO} – CO number of feed gas per hour (mol/h); S_{MeOH} – selectivity of methanol; M_{MeOH} – molar mass of methanol (32.0 g/mol); $W_{cat.}$ – catalyst weight (kg); X_{CO2} – CO_2 conversion; n_{CO2} – CO_2 number of feed gas per hour (mol h^{-1}).

3.3 Results and discussion

3.3.1 CuZn-SC-Px for alcohol-assisted LT-MS

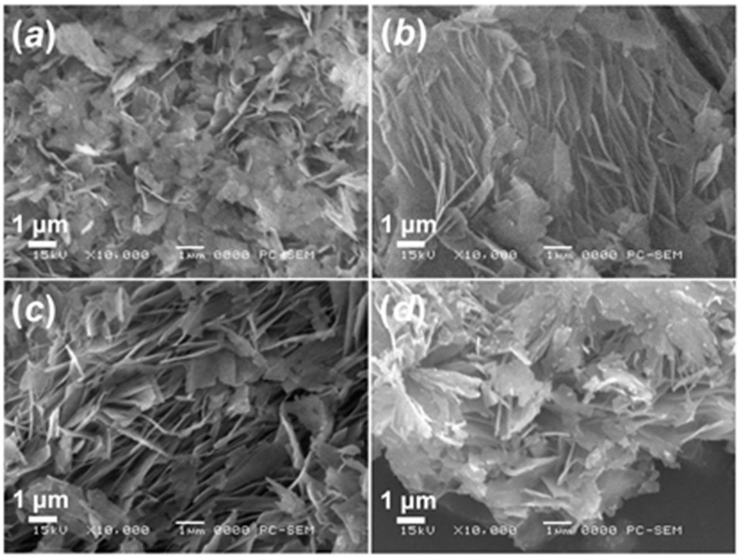

Figure 3.1 SEM analyses for the CuZn-SC-Px catalysts after the calcination. (a) CuZn-SC-P0, (b) CuZn-SC-P3, (c) CuZn-SC-P5 and (d) CuZn-SC-P8

To observe the surface morphology of CuZn-SC-Px catalysts after the calcination, we employed a scanning electron microscope (SEM). The results were shown in Figure 3.1. The CuZn-SC-P0, synthesized from supercritical CO_2 drying without PEG treatment, formed highly disordered sheet structure (Figure 3.1a). CuZn-SC-P3 and CuZn-SC-P5 displayed more uniform sheets than CuZn-SC-P0 (Figure 3.1b, c). Moreover, the sheet thicknesses of CuZn-SC-P5 were broader than those of CuZn-SC-P3. We further counted the thickness of 120 sheets on CuZn-SC-P5. The average sheet thickness was about 78 nm (Figure 3.2). CuZn-SC-P8 also displayed a sheet structure (Figure 3.1d). But the sheet surface of CuZn-SC-P8 generated a large number of bulges, probably due to excessive agglomeration of CuO or ZnO. Compared to the CuZn-SC-P8, CuZn-SC-P5 possessed a more uniform and smooth sheet surface.

We utilized transmission electron microscopy (TEM) to further observe the sheet structure on the calcined CuZn-SC-P5 (Figure 3.3). The TEM results clearly uncovered that a large number of mesopores were formed in the sheet (Figure 3.3a), and average size of the metal oxide nanoparticles was about 10 nm (Figure 3.4). Moreover, the high-magnification TEM image demonstrated that the nanoparticles of CuO and ZnO were linked to each other (Figure 3.3b), and abundant Cu-Zn interfaces were generated in the sheet. The interplanar spacing of 0.23 and 0.28 nm should be attributed to the planes of CuO (111) and ZnO (100), respectively (Figure 3.3b) [27-30]. We also applied energy - diffusive X-ray spectroscopy (EDS) to analyze the sheet (Figure 3.3c-f). The results revealed that the elements of Cu, Zn, and O were uniform in the whole sheet structure.

The element contents of Cu, Zn and O for all the calcined CuZn-SC-Px catalysts were analyzed by X-ray fluorescence (XRF). As shown in Table 3.1, the results uncovered that they were almost the same for each CuZn-SC-Px catalyst. To further explore the physical properties, we employed N_2 adsorption-desorption to analyze the calcined CuZn-SC-Px catalysts. The Brunauer-Emmett-Teller (BET) area and average pore size are also presented in Table 3.1. The CuZn-SC-Px catalysts possessed a BET area from 70.7 to 88.5 m^2/g, and an average pore size from 7.5 to 9.2 nm. The N_2 adsorption-desorption isotherms of CuZn-SC-Px displayed that the CuZn-SC-P3, CuZn- SC-P5 and CuZn-SC-P8 generated higher BET surface area and volume of adsorbed/desorbed N_2 than CuZn-SC-P0 (Table 3.1 and Figure 3.5). This suggests that the PEG treatment improved the porous structures on the CuZn-SC-Px. The pore size distribution of the CuZn-SC-Px exhibited that the CuZn-SC-P3 and CuZn-SC-P5 produced larger mesopore size than the CuZn-SC-P0 and CuZn-SC-P8 (Table 3.1 and Figure 3.6). This further indicates that the PEG treatment was beneficial to stabilize the mesoporous structures. But the mesopore size was decreased, when the PEG dosage was too high in the treatment. As a result, the CuZn-SC-P5 obtained high porosity after the two improvement strategies with the PEG dosage of 5 wt%.

The surface chemical states of CuZn-SC-Px catalysts after calcination at 350 °C were analyzed using X-ray photoelectron spectroscopy (XPS). The Cu 2p region of CuZn-SC-Px catalysts is indicated in Figure 3.7a. The similar Cu 2p peaks imply the same chemical states of Cu species on CuZn-SC-Px. The Cu 2p 3/2 peaks at 933.4 eV, with the satellite characteristic peaks at around 942.0 eV, clearly demonstrated that the Cu species were divalent cations.[31,32] In Figure 3.7b, the Zn 2p region of Zn-SC-Px is shown. The Zn 2p 3/2 peaks at 1021.8 eV were due to ZnO phase, and the shoulder peaks at 1023.7 eV should be attributed to $Zn(OH)_2$ species.[33,34] The shoulder peaks of CuZn-SC-P3 and CuZn-SC-P5 were higher than the CuZn-SC-P0 and CuZn-SC-P8, suggesting that the PEG treatment with moderate dosages can result in high distribution of $Zn(OH)_2$ species. The O 1s region of CuZn-SC-Px was shown in Figure 3.7c. The O 1s peaks at 529.4 and 531.4 eV were mainly due to lattice oxygen and surface chemisorbed oxygen, respectively.[35,36] The increase of the O 1s peaks at 531.4 eV revealed that the high PEG dosage enhanced the content of surface chemisorbed oxygen.

H_2 temperature programmed reduction (H_2-TPR) profiles of the calcined CuZn-SC-Px catalysts are presented in Figure 3.8. They mainly exhibited two peaks in the H_2-TPR profiles. To our knowledge, the peak at low temperature should be ascribed to reduction of highly dispersed Cu species, and the peak at high temperature should be attributed to reduction of bulky CuO particles.[37-39] As shown in Figure 3.9, we also proved this viewpoint via our H_2-TPR analyses of CuZn-based catalysts with different Cu contents. Based on the peak area in Figure 3.8, the reduction degrees could reach 70-75% for these CuZn-SC-Px catalysts, when the reduction temperature was 220 °C (Table 3.2). In addition, the CuZn-SC-P3 CuZn-SC-P5 and CuZn-SC-P8 displayed higher reduction degrees than the CuZn-SC-P0. This observation demonstrated that the PEG treatment enhanced the reduction of the Cu species on the CuZn-SC-Px catalysts.

The X-ray diffraction (XRD) patterns of reduced CuZn-SC-Px are shown in Figure 3.10. The three main peaks at 31.7°, 34.4° and 36.1° should be assigned to the planes of (100), (002) and (101) of ZnO phase, respectively.[40,41] Another main peak at 43.3° should be due to the (111) plane of Cu phase.[42,43] We did not observe significant differences for each CuZn-SC-Px from the XRD analyses. The particle sizes of Cu and ZnO were calculated using the Scherrer equation at $2\theta = 43.3°$ and 36.1°. The calculation results, as indicated in Table 3.1, revealed that the particle sizes of Cu or ZnO were very close on CuZn-SC-Px, although they were prepared by different PEG contents in the co-precipitation process. In contrast, our N_2O chemisorption analysis showed significant differences on the Cu^0 surface area of reduced CuZn-SC-Px (Table 3.1). CuZn-SC-P3, CuZn-SC-P5 and CuZn-SC-P8 generated higher Cu^0 surface areas than CuZn-SC-P0. Moreover, among them CuZn-SC-P5 possessed the highest Cu^0 surface area. This indicates that the PEG treatment is also beneficial for improving the Cu^0 surface area.

To explore the behavior of CO adsorption and activation for the reduced CuZn-SC-Px catalysts, CO temperature-programmed desorption (CO-TPD) analysis was performed, and the corresponding profiles are shown in Figure 3.11. They mainly exhibited three peaks for CO desorption. One peak below about 250 °C was ascribed to physisorption on the surface of the catalyst.[44] The other two peaks at about 350 and 400 °C were attributed to the desorption of moderately and strongly adsorbed CO, respectively.[45] The desorption temperatures remained almost constant over the reduced CuZn-SC-Px catalysts, suggesting that the strength of interaction between CO and the Cu surfaces was almost same.[45] However, the amount of desorbed CO were different among all the samples. As presented in Table 3.3, the amount of desorbed CO first increased with increasing PEG dosage, and reached a maximum of 0.182 mmol/g over the CuZn-SC-P5. Then it declined with further increasing PEG dosage on CuZn-SC-P8. This trend was in agreement with that of the Cu^0 surface area, indicating that the higher Cu^0 surface area was favorable for adsorbing more CO molecules.

We further used *in-situ* XPS analysis to characterize the CuZn-SC-P5 sample. The CuZn-SC-P5, after *in-situ* reduction in the XPS instrument, was analyzed and is presented in Figure 3.7d-f (denoted as CuZn-SC-P5-Reduced). It generated a lower binding energy of the Cu 2p region than the calcined CuZn-SC-P5 (CuZn-SC-P5-calcined). The Cu 2p 3/2 peak at 932.3 eV, with the absence of satellite characteristic peaks at around 942 eV (Figure 3.7d), implies that the copper species in CuZn-SC-P5- reduced exists as low oxidation state of Cu species (Cu^0 or Cu^{+1}).[31,32] The Cu (LMM) Auger peaks at 918.6 eV suggests that the Cu^0 was the main phase on surface of the CuZn-SC-P5-Reduced, as depicted in Figure 3.12.[46,47] This is in good agreement with the high reduction degree from H_2-TPR results. The Zn 2p region uncovered that ZnO was the main species both in the CuZn-SC-P5-reduced and CuZn-SC-P5-calcined (Figure 3.7e).[33,34] But the CuZn-SC-P5-reduced displayed a weak shoulder peak for $Zn(OH)_2$ species. This implies that the reduction treatment can decrease the concentration of $Zn(OH)_2$ species. Additionally, the O 1s peaks of CuZn-SC-P5-reduced revealed a lower intensity of the surface chemisorbed oxygen than that of CuZn-SC-P5-caicined (Figure 3.7f).[35,36] Therefore, we confirm that the concentration of surface chemisorbed oxygen was reduced via the reduction possess. The appropriate reduction temperature should be used to protect surface functional groups and inhibit excessive agglomeration of the Cu nanoparticles.

The catalytic performance of alcohol-assisted LT-MS was evaluated at 170 °C over the CuZn-SC-Px catalysts. Although the product selectivity to CH_3OH, $HCOOCH_3$, or 2-butyl formate was very similar on these CuZn-SC-Px catalysts, the conversions of CO and total carbon were significantly different from each other (Table 3.4). CuZn-SC-P0 displayed a CO conversion of 49.7 % and a total carbon conversion of 43.7 %. Compared to CuZn-SC-P0, the CuZn-SC-P3 and CuZn-SC-P5 produced higher conversions of CO and total carbon. This suggests that the CuZn-SC-Px catalysts with the PEG treatment enhanced the ability of CO conversion. CuZn-SC-P8 revealed lower conversions of CO and total carbon than CuZn-SC-P3 and CuZn-SC-P5. This implies that the high dosage of PEG treatment can lead to lowering the activity of alcohol-assisted LT-MS. According to these catalytic results, the CuZn-SC-P5 exhibited the best performance compared to the other three CuZn-SC-Px catalysts.

In addition, we also evaluated the stability of CuZn-SC-P5 for alcohol-assisted LT-MS. As shown in Figure 3.13, an upward trend during the first 10 h was observed, likely because of the dilution influence from dead volume of the initial reactor system. The negative conversion of CO_2 was generated in the initial period, due to extremely low CO_2 concentration in the feed gas and CO_2 formation via water-gas shift reaction. After the test of 50 h, the conversions of CO and total carbon were stabilized at 52.7 and 49.3 %, respectively. These results demonstrated that the CuZn-SC-P5 stably promoted the alcohol-assisted LT-MS reaction at 170 °C

To further compare the catalytic activity, the turnover frequency (TOF) of total carbon was calculated based on the Cu dispersion, and is compared in Table 3.5. The TOF value increased from 3.29 to 3.31 h^{-1} on CuZn-SC-Px, and reached a maximum value of 3.40 h^{-1} over the CuZn-SC-P5. But the value decreased to 3.27 h^{-1} on CuZn-SC-P8 with further increasing the PEG amount. The space-time yield (STY) of methanol for CuZn-SC-Px is also shown in Table 3.5. They displayed the same trend as the TOF on CuZn-SC-Px. The CuZn-SC-P5 generated a maximum methanol STY of 94.7 g kg^{-1} h^{-1}. To unveil the relationship between the copper surface area and the activity of methanol synthesis, we further employed the methanol STY as a function of the exposed Cu^0 surface area of CuZn-SC-Px (Figure 3.10). The results clearly demonstrated that the methanol STY exhibited a good linear relationship with the Cu^0 surface area.

In combination of the characterization results, the CuZn-SC-Px catalysts displayed similar elemental composition and particle size of the copper and zinc. But the XPS results demonstrated that CuZn-SC-P5 possessed abundant surface Zn-OH hydroxyl groups, which are beneficial for promoting the stability of Cu nanoparticles. The N_2 adsorption-desorption and N_2O chemisorption analyses further proved that the CuZn-SC-P5 formed higher porosity and larger Cu^0 surface area than the others. The CO-TPD profile also demonstrated that the CuZn-SC-P5 possessed an excellent behavior of CO adsorption. Therefore, although the CuZn-SC-P3, CuZn-SC-P5 and CuZn-SC-P8 produced similar Cu content and BET surface area, the CuZn-SC-P5 still exhibited the best conversions of CO and total carbon among the CuZn-SC-Px catalysts.

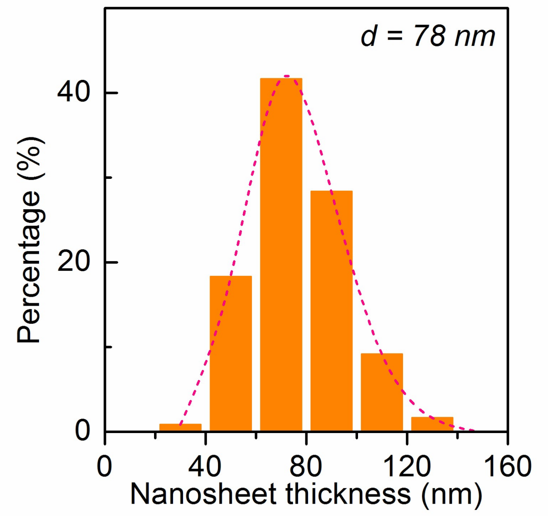

Figure 3.2 The size distribution of sheet thickness for the CuZn-SC-P5. Statistical analysis of the thickness distribution was according to the 120 sheets of CuZn-SC-P5, and the average sheet thickness was about 78 nm.

Table 3.1 Physicochemical properties for the CuZn-based catalysts

Sample	Weight (wt%)[a]			Particle size (nm)[b]		BET area (m^2/g)[c]	Cu^0 area (m^2/g)[d]	Cu dispersion (%)[e]	Pore size (nm)[f]
	Cu	Zn	O	Cu	ZnO				
CuZn-SC-P0	37.4	38.6	24.0	8.7	8.7	70.7	22.6	11.7	7.5
CuZn-SC-P3	38.6	38.5	22.9	8.8	9.5	83.7	27.3	12.4	9.0
CuZn-SC-P5	38.6	39.1	22.3	9.6	9.1	88.5	29.8	12.9	9.2
CuZn-SC-P8	37.6	38.7	23.7	9.5	9.9	82.6	25.2	11.8	8.2
CuZn-P0	38.2	35.4	26.4	8.5	8.3	66.5	21.8	11.2	7.7
CuZn-P5	39.0	37.9	23.1	8.9	9.3	82.1	26.2	11.9	8.3
CuZn-P8	38.2	37.7	24.1	13.4	9.6	81.0	24.4	11.3	8.1

(a) Measured by the XRF over the calcined samples.

(b) Calculated by the XRD from the reduced samples. The particle sizes of Cu and ZnO were calculated based on the Scherrer equation at $2\theta = 43.3°$ and $36.1°$, respectively.

(c) Calculated based on the method of BET about the calcined samples.

(d) Determined by N_2O chemisorption on the reduced samples.

(e) Analysed by N_2O chemisorption from the reduced samples.

(f) Evaluated by the BJH method on the calcined samples.

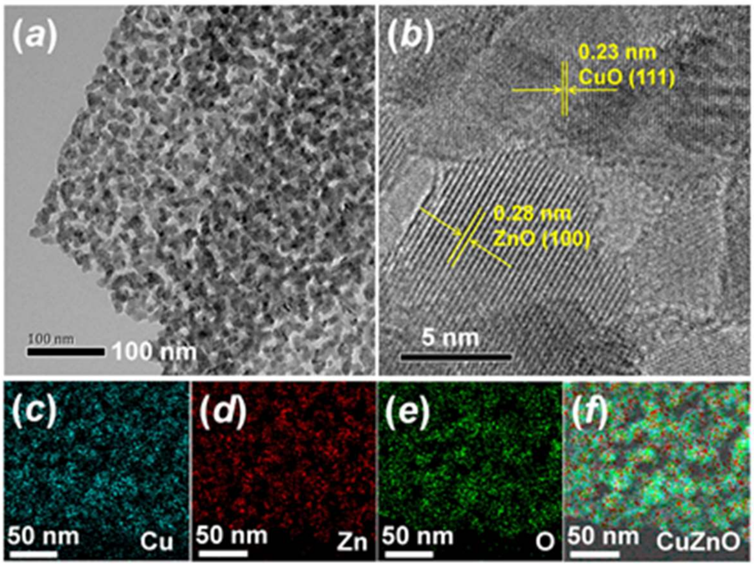

Figure 3.3 TEM analyses for the CuZn-SC-P5 catalyst after the calcination. (a) TEM image of the calcined CuZn-SC-P5, (b) high-magnification TEM image of the calcined CuZn-SC-P5; Elemental mapping of the calcined CuZn-SC-P5: (c) Cu, (d) Zn, (e) O (f) Merged.

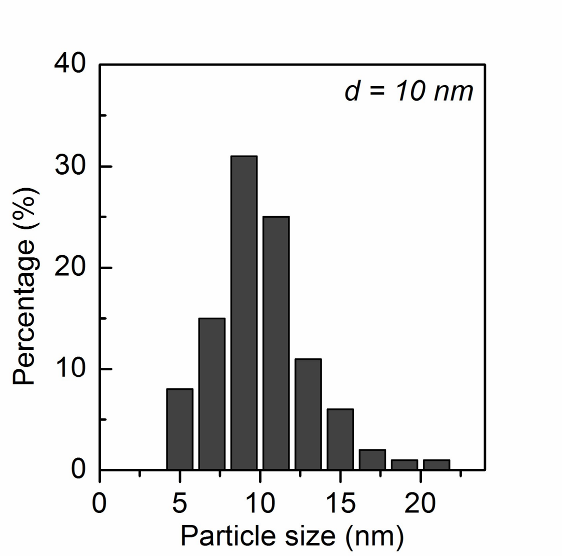

Figure 3.4 The particle size distribution for the CuZn-SC-P5. Statistical analysis of the size distribution was based on the 100 metal-oxide particles, and the average particle size was about 10 nm.

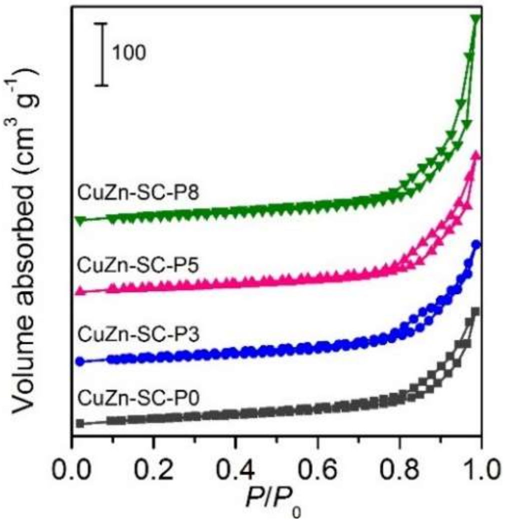

Figure 3.5 N_2 adsorption-desorption isotherms for the calcined CuZn-SC-Px.

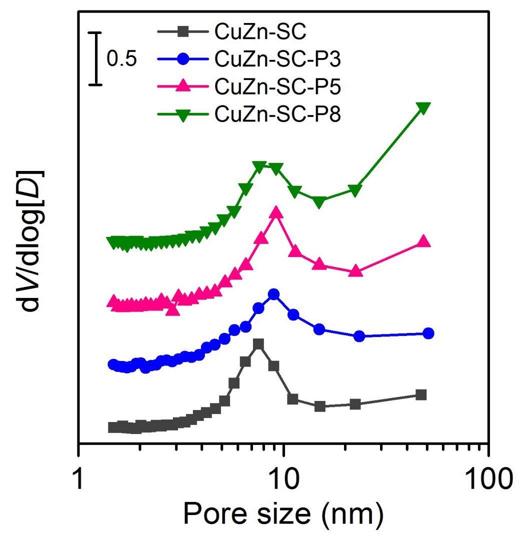

Figure 3.6 Pore-diameter distributions for the CuZn-SC-Px.

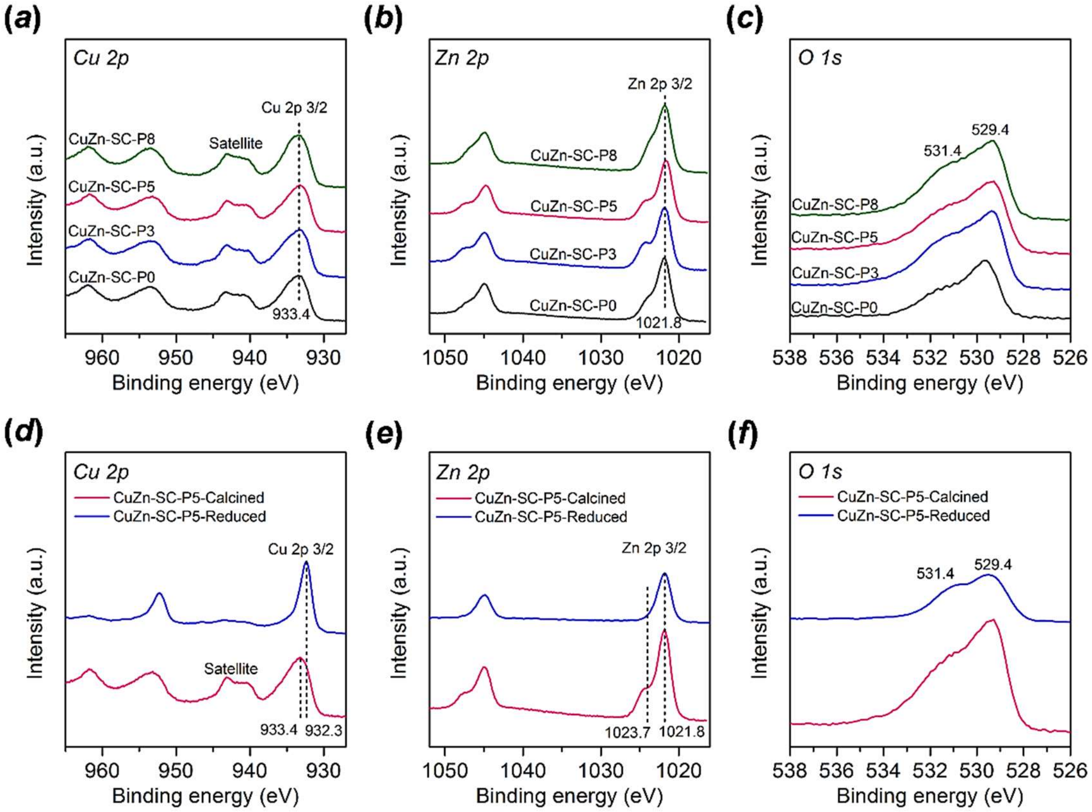

Figure 3.7 XPS spectra for the CuZn-SC-Px samples. (a) Cu 2p region for the calcined CuZn-SC-Px, (b) Zn 2p region for the calcined CuZn-SC-Px, (c) O 1s region for the calcined CuZn-SC-Px, (d) Cu 2p region for the CuZn-SC-P5-Calcined and CuZn-SC-P5-Reduced, (e) Zn 2p region for the CuZn-SC-P5-Calcined and CuZn-SC-P5-Reduced, (f) O 1s region for the CuZn-SC-P5-Calcined and CuZn-SC-P5-Reduced.

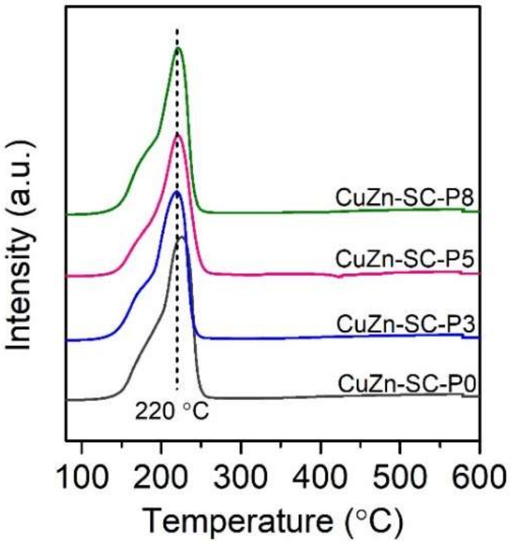

Figure 3.8 H_2-TPR profiles for the calcined CuZn-SC-Px catalysts.

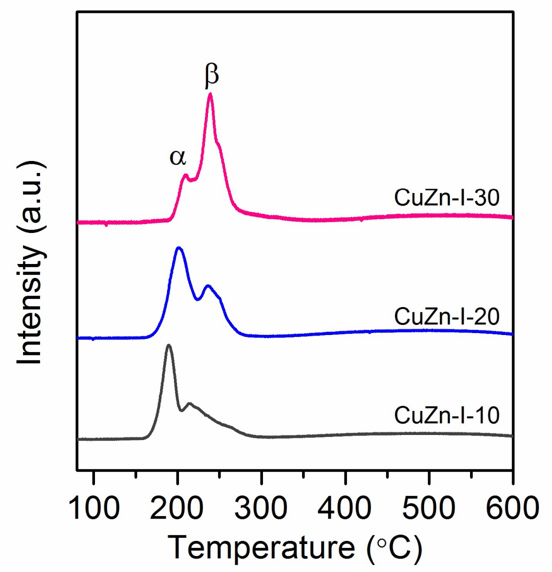

Figure 3.9 H_2-TPR profiles for the calcined CuZn-I-x catalysts. The x represents Cu contents for the CuZn-based catalysts.

Table 3.2. Reduction degree for the CuZn-SC-Px and CuZn-Px catalysts

Sample	Peak position at low temperature (°C)	Peak position at high temperature (°C)	Shoulder peak (°C)	Reduction degree[a] (%)
CuZn-SC-P0	184.9	221.2	-	70.5
CuZn-SC-P3	172.9	224.3	-	74.5
CuZn-SC-P5	172.9	220.2	-	73.3
CuZn-SC-P8	174.5	226.4	-	75.1
CuZn-P0	189.6	230.5	-	62.1
CuZn-P5	181.1	220.3	-	64.4
CuZn-P8	180.7	224.8	251.9	58.3

[a] Reduction degree was calculated based on the peak area before 220 °C.

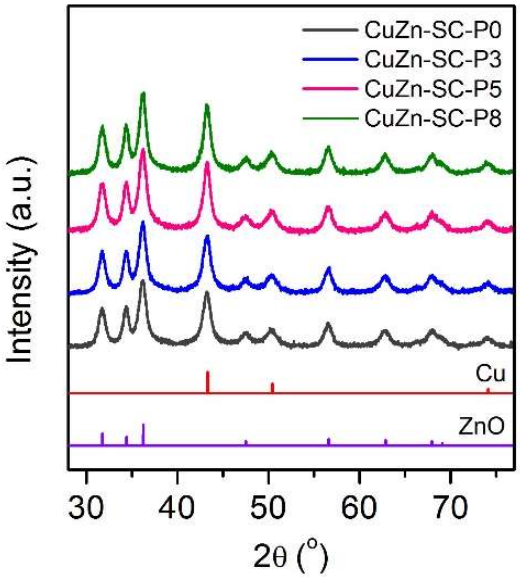

Figure 3.10 XRD patterns of the reduced CuZn-SC-Px catalysts.

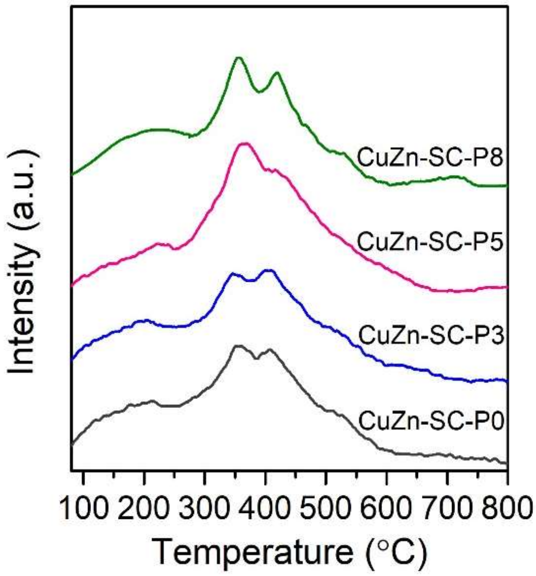

Figure 3.11 CO-TPD profiles of the reduced CuZn-SC-Px catalysts.

Table 3.3 Amount of the desorbed CO over the reduced CuZn-SC-Px catalysts

Catalyst	Amount of desorbed CO[a] (mmol/g)
CuZn-SC-P0	0.145
CuZn-SC-P3	0.169
CuZn-SC-P5	0.182
CuZn-SC-P8	0.151

[a] Measured by CO -TPD analysis.

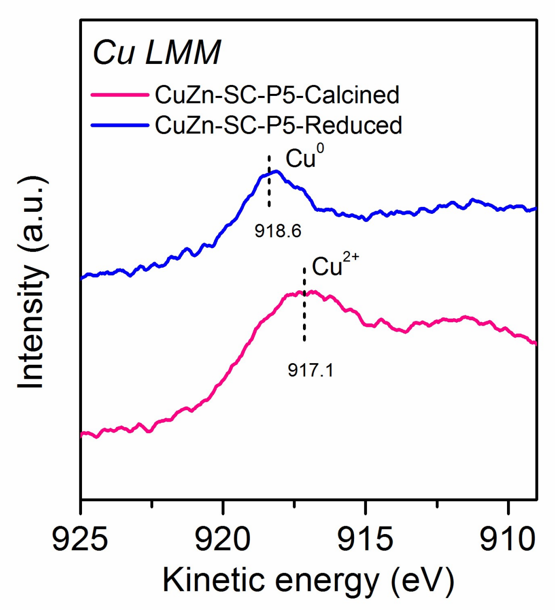

Figure 3.12 Auger spectra for Cu LMM region for the CuZn-SC-P5-Calcined and CuZn-SC-P5-Reduced.[3,4]

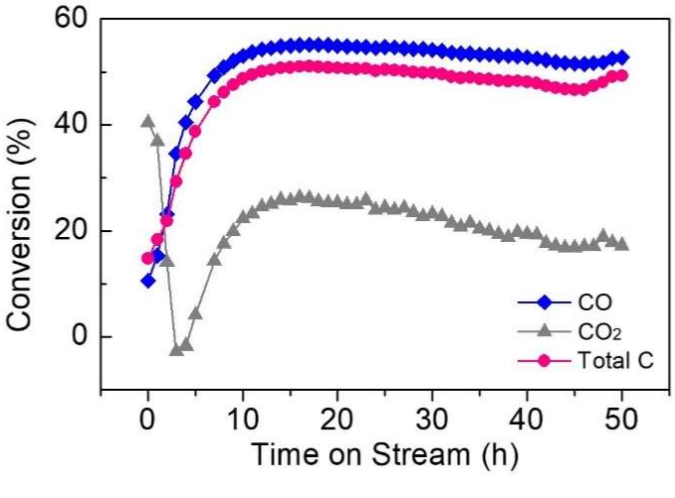

Figure 3.13 Stability of the CuZn-SC-P5 catalyst in alcohol-assisted LT-MS. Reaction condition: catalyst weight, 3.0 g; temperature, 170 °C; pressure, 5.0 MPa; solvent, 2-butanol (40 mL); $CO/CO_2/H_2/Ar$ = 29.5/4.9/62.6/3.0; flow rate, 20 mL/min.

Table 3.4 Catalytic performance of alcohol-assisted LT-MS over the CuZn-SC-Px catalysts

Sample	Conversion (%)			Selectivity (%)		
	CO	CO_2	Total C	CH_3OH	$HCOOCH_3$	2-Butyl formate
CuZn-SC-P0	49.7	7.2	43.7	96.9	0.2	2.8
CuZn-SC-P3	53.3	2.6	46.1	97.4	0.2	2.4
CuZn-SC-P5	55.8	11.3	49.5	97.4	0.2	2.4
CuZn-SC-P8	50.8	-0.3	43.6	97.7	0.2	2.1

Reaction conditions: catalyst weight, 3.0 g; temperature, 170 °C; pressure, 5.0 MPa; solvent, 2-butanol (40 mL); $CO/CO_2/H_2/Ar$ = 29.5/4.9/62.6/3.0; flow rate, 20 mL/min; time on stream, 20 h.

Table 3.5 Cu^0 surface area, TOF and STY for the CuZn-based catalysts

Sample	Cu^0 surface area[a] (m^2/g)	TOF[b] (h^{-1})	STY[c] ($g\ kg^{-1}\ h^{-1}$)
CuZn-SC-P0	22.6	3.29	83.1
CuZn-SC-P3	27.3	3.31	88.2
CuZn-SC-P5	29.8	3.40	94.7
CuZn-SC-P8	25.2	3.27	83.7
CuZn-P0	21.8	3.30	79.5
CuZn-P5	26.2	3.37	87.0
CuZn-P8	24.4	3.04	72.9

[a] Determined by N_2O chemisorption method. [b] Total carbon turnover frequency. [c] Space-time yield of methanol.

3.3.2 CuZn-Px for alcohol-assisted LT-MS

We utilized traditional drying method to synthesize the CuZn-Px catalysts. The SEM results exhibited that the calcined CuZn-Px also possessed sheet structures (Figure 3.14). The XRF results demonstrated that they have similar elemental composition (Table 3.1). In addition, the N_2 adsorption-desorption analyses demonstrated that CuZn-P5 and CuZn-P8 formed a higher BET area than CuZn-P0. However, compared to CuZn-SC-P5 from supercritical CO_2 drying, CuZn-P5 showed a lower BET area and volume of adsorbed/desorbed N_2 (Table 3.1 and Figure 3.15). These phenomena also indicate that the PEG treatment improved the BET area. Moreover, the supercritical CO_2 drying process further promoted the BET area and the porosity.

We further analyzed the chemical states of the calcined CuZn-Px catalysts by XPS (Figure 3.16a). The Cu 2p region is shown in Fig. S8a. The CuZn-Px catalysts still displayed the same chemical states of the Cu species. The Zn 2p region in Figure 3.16b unveiled that the shoulder peaks at 1023.7 eV disappeared on CuZn-P8. This is consistent with the Zn 2p analyses from the CuZn-SC-Px catalysts. This further implies that the treatment with high PEG dosage inhibited the formation of $Zn(OH)_2$ species. Although the O 1s peaks revealed that the high dosage of PEG treatment increased the concentration of surface chemisorbed oxygen (Figure 3.16c), CuZn-P8 still displayed a larger Cu particle size than the other CuZn-Px catalysts after H_2 reduction (Table 3.1). This indicates that the surface chemisorbed oxygen did not stabilize the Cu particles. By contrast, the surface Zn-OH hydroxyl groups may play a key role on the stability of the Cu particles.

We also employed H_2-TPR to analyze the calcined CuZn-Px catalysts, as indicated in Figure 3.17. The analysis results revealed that the reduction degrees were about 58-62 % on the CuZn-Px samples, when the reduction temperature was 220 °C (Table 3.2). They were lower than the reduction degrees of 70-75 % on the CuZn-SC-Px catalysts. In addition, we also utilized XRD and N_2O chemisorption to characterize the reduced CuZn-Px catalysts (Table 3.1 and Figure 3.18). The XRD results exhibited that the Cu or ZnO particle sizes of CuZn-P0 and CuZn-P5 were similar with those of the CuZn-SC-Px catalysts. But CuZn-P8 generated a severe agglomeration of Cu metal, and it formed a larger Cu particle size than CuZn-SC-P8. The N_2O chemisorption analyses demonstrated that the CuZn-P5 has the best Cu^0 surface area among the CuZn-Px samples. However, it was still lower than that of CuZn-SC-P5. These observations clearly showed that the two strategies, PEG treatment and supercritical CO_2 drying, can effectively optimize reduction degree, Cu particle size and Cu^0 surface area in the preparation processes.

We further tested the catalytic performance of alcohol-assisted LT-MS over the CuZn-Px catalysts. As in Table 3.6, the CuZn-Px catalysts also displayed similar products selectivities. The methanol selectivity reached about 97 %, and the conversions of CO and total carbon were also different. CuZn-P0 exhibited a CO conversion of 47.6 % and a total carbon conversion of 41.7 %. The CuZn-P8 realized a CO conversion of 44.5 % and a total carbon conversion of 38.3 %. Compared to the CuZn-P0 and CuZn-P8, CuZn-P5 exhibited higher conversions of CO and total carbon. This demonstrated that the appropriate PEG treatment promoted the activity, but the high dosage of PEG treatment decreased the conversions. The XRD and N_2O chemisorption analyses have proved that the high dosage of PEG contents led to a large Cu particle size and low Cu^0 surface area (Table 3.1). Thus, CuZn-P5 exhibited better performance than CuZn-P8.

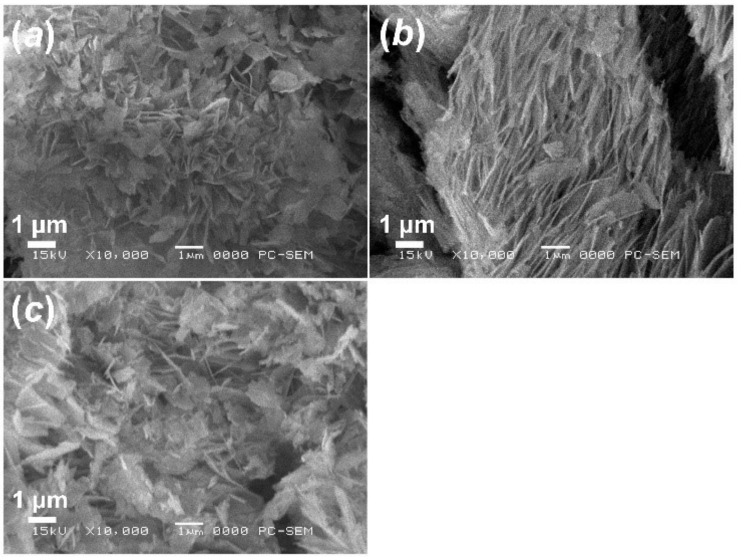

Figure 3.14 SEM analyses for the calcined CuZn-Px samples. (a) CuZn-P0, (b) CuZn-P5, and (c) CuZn-P8.

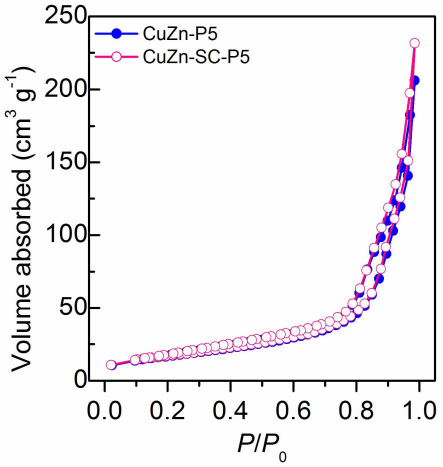

Figure 3.15. N_2 adsorption-desorption isotherms for the CuZn-P5 and CuZn-SC-P5.

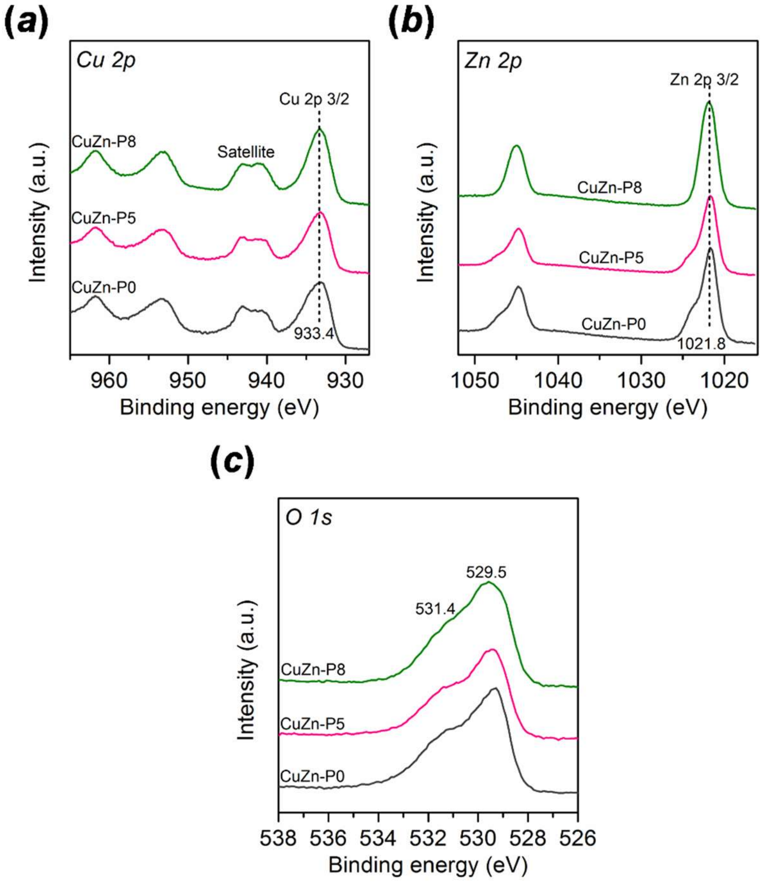

Figure 3.16 XPS spectra for the CuZn-Px samples. [5-7] (a) Cu 2p region for the CuZn-Px, (b) Zn 2p region for the CuZn-Px, (c) O 1s region for the CuZn-Px.

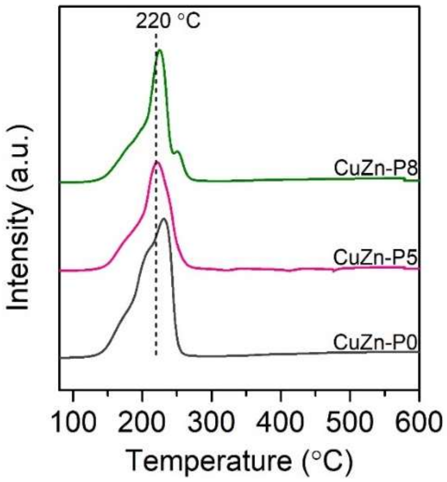

Figure 3.17 H_2-TPR profiles for the calcined CuZn-Px catalysts. According to the H_2-TPR analyses, the reduction degrees were only 58-62 % for the CuZn-Px catalysts, when the reduction temperature was at 220 °C.

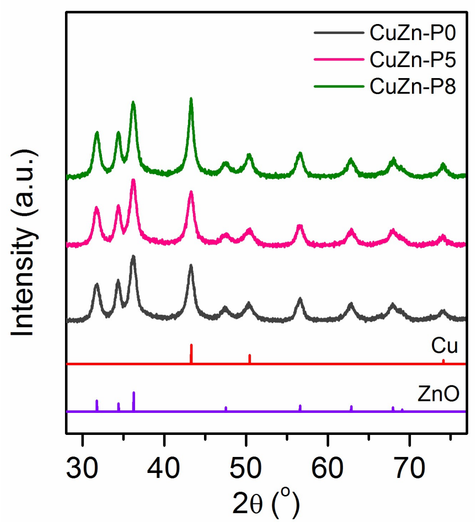

Figure 3.18 XRD results for the reduced CuZn-Px catalysts. Based on the Scherrer equation at $2\theta = 43.3°$ and 36.1°, the particle sizes of Cu and ZnO were calculated, respectively.

Table 3.6 Catalytic performance of alcohol-assisted LT-MS over the CuZn-Px catalysts

Sample	Conversion (%)			Selectivity (%)		
	CO	CO_2	Total C	CH_3OH	$HCOOCH_3$	2-Butyl formate
CuZn-P0	47.6	5.8	41.7	97.1	0.3	2.6
CuZn-P5	51.4	8.1	45.3	97.8	0.2	2.0
CuZn-P8	44.5	0.7	38.3	96.9	0.3	2.9

Reaction conditions: catalyst weight, 3.0 g; temperature, 170 °C; pressure, 5.0 MPa; solvent, 2-butanol (40 mL); $CO/CO_2/H_2/Ar$ = 29.5/4.9/62.6/3.0; flow rate, 20 mL/min; time on stream, 20 hours.

3.3.3 Different types of CuZn-based catalysts for alcohol-assisted LT-MS

We applied the traditional impregnation method to prepare the CuZn-I catalyst, and further coupled this method with the supercritical CO_2 drying to synthesize the CuZn-I-SC catalyst. The performance of alcohol-assisted LT-MS, over the CuZn-I and CuZn-I-SC, is shown in Figure 3.19 and Table 3.7. CuZn-I and CuZn-I-SC revealed that conversions of CO and total carbon were about 3-5 %. Although the Cu contents of 35 wt% were the same for the two catalysts, they displayed much lower conversions than the CuZn-Px and the CuZn-SC-Px catalysts. This observation allows us to consider that the impregnation method did not efficiently activate the molecules of CO and H_2 at such a low temperature of 170 °C.

The *In-situ* DRIFT spectra of CO adsorption for CuZn-I-SC and CuZn-SC-P5 are shown in Figure 3.20. Before the CO adsorption, the two samples were pretreated by *in-situ* reduction of H_2. Then, the CO adsorption was conducted at room temperature. The results showed that CuZn-SC-P5 generated very strong CO adsorption. The adsorption peaks at 2103, 2130 and 2168 cm^{-1} should be ascribed to the CO adsorbed on Cu^0 and Cu^{+1} and Cu^{+2}, respectively.[48,49] However, CuZn-I-SC only adsorbed CO weakly. This further demonstrated that it is difficult to activate the CO molecules on CuZn-I-SC. In contrast, CuZn-SC-P5 revealed high intensity for CO adsorption peaks, indicating that it possessed a strong interaction between the CO molecules and Cu surface, and high probability for the CO activation.

In the impregnation method, we employed ZnO powder as the catalyst support. After the impregnation, the Cu particles should be distributed on outer surface of the ZnO powder (Figure 3.21a). This resulted in severe agglomeration of Cu to generate large particle size and low probability of CO activation (Figure 3.20 and 3.22). Moreover, the number of Cu-Zn interface was significantly decreased. It can further accelerate agglomeration and sintering of the Cu species and lower the activity. Consequently, CuZn-I and CuZn-I-SC displayed low conversion for the alcohol-assisted LT-MS. In contrast, we employed the urea co-precipitation method to prepare the CuZn-Px and the CuZn-SC-Px catalysts. Urea was slowly decomposed to produce a uniform basic environment. It can effectively inhibit the severe agglomeration of Cu, and the uniform and small precipitates can produce a large number of Cu-Zn interface (Figure 3.21b). These phenomena have been demonstrated by our XRD and TEM characterization analyses (Figure 3.3 and 3.10 and Table 3.1). Therefore, CuZn-Px and CuZn-SC-Px exhibited remarkable improvement in the activity of alcohol-assisted LT-MS.

Compared to the CuZn-I, CuZn-P0 and CuZn-P5 catalysts, the CuZn-I-SC, CuZn-SC-P0, and CuZn-SC-P5 catalysts, prepared from the supercritical CO_2 drying, showed enhanced performance. The H_2-TPR analyses clearly uncovered that CuZn-SC-Px possessed higher reduction degrees than CuZn-Px (Table 3.2). According to this analysis, the optimized performance of CuZn-I-SC, CuZn-SC-P0, and CuZn-SC-P5 should be due to the high reduction degrees caused by supercritical CO_2 drying. In addition, CuZn-P5 and CuZn-SC-P5 displayed higher performance than CuZn-P0 and CuZn-SC-P0. The XPS results have demonstrated that the appropriate dosage of PEG treatment can promote the activity of alcohol-assisted LT-MS. Therefore, we confirm that the PEG treatment was beneficial for enhancing the activity. As a result, using the urea co-precipitation method accompanied by PEG treatment and supercritical CO_2 drying, we obtained the excellent performance of alcohol-assisted LT-MS over CuZn-SC-P5.

To further compare the influence of the urea co-precipitation method, we employed traditional Na_2CO_3 co-precipitation method to prepare CuZn-Na catalyst. The catalytic performance and BET area were showed in Table 3.8. The CuZn-Na displayed a CO conversion of 41.4 % and a BET area of 60.2 m^2 g^{-1}. In comparison with CuZn-Na, the CuZn-P0, synthesized from urea co-precipitation, exhibited higher CO conversion and

BET area. Further, CuZn-SC-P5, synthesized from urea co-precipitation with the PEG treatment and supercritical CO_2 drying, displayed higher CO conversion and BET area than CuZn-P0. These results demonstrated that the urea co-precipitation method improved the catalytic performance and BET area of the CuZn-based catalysts. Moreover, the PEG treatment and supercritical CO_2 drying can further optimize the CuZn-based catalysts, on the basis of the urea co-precipitation method.

To illustrate the mechanism of alcohol-assisted LT-MS, *in-situ* DRIFT was further performed on CuZn-SC-P5. The DRIFT results were displayed in Figure 3.23. In the range of 3100~2800 cm^{-1}, the IR band at 2972 and 2884 cm^{-1} should be ascribed to ν(CH) of 2-butanol and methanol in the adsorption species, respectively. The band at 2935 and 2853 cm^{-1} was attributed to ν(CH) of 2-butanol and methanol species in the gas phase, respectively (Figure 3.23a).[12,50] Although CuZn-SC-P5 was purged in He after 30 min, it still displayed high peak intensity for 2-butanol adsorption. In the range of 1900~1300 cm^{-1}, we observed an obvious change that the peak intensity increased with He purging (Figure 3.23b). The band at 1664, 1590 and 1380 cm^{-1} was due to the groups of C=O, OCO and CH_3, respectively.[12,17] The band at 1500~1400 cm^{-1} should be attributed to the C-O and C-C stretching vibrations, and the band at 1601 cm^{-1} was attributed to H_2O adsorbed on Cu species. [12] In particular, the band for HCOO–Zn and HCOO-Cu adsorption species was observed at 1529 and 1351 cm^{-1}, respectively. [12,17] This indicates that the formate was the reaction intermediate. Additionally, we have detected 2-butyl formate in the reaction products. Therefore, we confirm that 2-butanol served not only as solvent, but also as catalytic promoter in the systems.

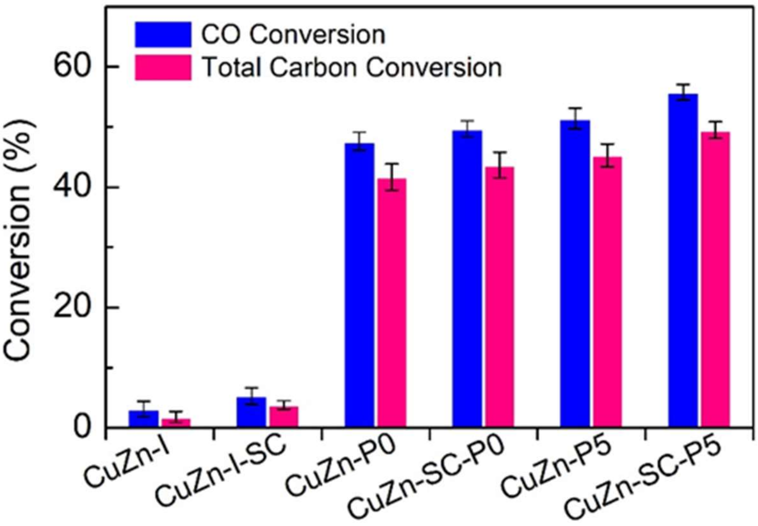

Figure 3.19 CO conversion and total carbon conversion over the CuZn-based catalysts from different preparation methods. Reaction conditions: catalyst weight, 3.0 g; temperature, 170 °C; pressure, 5.0 MPa; solvent, 2-butanol (40 mL); $CO/CO_2/H_2/Ar = 29.5/4.9/62.6/3.0$; flow rate, 20 mL/min; time on stream, 20 hours.

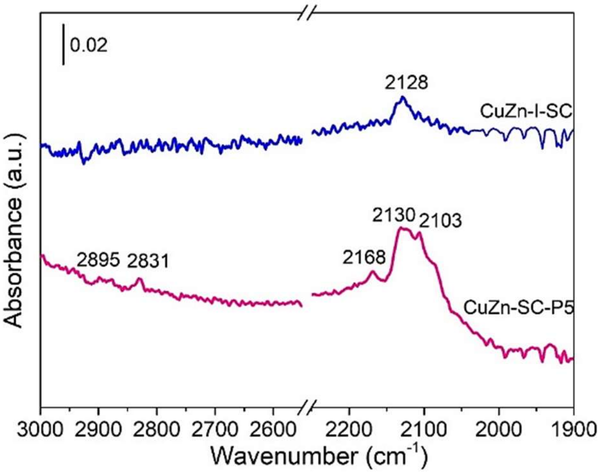

Figure 3.20 *in-situ* DRIFT spectra of CO adsorption over the CuZn-I-SC and CuZn-SC-P5 catalysts after He purge for 20 minutes.

Table 3.7 Catalytic performance of alcohol-assisted LT-MS over the CuZn-based catalysts from different preparation methods

Sample	Conversion (%)			Selectivity (%)		
	CO	CO_2	Total C	CH_3OH	$HCOOCH_3$	2-Butyl formate
CuZn-I	3.1	-6.4	1.8	100	/	/
CuZn-I-SC	5.3	-4.8	3.8	100	/	/
CuZn-P0	47.6	5.8	41.7	97.1	0.3	2.6
CuZn-SC-P0	49.7	7.2	43.7	96.9	0.2	2.8
CuZn-P5	51.4	8.1	45.3	97.8	0.2	2.0
CuZn-SC-P5	55.8	11.3	49.5	97.4	0.2	2.4

Reaction conditions: catalyst weight, 3.0 g; temperature, 170 °C; pressure, 5.0 MPa; solvent, 2-butanol (40 mL); $CO/CO_2/H_2/Ar$ = 29.5/4.9/62.6/3.0; flow rate, 20 mL/min; time on stream, 20 h.

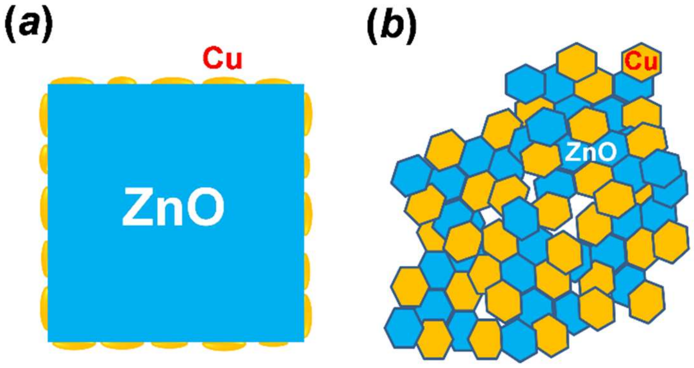

Figure 3.21 Schematic illustrations for the CuZn-based catalysts from different preparation methods. (a) Traditional impregnation method and (b) urea co-precipitation method.

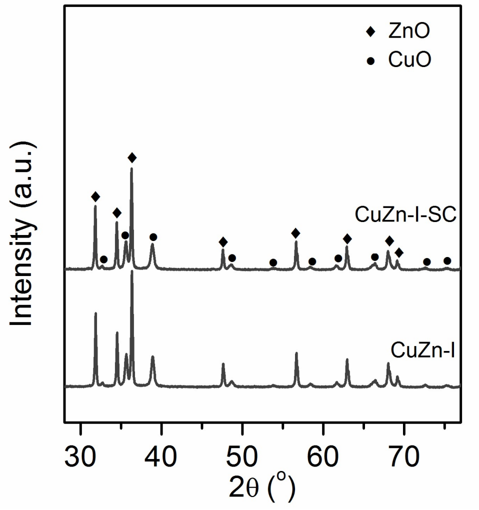

Figure 3.22 XRD patterns for the precursors of CuZn-I-SC and CuZn-I.

Table 3.8 Catalytic performance of alcohol-assisted LT-MS over the CuZn-Na, CuZn-P0 and CuZn-SC-P5.

Samples[a]	Conversion (%)			Selectivity (%)			BET area[b] (m^2/g)
	CO	CO_2	Total C	CH_3OH	$HCOOCH_3$	2-Butyl formate	
CuZn-Na	41.4	5.4	36.8	98.0	0.1	1.8	60.2
CuZn-P0	47.6	5.8	41.7	97.1	0.3	2.6	66.5
CuZn-SC-P5	55.8	11.3	49.5	97.4	0.2	2.4	88.5

[a] Reaction conditions: catalyst weight, 3.0 g; temperature, 170 °C; pressure, 5.0 MPa; solvent, 2-butanol (40 mL); $CO/CO_2/H_2/Ar$ = 29.5/4.9/62.6/3.0; flow rate, 20 mL/min; time on stream, 20 h.

[b] BET surface area determined by N_2 adsorption-desorption analysis.

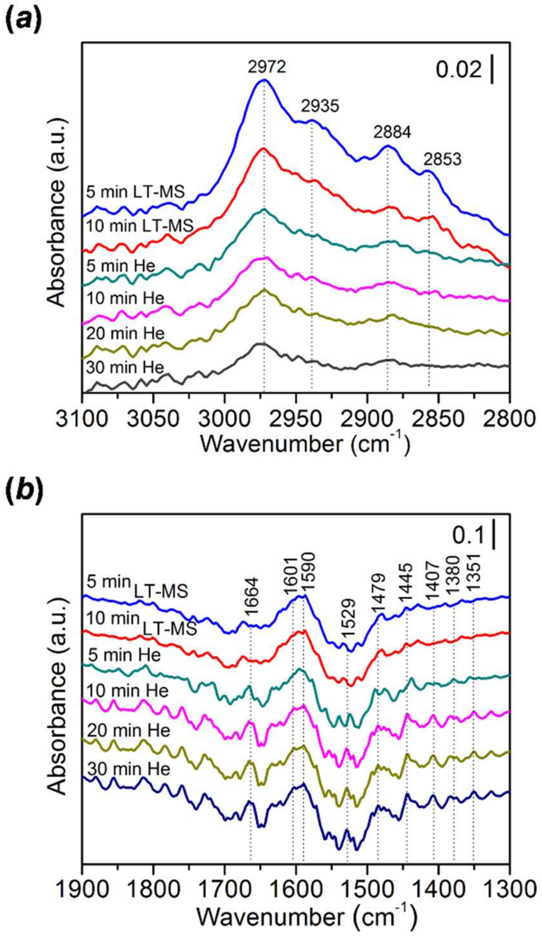

Figure 3.23 *In-situ* DRIFT spectra of alcohol-assisted LT-MS over the CuZn-SC-P5.

3.4 Conclusions

In conclusion, we have successfully employed PEG treatment and supercritical CO_2 drying to improve the traditional co-precipitation method for fabrication of CuZn-based catalysts for alcohol-assisted low-temperature methanol synthesis (LT-MS). The catalytic reaction results revealed that the CuZn-SC-P5 catalyst, after both improvement strategies, exhibited excellent performance. The conversions of CO and total carbon reached 55.8 and 49.5 %, respectively. Moreover, the CuZn-SC-P5 uncovered much higher conversions than the CuZn-based catalysts prepared by traditional impregnation method, and a better performance than the catalysts treated by sole PEG treatment or sole supercritical CO_2 drying. Our characterization analysis demonstrated that the moderate PEG treatment increased BET area, surface functional groups and Cu^0 surface area for the CuZn-based catalysts. Supercritical CO_2 drying further optimized these CuZn-based catalysts. This work offers two premium strategies to improve the fabrication processes of CuZn-based catalysts, and also facilitates new catalyst designs in other reaction systems.

References

[1] N. Tsubaki, M. Ito and K. Fujimoto, J Catal., 2001, 197, 224-227.

[2] K. C. Waugh, Catal. Today, 1992, 15, 51-75.

[3] R. G. Herman, G. W. Simmons and K. Klier, Stud. Surf. Sci. Catal., 1981, 7, 475-489.

[4] G. H. Graaf, P. J. J. M. Sijtsema, E. J. Stamhuis and G. E. H. Joosten, Chem. Eng. Sci., 1986, 41, 2883-2890.

[5] T. Chang, R. W. Rousseau and P. K. Kilpatrick, Ind. Eng. Chem. Process Des. Dev., 1986, 25, 477-481.

[6] N. Tsubaki, J. Zeng, Y. Yoneyama and K. Fujimoto, Catal. Commun., 2001, 2, 213-217.

[7] J. Haggin, Chemical Engineering News, 1986, 21, Aug. 4.

[8] Brookhaven National Laboratory, US pat., 4619946, 4623634, 4613623, 1990, 4935395, 1990.

[9] J. A. Christiansen, US Patent, 1919, 1302011.

[10] Z. Liu, J. W. Tierney, Y. T. Shah and I. Wender, Fuel Process. Technol., 1989, 23, 149-167.

[11] V. M. Palekar, J.W. Tierney and I. Wender, Appl. Catal. A: Gen., 1993, 103, 105-122.

[12] R. Yang, Y. Fu, Y. Zhang and N. Tsubaki, J. Catal., 2004, 228, 23-35.

[13] J. Zeng, K. Fujimoto and N. Tsubaki, Energy Fuels, 2002, 16, 83-86.

[14] P. Reubroycharoen, T. Yamagami, T. Vitidsant, Y. Yoneyama, M. Ito and N. Tsubaki, Energy Fuels, 2003, 17, 817-821.

[15] R. Yang, X. Yu, Y. Zhang, W. Li and N. Tsubaki, Fuel, 2008, 87, 443-450.

[16] L. Shi, G. Yang, K. Tao, Y. Yoneyama, Y. Tan and N. Tsubaki, Acc. Chem. Res., 2013, 46, 1838-1847.

[17] F. Meng, Q. Zhang, G. Yang, R. Yang, Y. Yoneyama and N. Tsubaki, Chem. Eng. J., 2016, 295, 160-166.

[18] R. Fan, M. Kyodo, L. Tan, X. Peng, G. Yang, Y. Yoneyama, R. Yang, Q. Zhang and N. Tsubaki, Fuel Process. Technol., 2017, 167, 69-77.

[19] T. Fujitani, J. Japan Pet. Inst., 2020, 63, 43-51.

[20] S. Kattel, P. J. Ramírez, J. G. Chen, J. A. Rodriguez and Ping Liu, Science, 2017, 355, 1296-1299.

[21] S. Chen, J. Zhang, P. Wang, X. Wang, F. Song, Y. Bai, M. Zhang, H. Xie, and Y. Tan, ChemCatChem, 2019, 11, 1448-1457.

[22] A. A. Tountas, X. Peng, A. V. Tavasoli, P. N. Duchesne, T. L. Dingle, Y. Dong, L. Hurtado, A. Mohan, W. Sun, U. Ulmer, L. Wang, T. E. Wood, C. T. Maravelias, M. M. Sain and Geoffrey A. Ozin, Adv. Sci. 2019, 6, 1801903.

[23] Y. L. Zhang, Y. Yang, J. Zhao, R. Tan, P. Cui and W. Song, J. Sol-Gel Sci. Technol., 2009, 51, 198-203.

[24] A. Budiman, M. Ridwan, S. M. Kim, J. W. Choi, C. W. Yoon, J.M. Ha, D.J. Suh and Y.W. Suh, Appl. Catal. A: Gen., 2013, 462-463, 220-226.

[25] P. Zhang, Y. Araki, X. Feng, H. Li, Y. Fang, F. Chen, L. Shi, X. Peng, Y. Yoneyama, G. Yang and N. Tsubaki, Fuel, 2020, 268, 117213.

[26] C. A. García-González, M. C. Camino-Rey, M. Alnaief, C. Zetzl and I. Smirnova, J. Supercrit. Fluids, 2012, 66, 297-306.

[27] P. C. Rath, J. Patra, D. Saikia, M. Mishra, J. K. Chang and H. M. Kao, J. Mater. Chem. A, 2016, 4, 14222-14233.

[28] J. Dhakshinamoorthy and B. Pullithadathil, J. Phys. Chem. C, 2016, 120, 4087-4096.

[29] K. Xu, J. Wu, C. Fu Tan, G. W. Ho, A. Wei and M. Hong, Nanoscale, 2017, 9, 11574-11583.

[30] JyotiJ. and G.D. Varma, J. Alloys Compd., 2019, 806, 1469-1480.

[31] Y. Wu, E. Garfunkel and T. E. Madey, J. Vac. Sci. Technol. A, 1996, 14, 1662.

[32] A. Yin, X. Guo, W. Dai and K. Fan, J. Phys. Chem. C, 2009, 113, 11003-11013.

[33] H.Y. Chen, S.P. Lau, L. Chen, J. Lin, C.H.A. Huan, K.L. Tan and J.S. Pan, Appl. Sur. Sci., 1999, 152, 193-199.

[34] G. G. Guillén, M. I. M. Palma, B. Krishnan, D. Avellaneda, G.A. Castillo, T.K.D. Roy and S. Shaji, Mater. Chem. Phys., 2015, 162, 561-570.

[35] K. P. Ghoderao, S. N. Jamble and R. B. Kale, Mater. Res. Express, 2017, 4, 105009.

[36] X. Hou, F. Zhou, B. Yu and W. Liu, Mater. Lett., 2007, 61, 2551-2555.

[37] W. Dow, Y. Wang and T. Huang, J. Catal., 1996, 160, 155-170.

[38] A. Bansode, B. Tidona, P. R. von Rohr and A. Urakawa, Catal. Sci. Technol., 2013, 3, 767-778.

[39] X. Courtois, V. Perrichon, M. Primet and G. Bergeret, Stud. Surf. Sci. Catal., 2000, 130, 1031-1036.

[40] R. M. Wang, Y.J. Xing, J. Xu and D.P. Yu, New J. Phys., 2003, 5, 115.1-115.7.

[41] J. Wang, Z. Gao, Z. Li, B. Wang, Y. Yan, Q. Liu, T. Mann, M. Zhang and Z. Jiang, J. Solid State Chem., 2011, 184, 1421-1427.

[42] H. Zhu, C. Zhang and Y. Yin, J. Cryst. Growth, 2004, 270, 722-728.

[43] P. K. Khanna, S. Gaikwad, P. V. Adhyapak, N. Singh and R. Marimuthu, Mater. Lett., 2007, 61, 4711-4714.

[44] F. Song, Y. Tan, H. Xie, Q. Zhang and Y. Han, Fuel Process. Technol., 2014, 126, 88-94.

[45] X. Dong, H. Zhang, G, Lin, Y. Yuan and K. Tsai, Catal. Letters, 2003, 85, 237-246.

[46] A. Maetaki and K. Kishi, Surf. Sci., 1998, 411, 35-45.

[47] J. Batista, A. Pintar, D. Mandrino, M. Jenko and V. Martin, Appl. Catal. A: Gen., 2001, 206, 113-124.

[48] A. Dandekar and M. A. Vannice, J. Catal., 1998, 178, 621–639.

[49] A. G. Sato, D. P. Volanti, D. M. Meira, S. Damyanova, E. Longo and J. M. C. Bueno, J. Catal., 2013, 307, 1–17.

[50] Y. Wang, S. Kattel, W. Gao, K. Li, P. Liu, J.G. Chen and H. Wang, Nat. Commun., 2019, 10, 1166.

Chapter 4

Summary

The rising concentration of CO_2 in the atmosphere, resulting from fossil fuel utilization, is confidently thought to have induced global warming and climate change phenomena. Biomass is a promising renewable source of energy for it can replace fossil fuels. Produced from biomass, coal and nature gas, syngas is a crucial junction point that bridges the non-petroleum carbon resources and other basic chemicals. Therefore, efficiently employing and converting of renewable resources to alternative fuels and chemicals is believed to be a crucial way in current science research field.

The functionalization of catalysts is one of attractive way to boost the catalytic performance and product distribution. In this thesis, we successfully functionalized and synthesized heteroatom incorporation into carbon structure, and K addition were employed to boost their catalytic performances. The nitrogen and K promotor on Fe-based catalyst was prepared for enhanced CO_2 activity and liquid hydrocarbons (C_{5+}). Test under reaction temperature at 300 °C test for 6 hours, pressure 1 MPa, and W/F 12 g.h/mol^{-1}.

As mentioned in Chapter 1, ethylene diamine (EDA) as a nitrogen source was achieving an outstanding performance for the CO_2 hydrogenation process. The nitrogen incorporation into the carbon support contributes to the high dispersion of active iron oxide phase, and to the formation of small-size iron carbides. Meanwhile, enhanced surface basicity resulted from suitable nitrogen doping, which also boosts the selective formation of olefins. In addition, further utilization of electronic K promoter adjusts iron carbide's electron density, thus promoting chain propagation of C_xH_{y-s} adsorbed intermediates. Correspondingly, the catalyst with both nitrogen incorporation into the carbon support structure and potassium modification presents benign catalytic activity as well as higher olefin-rich hydrocarbon selectivity and enhanced catalytic CO_2

hydrogenation performance.

As mentioned in Chapter 2, a serial of spinel-like structure catalysts ($NiFe_2O_x$, $CoFe_2O_x$, $MgFe_2O_x$, $CuFe_2O_x$, and $ZnFe_2O_x$) are successfully fabricated through urea self-combustion method. Compared with reference catalysts show a high CH_4 selectivity. As for $MgFe_2O_x$ catalysts, although product distribution changes little, the olefins hydrogenation ability on catalyst surface becomes stronger than Fe_2O_3 catalysts. However, with the incorporation of Cu promoter, catalytic activity as well as light olefins selectivity are improved owing to the synergistic effect between Cu and Fe species. Among these spinel catalysts, $ZnFe_2O_x$ catalyst exhibits the best catalytic performance with larger light olefins selectivity and chain growth ability. $ZnFe_2O_x$ species from urea self-combustion method, provides a benign route for efficiently catalyzing CO_2 hydrogenation to value hydrocarbon products, especially olefin-rich C_{2+} products.

As mentioned in Chapter 3, the successfully employed PEG treatment and supercritical CO_2 drying to improve the traditional co-precipitation method for fabrication of CuZn-based catalysts for alcohol-assisted low-temperature methanol synthesis (LT-MS). The CuZn-SC-P5 catalyst, after both improvement strategies, exhibited excellent performance. The conversions of CO and total carbon reached 55.8 and 49.5 %, respectively. Moreover, the CuZn-SC-P5 uncovered much higher conversions than the CuZn-based catalysts prepared by traditional impregnation method, and a better performance than the catalysts treated by sole PEG treatment or sole supercritical CO_2 drying.

The new findings in this thesis are beneficial to designing and building functional catalysts for high-value-added chemicals synthesis from non-petroleum source (syngas and CO_2). The presented catalysts preparation method in this thesis can be also extended to other catalysis processes.

List of publications

1. **Rungtiwa Kosol**, Lisheng Guo, Naoya Kodama, Peipei Zhang, Prasert Reubroycharoen, Tharapong Vitidsant, Akira Taguchi, Takayuki Abe, Jienan Chen, Guohui Yang, Yoshiharu Yoneyama, Noritatsu Tsubaki. Iron catalysts supported on nitrogen functionalized carbon for improved CO_2 hydrogenation performance. ***Catalysis Communications***, 2021, 149, 106216. IF = 3.612
2. Fei Chen, Peipei Zhang, Yan Zeng, **Rungtiwa Kosol**, Liwei Xiao, Xiaobo Peng, Jie Li, Guangbo Liu, Jinhu Wu, Guohui Yang, Noritatsu Tsubaki. Vapor-phase low-temperature methanol synthesis from CO_2-containing syngas via self-catalysis of methanol and Cu/ZnO catalysts prepared by solid-state method. ***Applied Catalysis B: Environmental***, 2020, 279, 119382. IF = 16.683
3. Lisheng Guo, Jie Li, Yu Cui, **Rungtiwa Kosol**, Yan Zeng, Guangbo Liu, Jinhu Wu, Tiansheng Zhao, Guohui Yang, Lishu Shao, Peng Zhan, Jienan Chen, Noritatsu Tsubaki. Spinel-structure catalyst catalyzing CO_2 hydrogenation to full spectrum alkenes with an ultra-high yield. ***Chemical Communications***, 2020, 56, 9372-9375. IF = 5.996
4. Jie Yao, Xiaobo Feng, Jiaqi Fan, Yingluo He, **Rungtiwa Kosol**, Yan Zeng, Guangbo Liu, Qingxiang Ma, Guohui Yang, Noritatsu Tsubaki. Effects of mordenite zeolite catalyst synthesis conditions on dimethyl ether carbonylation. ***Microporous and Mesoporous Materials***, 2020, 306, 110431. IF = 4.551
5. Peipei Zhang, Xiaobo Peng, Yuya Araki, Yuan Fang, Yan Zeng, **Rungtiwa Kosol**, Yoshiharu Yoneyama, Guohui Yang, Noritatsu Tsubaki. Fabrication of a CuZn-based catalyst using a polyethylene glycol surfactant and supercritical drying. ***Catalysis Science&Technology***, 2020, 10, 8410-8420. IF = 5.721
6. Lisheng Guo, Jie Li, Yan Zeng, **Rungtiwa Kosol**, Yu Cui, Naoya Kodama, Xiaoyu Guo, R.Prasert, V. Tharapong, Guangbo Liu, Jinhu Wu, Guohui Yang, Yoshiharu Yoneyama, Noritatsu Tsubaki. Heteroatom doped iron-based catalyst prepared by urea

self-combustion method for efficient CO_2 hydrogenation. ***Fuel***, 2020, 276, 118102. IF = 5.578

7. Fei Chen, Peipei Zhang, Liwei Xiao, Jiaming Liang, Baizhang Zhang, Heng Zhao. **Rungtiwa Kosol**, Qingxiang Ma, Jienan Chen, Xiaobo Peng, Guohui Yang, Noritatsu Tsubaki. Structure−Performance Correlations over Cu/ZnO Interface for Low Temperature Methanol Synthesis from Syngas Containing CO_2. ***ACS Applied materials & interfaces***, 2021, 13, 8191-8205. IF = 8.758
8. Xiaoyu Guo, Lisheng Guo, Yan Zeng, **Rungtiwa Kosol**, Xinhua Gao, Yoshiharu Yoneyama, Guohui Yang, Noritatsu Tsubaki. Catalytic oligomerization of isobutyl alcohol to jet fuels over dealuminated zeolite Beta. ***Catalysis Today***, 2021, 368, 196-203. IF = 5.825

List of conference

1. Iron catalysts supported on nitrogen functionalized carbon for improved CO_2 hydrogenation performance, 63rd Annual Meeting of JPI (69th R＆D Symposium of The Japan Petroleum Institute; JPI, 25th JPIJS Poster Sess.) Tokyo, Japan, 2021. Oral

Acknowledgements

Undertaking this PhD has been a new experience and truly knowledge for me and it would not have been possible to do without the support and guidance that I received from many people especially from all of staff and members in Professor Tsubaki's laboratory throughout my doctoral period.

I would like to express my deeply gratitude to my supervisor, Professor Noritatsu Tsubaki, for his encouragement and most valuable advice, especially for giving me an opportunity to study in Japan for doctor degree. What is more important is that his profound erudition and rigorous attitude to science influenced me deeply, inspiring me to move towards the scientific way of passing the future. Without his pushing me ahead, encouragement and guidance, I could not have completed this paper.

My sincere thanks also go to Associate Professor Yoshiharu Yoneyama for providing me with advice, assistance in the experiment and helpful since I had first time been in Toyama. I shall extend my thanks to Associate Professor Guohui Yang, for his invaluable advice, constant encouragement and precise modification, and I admire his knowledge and his personality. His keen and vigorous academic observation enlightens me not only in my doctor academic career but also in my future study. The most thanks go to Professor Tharapong Vitidsant and Associate Professor Prasert Reubroycharoen as giving me the opportunity to get the MEXT scholarship.

I would like to give my deeply thanks to senior apprentice of Tsubaki lab for offering me a lot of help in my experiment and life. They are Dr. Peipei Zhang, Dr. Lisheng Guo, Dr. Jie Li, Dr. Yingluo He, Dr. Yuan Fang, Dr. Jaru Natakaranakul, Miss Yan Zeng, Mr. Heng Zhao, Mr. Yu Cui, Mr. Xiaoyu Guo, Mr. Fei Chen, Mr. Jie Yao, Mr. Kangzhou Wang. Besides, I also want to thank Mr. Shun Kazumi, Mr. Naoya Kodama, Mr. Yuya Araki, Mr. Hiroki Uesugi, Mr. Tatsuki Kojima, Mr. Hiroto Araki, Mr. Koki Ueda, Mr. Yusuke Imai, Mr. Toshihito Kakuma, Mr. Shoya Komiyama, Mr. Taiki Arakawa, Mr. Hayate Takahashi, Mr. Shoma Naito, Mr. Yusuke Seki and Miss Ayano Kimura.

Especially, Dr. Peipei Zhang, Dr. Yuan Fang, Miss Yan Zeng and Miss Ayano Kimura that always supporting me in every part of my life at here and many other students in University of Toyama for their assistance in study and life.

Last but not least, I would like to express my thanks to my beloved family and my friends for their continued encouragement and spiritual support during my study.